# A DEUTERIUM NMR AND QUANTUM CHEMICAL INVESTIGATION OF HYDROGEN BONDING IN ORGANIC SOLIDS

A Thesis

Presented to

The Faculty of Graduate Studies

of

The University of Guelph

by

RENEE WEBBER

In partial fulfilment of requirements

for the degree of

Master of Science

August, 2007

# Canada

# ABSTRACT

## A DEUTERIUM NMR AND QUANTUM CHEMICAL INVESTIGATION OF HYDROGEN BONDING IN ORGANIC SOLIDS

**Renee Webber**                                    **Advisor**
**University of Guelph**                             **Dr. Glenn H. Penner**

This thesis reports an investigation of hydrogen bonding in organic solids using solid-state $^2$H nuclear magnetic resonance and quantum chemical calculations. NMR measurements of deuterium chemical shifts ($\delta$), nuclear quadrupolar coupling constants ($\chi$) and asymmetry parameters ($\eta_Q$) have been performed on a variety of samples. For the first time, a C–H$\cdots$O hydrogen bond has been investigated using solid state NMR spectroscopy. Existence of the C–H$\cdots$O hydrogen bond has been demonstrated by comparing the values of $\delta$, $\Delta\delta$, $\chi$, $\eta_Q$ for the uncomplexed triphenylsilyl acetylene with the values for the triphenylsilyl acetylene-triphenylphosphine oxide. Samples containing two distinct hydrogen bonding situations have also been investigated; in most cases spectral resolution of the two separate spinning sideband manifolds has been achieved. Using the values of $\delta$, $\chi$ and $\eta_Q$ the relative strengths of the two hydrogen bonds have been inferred. Calculations have been performed and the values compare favourably with experimental results.

# Acknowledgements

I would first and foremost like to thank my supervisor *Dr. Glenn H. Penner* for his valuable advice and guidance not only during the past two years but throughout my undergraduate degree at the University of Guelph. My advisory committee members: *Dr. John Goddard* and *Dr. Nick P. C. Westwood*, are also gratefully acknowledged. I would also like to thank *Dr. Mario Monteiro* for being a member of my defence committee.

I am especially thankful to *Valerie Robertson* for her kindness and her technical support in operation of the spectrometer, also *Jun Gu* and *Peter Scheffer* for their assistance in the NMR Center. A special thanks to *Dr. Uwe Oehler* for his computer advice, as well as *Peng Liu* for his help with the computational aspect of this work.

I would also like to thank *Andrea McCullough* for helping me get started in the lab, *Neil Cockburn* for assistance throughout the previous year, *Bruce Liu* for his encouragement and *Liang Li* for his ability to make me laugh.

I would like to take this opportunity to thank *my family*, especially my *parents* who have always been very supportive and extremely encouraging to me throughout the years.

And finally, the financial support of this project by an operating grant to Dr. G.H. Penner from the *National Sciences and Engineering Research Council of Canada* (NSERC) is also acknowledged.

i

# Table of Contents

# List Of Tables

# List of Figures

**Chapter III  Results and Discussion**

# Table of Abbreviations

| | |
|---|---|
| $B_o$ | applied magnetic field |
| $\delta$ | chemical shift |
| $\Delta\delta$ | chemical shift anisotropy |
| -d | deuterated |
| $^2H$ | deuterium |
| $\hat{V}$ | electric field gradient tensor at the nucleus |
| eq | electric field gradient tensor at the nucleus |
| $\mathcal{H}$ | Hamiltonian |
| $V_{33}$ | largest component of the electric field gradient |
| $\nu_o$ | Larmor frequency |
| $\gamma$ | magnetogyric ratio |
| $\mu$ | magnetic moment |
| e$\mathbf{Q}$ | nuclear quadrupole moment |
| I | nuclear spin |
| $^1H$ | proton |
| $\chi$ | quadrupolar coupling constant |
| $\eta_Q$ | quadrupolar asymmetry parameter |

---

| | |
|---|---|
| aug | augmented to include diffuse functions |
| cc | correlation consistent |
| CSA | chemical shift anisotropy |

| | |
|---|---|
| DFT | density functional theory |
| efg | electric field gradient |
| HF | Hartree-Fock theory |
| IR | infrared |
| LCAO | linear combination of atomic orbitals |
| MAS | magic-angle spinning |
| MP | Møller-Plesset perturbation theory |
| NMR | nuclear magnetic resonance |
| PAS | principle axis system |
| QCC | quadrupolar coupling constant |
| TMS | tetramethylsilane |
| TPPO | triphenylphosphine oxide |
| TPSiA | Triphenylsilylacetylene |
| HPDEC | high-power decoupling |

# CHAPTER I

## *INTRODUCTION*

# 1. Hydrogen Bonding

The hydrogen bond is of vital importance in structural chemistry and biology. Its fundamental importance lies in its role in molecular association. In supramolecular chemistry, hydrogen bonds are able to control and direct the structures of molecular assemblies because they are sufficiently strong and sufficiently directional. In biology, the hydrogen bond is important as it lies in an energy range between van der Waals interactions and covalent bonds. This energy range is such that hydrogen bonds can associate and dissociate quickly at ambient temperature; an essential condition for biological reactions that occur at ambient temperature. For these reasons, the subject of hydrogen bonding is of major interest and remains relevant with each new focus in chemical and biological research [1].

## 1.1. Definition

Hydrogen bonding was brought into the chemical mainstream via Pauling's chapter on hydrogen bonding in *The Nature of the Chemical Bond* [2-6]. Pauling expressed two core ideas within the chapter. First he stated: "Under certain conditions an atom of hydrogen is attracted by rather strong forces to two atoms instead of only one, so that it may be considered to be acting as a bond between them. This is called a hydrogen bond" [6]. The second idea to emerge from Pauling's work is that the hydrogen bond is an electrostatic interaction. He stated thus, "It is now recognized that the hydrogen atom, with only one stable orbital (the 1s orbital), can form only one covalent bond, that the hydrogen bond is largely ionic in character, and that it is formed only between the most electronegative atoms" [6]. The electrostatic nature of the hydrogen bond, as well as the

2

unique ability of the H atom to form such associations, arises from; (1) the time-averaged position of the H electron (between H and X) and (2) the deshielding of the H atom as X becomes more electronegative. Pauling assumed that the latter would only occur if X and A were extremely electronegative. If this were true, then the hydrogen bond phenomenon would be limited to interactions of the type X–H···A where X and A could be any of the following elements: F, O, Cl, N, Br, and I.

Pauling's ideas were developed and refined resulting in the definition of a hydrogen bond by Pimentel and McClellan. This is the first of the modern definitions of the phenomenon, "A hydrogen bond is said to exist when (1) there is evidence of a bond, and (2) there is evidence that this bond sterically involves a hydrogen atom already bonded to another atom" [7]. This new definition makes no assumptions about the nature of X and A and thus, permits an evaluation of the hydrogen bonding potential of groups such as: C–H, P–H, S–H and π-acceptors. Since the single electron of the H atom is involved in the X–H covalent bond, the H atom is always deshielded in the forward direction, regardless of the nature of the X atom. This idea led Jeffrey and Saenger to pose the question, "Should the C–H···O=C interaction be referred to as a hydrogen bond, even though there is every reason to suspect that the carbon atom is not electronegative and may even carry a positive charge? By Pauling's definition, the answer is no. By Pimentel and McClellan's definition, the answer is yes" [8].

Steiner and Saenger eventually refined Pimentel and McClellan's definition to include a quantitative aspect. They considered a hydrogen bond to be "any cohesive interaction X–H···A where H carries a positive and A a negative (partial or full) charge and the charge on X is more negative than on H" [9].

3

## 1.2. Classification of Hydrogen Bonds

As evidenced by the previous section (1.1), understanding the nature of hydrogen bonds appears to be more elusive than for covalent and ionic bonds, and van der Waals forces. This is because the term hydrogen bond applies to a very wide range of interactions. Within this range are very strong hydrogen bonds which resemble covalent bonds, as well as weak hydrogen bonds which are similar to van der Waals forces. The majority of hydrogen bonds are distributed between the two extremes. Table 1.1 outlines the three categories of hydrogen bonds as well as their general characteristics.

**Table 1.1**
**Classification of hydrogen bonds**

|  | Very Strong | Strong | Weak |
|---|---|---|---|
| X–H···A interaction | Mainly covalent | Mainly electrostatic | Electrostatic |
| Bond lengths | X–H≈H···X | X–H< H···A | X–H<< H···A |
| H···A (Å) | ~1.2-1.5 | ~1.5-2.2 | 2.2-3.2 |
| X···A (Å) | 2.2-2.5 | 2.5-3.2 | 3.2-4.0 |
| Bonds shorter than vdW | 100% | Almost 100% | 30-80% |
| Bond angles (°) | 175-180 | 130-180 | 90-180 |
| Bond energy (kJ/mol) | 60-170 | 15-60 | <15 |
| Relative IR $v_s$ vibration shift (cm$^{-1}$) | >25% | 5-25% | <5% |
| Effect on crystal packing | Strong | Distinctive | Variable |
| Utility in crystal engineering | Unknown | Useful | Partly useful |
| Covalency | Pronounced | Weak | Vanishing |
| Electrostatics | Significant | Dominant | Moderate |
| Examples | [F···H···F]⁻ | O–H···O=C | C–H···O |
|  | [N···H···N]⁺ | N–H···O=C | O–H···π |
|  | P–OH···O=P | O–H···O–H | Os–H···O |

These categories of hydrogen bonds are meant to be used as a guide only and are not intended to divide hydrogen bonds into distinct compartments. Such a distinction would be very misleading as the energies and the properties of hydrogen bonds lie in continuous ranges.

Very strong hydrogen bonds are formed by unusually activated donors and acceptors often in an intramolecular context. They are commonly formed between an acid and its conjugate base, $X-H\cdots X^-$, or between a base and its conjugate acid, $X^+-H\cdots X$. This is to be expected since a deficiency of electrons of the donor group further deshields the proton and thus increases the positive charge, while an excess of electrons on the acceptor increases its negative charge and the interaction with the deshielded proton. Very strong hydrogen bonds are of great importance in the context of chemical reactivity and have therefore been studied for many years [10,11]. The defining characteristic of these types of hydrogen bonds is their substantial covalent nature [12]. For example, in very strong hydrogen bonds the $X-H$ and $H\cdots X$ distances are comparable. These bonds may therefore be studied via methods used to study proper covalent bonds.

Strong hydrogen bonds are not quasi-covalent but rather electrostatic in nature. All hydrogen bonds are electrostatic but this particular characteristic dominates this large and most common category of hydrogen bonds. Molecules that are capable of forming strong hydrogen bonds always do so unless there are unfavorable steric effects. For this reason, strong hydrogen bonds are often regarded as *normal* hydrogen bonds with the other two categories being the exceptions.

Weak hydrogen bonds, though numerous, were not investigated in a general sense until recently. In part this is because molecules which contain groups capable of forming weak hydrogen bonds do not necessarily need to associate in such a manner. Weak hydrogen bonds are electrostatic but this depends substantially on the nature of the donor and acceptor. The pairing of a strong donor/acceptor with a weak counterpart, for example $O-H\cdots Ph$ and $C\equiv C-H\cdots O$, results in hydrogen bonds which are quite

electrostatic and comparable to bonds like O–H⋯O–H. The pairing of a weak donor/acceptor with a weak counterpart results in bonds that are barely stronger than van der Waals interactions, and are only distinguishable via evidence of directional involvement of the A–H bond.

## 1.3. C–H⋯O Interactions

The idea that C–H groups may be involved in attractive electrostatic interactions of appreciable strength is generally attributed to Glasstone [13]. In 1937, he investigated several liquid complexes such as 1:1 chloroform-acetone which appeared to have abnormal physical properties. He found that the molar polarizations of the mixtures were larger than those of the pure components, and attributed this to a directional electrostatic interaction of the type shown:
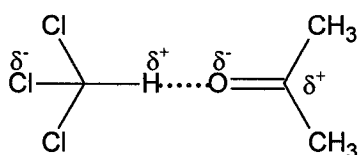


The idea was quickly accepted by spectroscopists and by 1939, Gordy [14] had classified the interaction as a C–H⋯O 'hydrogen bond' with properties similar to O–H⋯O and N–H⋯O hydrogen bonds.

The first systematic study of C–H⋯O hydrogen bonds in crystals was undertaken by Sutor in the early 1960s [15,16]. Sutor, assuming a van der Waals distance of 2.6 Å for the H⋯O contact, showed that hydrogen bonds exist in crystalline theophylline (d=2.25 Å), caffeine (d=2.12 Å), uracil (d=2.20 Å, 2.27 Å) and a few other compounds

that contain $C(sp^2)$–H groups. Despite the seemingly conclusive crystallographic evidence she presented, her ideas were drowned in skepticism, if not outright hostility.

It was not until two decades later, with the landmark paper by Taylor and Kennard [17], that the subject was properly resurrected. The study employed the Cambridge Crystallographic Database (CSD) and focused on 113 high quality neutron diffraction structures. The study proved that C–H···O hydrogen bonds are electrostatic and that they occur within certain distance (C···O, 3.0-4.0Å) and angle (C–H···O, 90-180°) ranges.

Today, there is a general consensus that C–H···O hydrogen bonds have significant implications in many diverse areas of structural chemistry [18-21] and biology [8]. These interactions are no longer considered obscure phenomena with little practical importance or a mere basis for crystallographic disputes.

### 1.3.1. Bond Lengths

The shortest C–H···O contacts observed in crystal structures have donor-acceptor separations of ~3.0 Å for C···O and ~2.0 Å for H···O. Such short contacts can only occur with the most acidic donors, such as those shown in Figure 1.1. However, even for acidic C–H donors, H···O contacts of ~2.0 Å are the minority; H···O distances are generally in the 2.1 Å to 2.3 Å range.

If H···O separations in crystals are statistically characterized, different behaviour is observed for chemically different C–H donors. For the strongest donors, such as acetylene and $CHCl_3$, the frequency distributions of H···O interactions have a defined maximum and fall off for longer distances (Figure 1.2). This same phenomenon is seen

7

with more 'conventional' hydrogen bonds like O–H···O [8]. For weaker donors, the maximum of the frequency distribution is shifted to longer distances and becomes slightly less defined. For the weakest C–H donors (*i.e.* $CH_3$) there is no maximum and the number of contacts, n, simply increases with increasing distance as shown in Figure 1.2.

(a)  P—C≡C—H    Si—C≡C—H    N≡C—H

(b)

(c)  Cl—C(Cl)(Cl)—H    Cl—C(Cl)(H)—H    $O_2N$—C($O_2N$)($O_2N$)—H

---
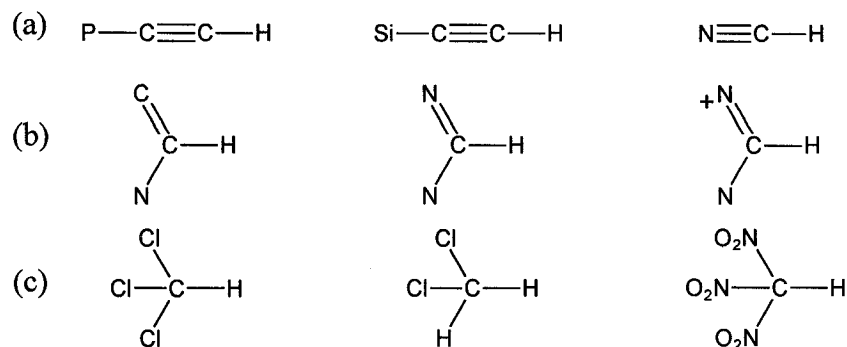
**Figure 1.1.**  C-H groups that can form short C–H···O hydrogen bonds. Examples are given for (a) $C(sp^1)$–H, (b) $C(sp^2)$–H, and (c) ) $C(sp^3)$–H.

---
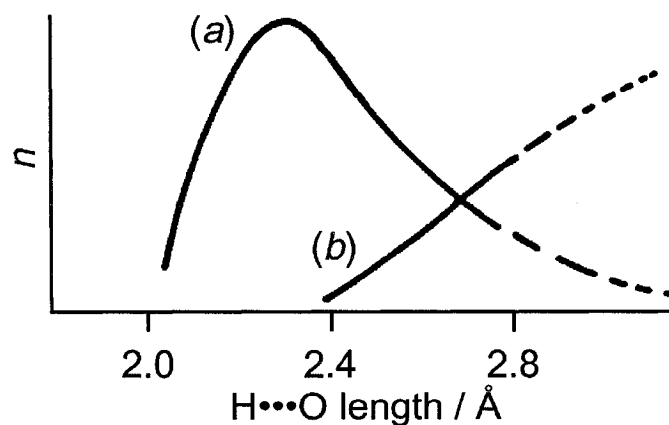


**Figure 1.2**  Frequency distribution for (a) strong C–H···O donors and (b) weak C–H···O donors [22].

The distribution for the weak C–H⋯O donors is difficult to interpret as one might expect to see a maximum similar to that for the strong case, only weaker. One of the defining factors is that, in competition with other intermolecular forces, hydrogen bonds from the less acidic C–H donors will more frequently be the losers and be pushed out of optimal geometry.

Crystallographers often attempt to correlate hydrogen bond distances with hydrogen bond strengths. This can be misleading as shorter contacts do not necessarily denote stronger hydrogen bonds; nor can a contact be disqualified as a hydrogen bond simply because it is beyond a certain distance limit. Attempts to obtain reliable bond length-bond energy correlations remain unsuccessful; the same holds true for conventional hydrogen bonds. However, it is possible to relate the mean H⋯O distances of large data samples to the nature of the donor and acceptor.

C–H donors that are bonded to electron-withdrawing groups are said to be 'strong' or 'activated'; these donors tend to form shorter contacts than their weaker counterparts. Desiraju was able to quantify this phenomenon using a series of crystal correlation studies [23-25]. Using a group of chloroalkyl compounds, he showed that the mean donor-acceptor separation of hydrogen bonds follows the sequence $Cl_3CH$ > $Cl_2CCH$ > $ClC_2CH$ < $C_3CH$, with mean C⋯O separations of 3.32, 3.40, 3.46, and 3.59 Å respectively [23]. Desiraju further established this effect using results that showed that the more acidic alkynes formed shorter contacts to oxygen than the less acidic alkenes [24]. In an important generalization, a direct correlation between average C⋯O separations and carbon acidity was shown (Figure 1.3) [25]. This correlation is sharp only

9

for sterically unhindered donors; sterically hindered C–H groups have much longer values than expected from Figure 1.3.

The effect of acceptor basicity on the C–H···O bond length is far less noticeable than that of C–H group acidity. However, Steiner showed that the effect of acceptor basicity is revealed when acidity effects are held constant [26]. He investigated six separate donors with a large variety of acceptors (up to 50 for some donors), and found that the average C···O (and H···O) distances were shorter for strong acceptors like carbonyl groups, and longer for weak acceptors such as ether O atoms. Figure 1.4 provides an example for a dichloromethane donor, illustrating the shift to higher values from C=O to C–O–C acceptors.
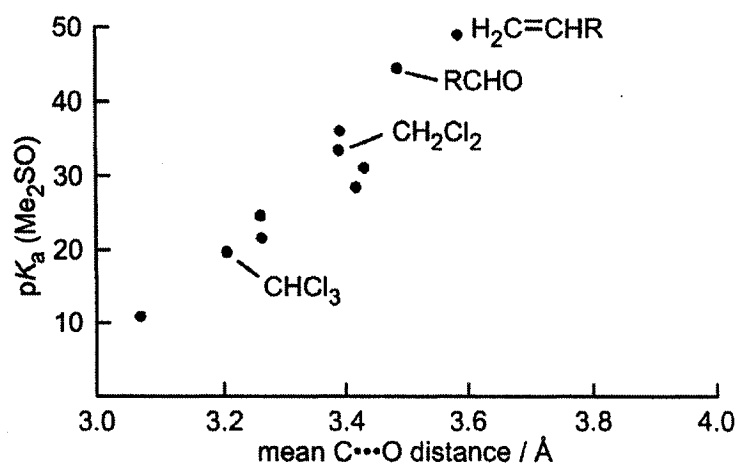


Figure 1.3    Correlation of mean C···O distance with C–H acidity. Only data for sterically unhindered donors is shown. Each data point represents the mean value of the broad distribution (such as those in Figure 1.2.) [22].

C=O
6
5
4
3
2
1
0

3.1 3.2 3.3 3.4 3.5 3.6 3.7 3.8
d (Å)

C=O
6
5
4
3
2
1
0

2 2.1 2.2 2.3 2.4 2.5 2.6 2.7
d (Å)

C-O-C
6
5
4
3
2
1
0

3.1 3.2 3.3 3.4 3.5 3.6 3.7 3.8
d (Å)

C-O-C
6
5
4
3
2
1
0

2 2.1 2.2 2.3 2.4 2.5 2.6 2.7
d (Å)
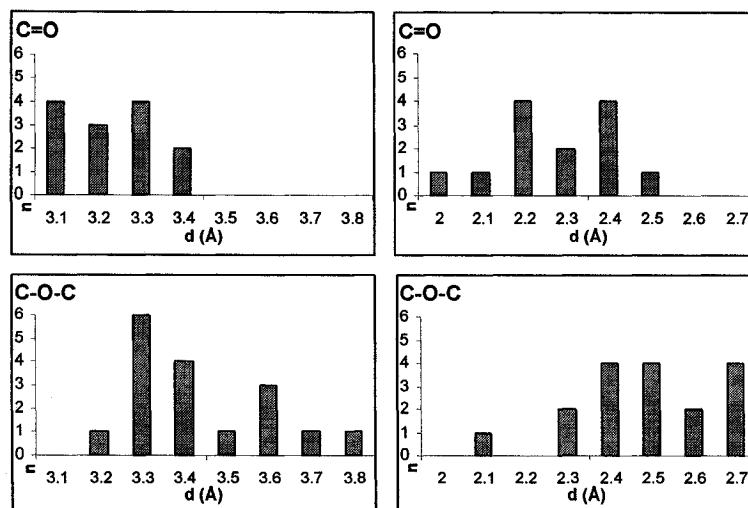
**Figure 1.4** Histogram of C⋯O (left) and H⋯O (right) separations in C–H⋯O hydrogen bonds donated by $CH_2Cl_2$ and accepted by C=O and C–O–C. Data for normalized H positions (C–H bond length of 1.08 Å) and H...O < 2.8 Å. Adapted from [26].

## 1.3.2. Directionality

Hydrogen bonds, in general, are directional interactions with a preference for linear geometry. For C–H⋯O hydrogen bonds this idea was revealed by Taylor and Kennard; upon analyzing the geometry of short C–H⋯O contacts they found that slightly bent arrangements with angles in the interval $\psi$=150-160° were most common, whereas heavily bent contacts did not occur [17]. The frequency distribution of C–H⋯O angles $\psi$ obtained by Taylor and Kennard is shown in Figure 1.5. In order to interpret this distribution properly, hydrogen bond angles must be corrected for the solid angle factor (sin $\psi$) as there is a greater probability for the occurrence of a hydrogen bond at lower values of sin $\psi$ for purely geometrical reasons [27]. Application of this cone correction factor results in more relevant histograms (see Figure 1.5).

11
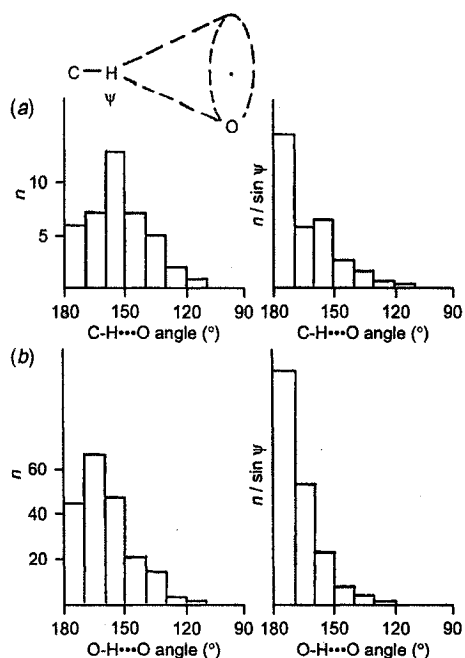
**Figure 1.5**   Frequency distribution of X–H···O angles (ψ) in crystal structures: (a) 41 intermolecular C–H···O contacts in organic neutron crystal structures; (b) 196 O–H···O hydrogen bonds in carbohydrate X-ray crystal structures. The cone correction relates the left and right histograms [22].

Figure 1.5 shows that C–H···O hydrogen bonds are in principle directional. Due to the weakness of the interaction, however, the C–H···O hydrogen bond can be easily bent, so that the directionality is blurred if steric hinderance or competition with other hydrogen bonding groups exists. This is generally the case for C–H···O interactions in carbohydrates, where O–H···O hydrogen bonds are the dominant intermolecular interaction forming a frame in which the weaker interactions are forced to adjust [28]. For very weak C–H donors (*i.e.* methyl groups) directionality is more easily distorted than for activated donors. In these cases, contributions from dispersion forces are similar or even larger than the electrostatic contribution [29], resulting in the C–H···O interactions becoming almost isotropic in nature.

Directionality is also determined by the chemical nature of the acceptor. For example, in the case of ketonic acceptors X–H vectors tend to point at the oxygen 'lone-pair lobes' which are in the carbonyl plane, in theory forming angles of $120°$ with the C=O bond [30]. This idea was demonstrated via a crystal correlation study of acidic and sterically unhindered C–H donors ($CHCl_3$, $CH_2Cl_2$, C≡C–H) [31]. If the approach of C–H to O=C is characterized by an angle $\alpha$ (H···O=C) and a torsion angle $\omega$ (H···O=C–Y), the polar scatterplot in Figure 1.6 is obtained. The histogram shows the distribution of $\omega$ and indicates a preference for in-plane contacts ($\omega$=0). It is clear from Figure 1.6 that acceptors in C–H···O interactions demonstrate significant directional behaviour, however, this directionality is soft.
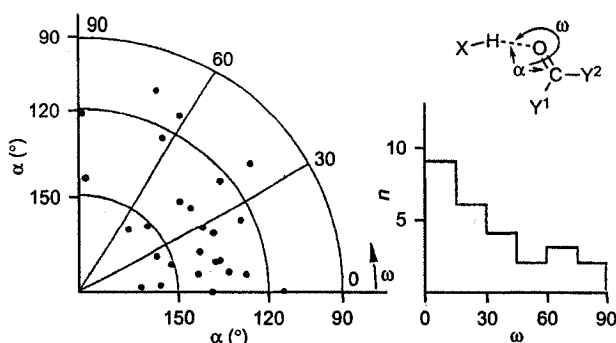


**Figure 1.6**    **Approach of acidic and sterically unhindered C–H donors to C=O acceptors. Geometrical parameters are defined in the inset [32].**

### 1.3.3. Covalent Bond Lengthening

It is an inherent property of hydrogen bonds that the covalent bonds of the groups involved therein are modified. Thus, in an interaction of the type $R_1$–X–H ···A–$R_2$, the X–H and A–$R_2$ covalent bonds are weakened, resulting in their lengthening. In a related

13

way, a less significant shortening of the $R_1$–X bond occurs. Corresponding spectroscopic shifts in the IR, arising from a reduction of the force constants of X–H and A–$R_2$ bonds, are easily observed. These effects are very pronounced for O–H$\cdots$O hydrogen bonds; analogous effects should be expected for C–H$\cdots$O interactions. The magnitude of the C–H lengthening can be estimated using the valence bond model of the hydrogen bond, which is based on a relationship between bond distances and valences. The results of this estimation are provided in Table 1.2.

**Table 1.2**
**Bond orders of H$\cdots$O and lengthening of**
**C–H in C–H$\cdots$O hydrogen bonds [33]**

| H$\cdots$O (Å) | Bond Order (valence units) | Bond lengthening (Å) |
|---|---|---|
| 1.9 | 0.076 | 0.029 |
| 2.0 | 0.058 | 0.022 |
| 2.1 | 0.044 | 0.017 |
| 2.2 | 0.034 | 0.013 |
| 2.3 | 0.026 | 0.010 |
| 2.4 | 0.020 | 0.007 |
| 2.5 | 0.015 | 0.005 |
| 2.6 | 0.011 | 0.004 |
| 2.8 | 0.007 | 0.002 |
| 3.0 | 0.004 | 0.001 |

For activated donors large bathochromic shifts, sometimes more than 100 cm$^{-1}$, have been observed. However, in the normal distance range of C–H$\cdots$O interactions, the C–H lengthening is very small ($\leq$ 0.001 Å) and thus difficult to detect even with neutron diffraction. As a result, covalent bond lengthening effects have not been studied extensively. In the only crystal correlation study to date, slight lengthening of the C–H bond was shown using neutron diffraction data for amino acid $C_\alpha$–H bonds. The reported lengthening was ~0.01 Å for contacts with H$\cdots$O ~ 2.30 Å and was shown to be

statistically significant at the 99 percent reliability level. The experimental data are in good agreement with the estimates determined from the valence bond model which associates an H⋯O separation of with a bond order of 0.026 valence units and a C–H lengthening of 0.01 Å.

## 2. Methods of Investigating Hydrogen Bonding

The methods used to study hydrogen bonds can be categorized as follows: (1) spectroscopy; (2) diffraction; (3) thermochemical; and (4) theoretical. The spectroscopic methods include infrared and Raman, microwave, NMR, and neutron inelastic scattering. Diffraction includes X-ray and neutron studies. Themochemical includes calorimetry of heats of mixing or dilution and the determination of enthalpies. Theoretical includes ab initio, semi-empirical, and empirical methods.

All of the methods mentioned play a crucial role in the investigation of hydrogen bonded systems. However, in this work only spectroscopic methods (vibrational and NMR), diffraction methods and computational methods will be discussed in detail.

## 2.1. Vibrational Spectroscopy

Vibrational spectroscopy is the classical method for the study of hydrogen bonding in condensed phases. Almost all kinds of hydrogen bonds were first discovered with this technique. Its applicability ranges from the strongest to the weakest hydrogen bonds, in both solution and the solid state.

### 2.1.1. IR Spectroscopy

Infrared (IR) spectroscopy is a very important tool used to investigate hydrogen bonding. IR spectroscopy obtains information about hydrogen bonding via spectra arising from transitions between the vibrational energy levels of the bonds. The frequency of the donor vibration X–H is most often studied, since it is quite easy to identify and in most instances is very sensitive to hydrogen bonding. The presence of a hydrogen bond

16

lengthens and weakens the covalent bond of the donor X–H, in turn, lowering the observed stretching vibrational frequency. Using this concept as a starting point, several relationships between X–H stretching frequencies and hydrogen bonds have been developed.

Numerous experimental studies [34-39] have also identified relationships between $v_{X-H}$ and X$\cdots$A bond distances. Based on these studies linear relationships were suggested [40,41], but as more crystal structure data became available, it was apparent that (for O–H$\cdots$O hydrogen bonds) linear relationships held for strong bonds, but for weaker bonds the relationship curved, the agreement deteriorated, and the frequency shifts became increasingly insensitive to changes in O$\cdots$O distances (see Figure 2.1).

A relationship between X–H IR stretching frequencies and hydrogen bond energies was proposed by Badger and Bauer [42] and Badger [43]. Using a variety of donors and acceptors, Bellamy and Pace [44] identified a linear relationship between hydrogen bond strength and the relative change in X–H stretching frequency. Purcell and Drago [45] and Drago, Vogel and Needham [46] also indicated the presence of linear relationships between strength and X–H stretching frequency, but found they were different for different acid-base combinations.

More recently, polarized Fourier transform IR spectroscopy using interferometry has been applied to slices of single crystals cut parallel to specific crystal faces. This method allows for the correlation of specific frequencies to specific bonds. The method has been applied to several carbohydrates [47-49] for which neutron structures are available. Even with precise crystal structures, the deviations from a linear relationship between $v_{O-H}$ and O–H, O$\cdots$O, O$\cdots$H distances greatly exceed experimental uncertainties.
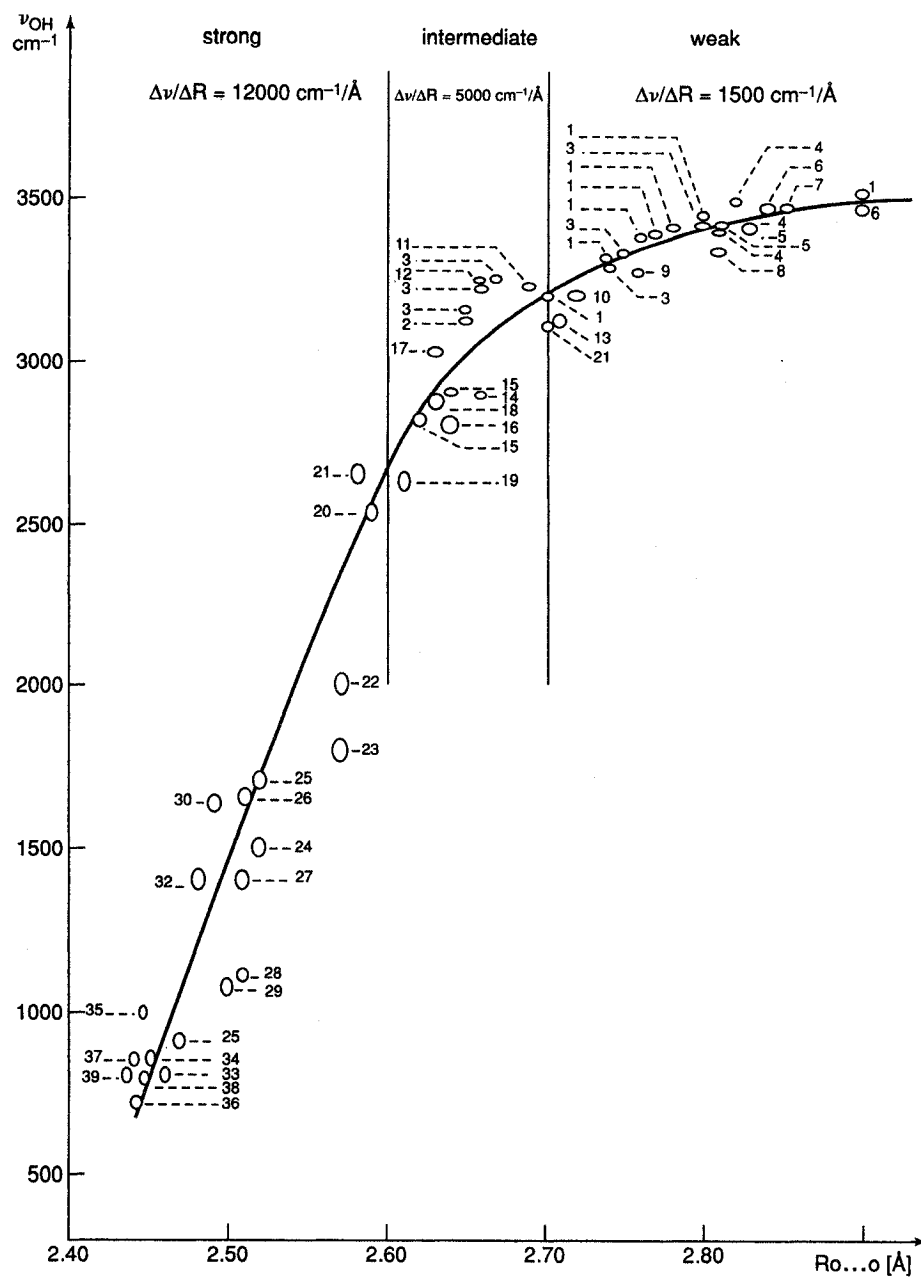
**Figure 2.1** Correlations between O–H $\nu_s$ and O⋯O hydrogen bond distances. Points 1-6 are salt hydrates, 7 is oxalic acid dihydrate, 33-38 are strong bonds in organic hydrogen anions. [38]

Despite many successful applications, the spectroscopic method is not free from drawbacks. The effects of weak hydrogen bonds on vibrational spectra are not always clear, and can be quite dissimilar for different types of weak hydrogen bonds. Lutz et al. [50] found that in instances of weak hydrogen bonding, the band width and intensity of the stretching mode increase and can often act as a more reliable indicator of hydrogen bond formation than the 'typically' investigated red shift.

### 2.1.2. Raman Spectroscopy

Despite the large amount of work conducted using IR methods, Raman spectroscopy is rarely mentioned in studies of hydrogen bonding. Raman spectra are only readily accessible for liquids; gases result in spectra that are very weak, and with solids Rayleigh scattering is too strong. Thus the useful correlation with microwave spectroscopy, ab initio calculations, and crystal structure analyses is not possible. However, since the selection rules of IR and Raman differ, Raman is occasionally employed to supplement IR spectral assignments.

## 2.2. NMR Spectroscopy

In most hydrogen bonds, several nuclei may be observed by NMR spectroscopy. In particular, protons become increasingly deshielded with increasing hydrogen bond strength which causes shifts to higher frequency [11]. This deshielding effect was investigated using ab initio calculations on hydrogen bonded $O-H\cdots O$ systems [51, 52]. The deshielding of the isotropic chemical shift was explained by three effects. First, the proton loses electron density upon hydrogen bond formation, and due to the fact that

19

there are only s functions on the hydrogen, the chemical shift tensor components are deshielded isotropically. Second, the acceptor oxygen (for the case O–H···O hydrogen bonds) deshields the perpendicular components but shields the parallel component. Third, the oxygen atom of the hydrogen bond donor accounts for some deshielding in the perpendicular components and can either shield or deshield the parallel component. The net result is a deshielding of both the isotropic chemical shift and the perpendicular components of the chemical shift tensor. The sensitivity of $^1$H NMR to changes in electronic environment make it a useful tool for detecting hydrogen bonding from weak donors, such as S–H and C–H and weak acceptors, such as multiple bonds and aromatic rings, as described by Foster and Fyfe [53].

Hydrogen bonding is complex in the liquid state because of the uncertainty in identifying particular bonds and the number of molecules involved. As a result, solution NMR spectroscopy, unlike IR spectroscopy, has never become a major investigative tool in this field. Improved multi-dimensional solution NMR experiments have made NMR spectroscopy as powerful a tool for elucidating molecular structure in solution as X-ray crystallography in crystals. However, such advancements have not impacted the study of hydrogen bonds. The more recent development of solid-state NMR spectroscopy has prompted a greater interest in the application to hydrogen bonding. This is certainly because the results of solid state NMR analyses can be correlated with crystal structures. For a discussion of solid state NMR and its application to hydrogen bonding, see Section 6.

## 2.3. Neutron and X-ray Diffraction

Single crystal structure analyses play an important role in the study of hydrogen

bonds, as they provide direct information about the stereochemistry. This is essential as

the location of the hydrogen atoms is necessary in understanding the nature of the

hydrogen bond.

X-ray diffraction methods are used to determine electron-density distributions,

and locate electron-density maxima of the atoms. Neutron diffraction methods on the

other hand locate actual nuclei. In neutron diffraction, unlike X-ray diffraction, the

coherent scattering of the atoms is not a function of atomic number, but instead varies

over a relatively narrow range as seen in Figure 2.2.
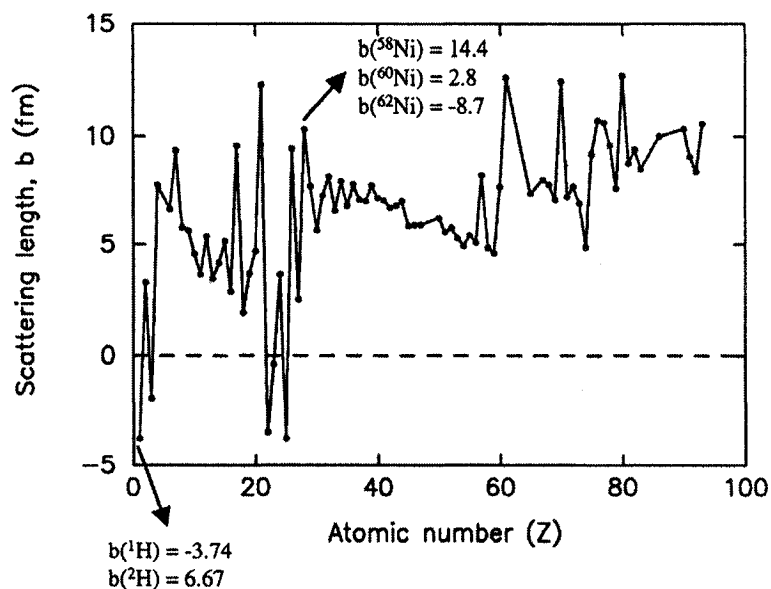


Figure 2.2   Neutron scattering lengths vary fairly randomly as a function of atomic
number. In addition, isotopes of the same element can have very different
scattering lengths, as shown here for nickel and hydrogen. [54]

Hydrogen has a scattering power for neutrons that is about half that of carbon and oxygen; compared with 1/50 for X-rays. With X-rays there is a fall-off with scattering angle due to thermal motion and the size of the electron cloud as seen in Figure 2.3. Since neutrons scatter mainly from nuclei rather than the atomic shell, the scattering power does not fall-off with the scattering angle, thus the only fall off is that due to thermal motion. The only major difficulty with hydrogen in neutron studies is the large incoherent neutron scattering factor which results in high background noise. Substitution with deuterium, which has a small incoherent scattering factor, is often used to circumvent this problem.
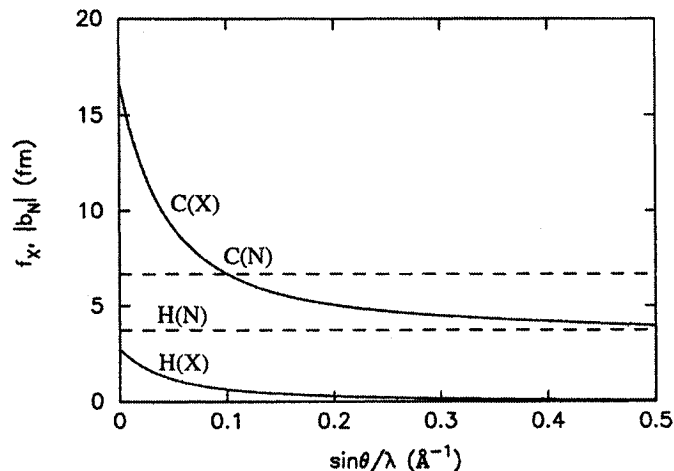


**Figure 2.3** **The fall off of X-ray scattering factors (solid lines) with scattering angle is not seen in the neutron case (dashed lines). The examples shown are carbon and hydrogen. [54]**

With the tremendous advances in diffractometry, computation, and low temperature techniques, highly precise structural information is now available from X-ray diffraction [55], though the location and refinement of hydrogen atom positions still remains at the limits of the technique [56]. Further concern arises from the fact that in X-ray structures, X–H distances are usually ~0.2 Å shorter than the internuclear distances

obtained from neutron diffraction analyses (as an example see Table 2.1). This occurs because X-rays are scattered by electrons and thus the atomic position derived for a hydrogen atom lies at the centre of the electron density. The latter is not centered on the H nucleus, but is displaced towards the atom X. Neutron diffraction avoids this problem as the scattering centers around the atomic nucleus itself. The distances derived from neutron studies correspond nearly to the interatomic distances and thus, neutron diffraction is unparalleled in the determination of accurate hydrogen bond parameters. It has been argued that while neutron distances are more accurate, they are not necessarily the most chemically meaningful since one cannot identify an atom with just a nucleus, but rather consider both its nucleus and its electrons [57, 58]. In any event distances from neutron diffraction have established themselves as benchmarks in hydrogen bond research [10, 59].

**Table 2.1**
**X–H bond lengths in an X-ray and a neutron crystal structure of α-glycine, and distances between H atom positions in these structures (Δ) [60]**

| Bond | X–H$_X$ (Å) | X-H$_N$ (Å) | Δ (Å) |
|---|---|---|---|
| N–H(1) | 0.996(19) | 1.054(2) | 0.066 |
| N–H(2) | 0.982(18) | 1.037(2) | 0.067 |
| N–H(3) | 0.959(16) | 1.025(2) | 0.070 |
| C(2)–H(4) | 0.963(16) | 1.090(2) | 0.130 |
| C(2)–H(5) | 0.966(18) | 1.089(2) | 0.133 |

### 2.3.1. Normalization of X–H Bonds

The difficulty in accurately determining hydrogen positions from X-ray analysis leads to the technique of distance normalization. In this procedure, the distances obtained in an X-ray analysis are corrected by extending the X–H bond vector to the average neutron derived distance of X–H. If no neutron-determined values are available, gas phase spectroscopy values are employed. Hydrogen bond distances are generally shorter in normalized geometries than in non-normalized geometries, and bond angles tend to be smaller.

In routine normalization, the neutron value of X–H is assumed to be constant; thus, modification by the hydrogen bond is ignored. For weak hydrogen bonds this modification is so small (< 0.01 Å) that normalization to a constant value is justified. For strong hydrogen bonds, X–H is often elongated by several hundredths of an Å, making normalization more approximate but still reasonable. For very strong hydrogen bonds, X–H can be elongated by more than 0.05 Å, making standard normalization procedures questionable. For very strong hydrogen bonds, the elongation of X–H has been parameterized and can be used in a refined normalization procedure [33].

## 2.4. Computation

Quantum chemistry complements crystallography and spectroscopy in the study of hydrogen bonding. Theoretical methods can provide benchmark values for the energies of intermolecular interactions without the complicating effects of the solid state or solution environment. Computational methods can be used to study domains on the potential energy structure which are far from the equilibrium structure; whereas

24

spectroscopy and diffraction methods are limited to providing information on equilibrium geometries. This aspect of computational chemistry allows for the investigation of the electronic redistributions that accompany the formation of hydrogen bonds, polymorphism, crystallization, and geometry interconversions.

An obvious limitation of computational chemistry is that is severely limited by the computing power available at the time. Advances in the number-crunching ability of computers has meant that computational results age much faster than experimental results. For example, about fifteen years ago computational work on intermolecular interactions was carried out using semi-empirical methods. At the time such methods were state-of-the-art, despite the fact that they were never designed or parameterized to treat intermolecular interactions properly. Today, much of this older work is completely disregarded with the exception of general trends which may have been accurately predicted. With the super computers now available, ab initio molecular orbital calculations are the methods of choice for hydrogen bonded complexes of simple molecules containing first and second row elements.

Ab initio molecular orbital calculations seek minimum energy intra- and inter-molecular geometry by solving the wave equation using a linear combination of atomic orbitals (LCAO). Coefficients are attached to each of the one-electron atomic orbitals and varied to obtain the minimum energy. Polarization effects are introduced by adding p-orbitals to the s-orbitals of hydrogen, d-orbitals to the s- and p-orbitals of first row elements, and so on. In order to carry out the calculations, atomic orbitals need to be expressed in an analytical form, most often by using Gaussian functions (this is known as a basis set). The more complicated the basis-set, the greater the computer power and time

required. However, with the development of super computers, this is not a serious problem. In general, the larger the basis set the closer the result comes to the Hartree-Fock limit. Though this is not to say that larger basis sets should always be employed; sometimes simpler basis-sets give better agreement with experimental results due to cancellation of errors.

A study outlining the effects of the basis-set size and correlation in calculating the hydrogen bond energies of the Watson-Crick base pairs is given by Gould and Kollman [61]. A general account of the use of ab initio methods for calculating molecular structures is given by Boggs [62]. An excellent analysis of the many ab initio studies on the water dimer is given by Scheiner [63].

Despite the widespread use of ab initio methods in the study of hydrogen bonding, these methods are not without fault. The results of ab initio calculations are *very* dependent on the choice of basis set, the use of density functional theory (DFT) and the various stratagems by which electron correlation effects are handled. All of these aspects must be considered carefully when assessing computational work.

# 3. NMR Interactions

For a diamagnetic compound, the interactions observed in NMR spectroscopy are described by the following Hamiltonians:

$$\mathcal{H}_{total} = \mathcal{H}_{external} + \mathcal{H}_{internal} \tag{3.1}$$

where

$$\mathcal{H}_{external} = \mathcal{H}_Z + \mathcal{H}_{RF} \tag{3.2}$$

and

$$\mathcal{H}_{internal} = \mathcal{H}_D + \mathcal{H}_{CS} + \mathcal{H}_J + \mathcal{H}_{SR} + \mathcal{H}_Q \tag{3.3}$$

A brief description of these nuclear spin Hamiltonians is given in Table 3.1. For a more detailed description of the various NMR interactions, the reader is referred to Harris [64].

**Table 3.1**
**Nuclear spin Hamiltonians [64]**

| Hamiltonian | Term | Interaction of nuclear spins with |
|---|---|---|
| $\mathcal{H}_Z$ | Zeeman | external static magnetic fields. |
| $\mathcal{H}_{RF}$ | Radiofrequency | external radiofrequency magnetic fields. |
| $\mathcal{H}_D$ | Dipolar | each other, directly via magnetic dipole moments. |
| $\mathcal{H}_{CS}$ | Chemical shift | induced magnetic fields originating from orbital motions of electrons. |
| $\mathcal{H}_J$ | Spin-coupling | each other, indirectly via electron spins. |
| $\mathcal{H}_{SR}$ | Spin-rotation | the magnetic moment associated with the molecular angular momentum. |
| $\mathcal{H}_Q$ | Quadrupolar | electric field gradients. |

## 3.1. The Zeeman Interaction

The Zeeman interaction is the basis of NMR spectroscopy and occurs for all nuclei with spin quantum number I > 0. For a nucleus with spin I the Zeeman interaction will create (2I + 1) energy levels, with a separation of $\gamma \hbar \mathbf{B_0}$, in the presence of a magnetic field $\mathbf{B_0}$. The Hamiltonian for the Zeeman interaction is given as:

$$\mathcal{H}_z = \mu \mathbf{B_o} = -\gamma \hbar \mathbf{B_o} \cdot \mathbf{I}_z \tag{3.4}$$

where $\gamma$ is the magnetogyric ratio, and $I_z$ is the nuclear spin angular momentum vector along the z-direction. In NMR spectroscopy, units of frequency are preferred over units of energy, thus the frequency at which a pure Zeeman interaction occurs is given by the Larmor frequency, $\nu_o$:

$$\nu_o = \gamma B_o / 2\pi \tag{3.5}$$

where $\nu_o$ is in Hertz.


## 3.2. The Radiofrequency Interaction

The radiofrequency interaction is similar to the Zeeman interaction as both involve the interaction between a nuclear spin and a field. As the name implies, the radiofrequency interaction involves the coupling of the nuclear spins to a time-dependent radiofrequency field. If the radiofrequency radiation $\mathbf{B_1}$ is chosen to be along the x-axis, then the Hamiltonian for the interaction is given as:

$$\mathcal{H}_{RF} = -\gamma \hbar \mathbf{B_1} \cdot \mathbf{I}x \tag{3.6}$$

28

## 3.3. The Dipolar Interaction

The dipolar interaction arises from the direct magnetic dipole-dipole coupling between two nuclei, A and X of nuclear spin I and S. If the two nuclei are the same, that is there is a single type of spin, then the interaction is homonuclear and its Hamiltonian can be written as:

$$\mathcal{H}_D(\text{homo}) = \frac{3\gamma^2\hbar^2}{2r^3_{AA}} I_A \cdot \hat{D}_{AA} \cdot I_A \tag{3.7}$$

where $r_{AA}$ is the internuclear distance and $\hat{D}_{AA}$ is the dipolar coupling tensor. The trace of the dipolar tensor is zero and therefore the observed dipolar interaction vanishes under motional averaging (*i.e.* in solution).

$$\text{trace } \hat{D} = \text{trace} \begin{bmatrix} D_{xx} & D_{xy} & D_{xz} \\ D_{yx} & D_{yy} & D_{yz} \\ D_{zx} & D_{zy} & D_{zz} \end{bmatrix}$$

$$= \text{trace} \begin{bmatrix} \dfrac{r^2 - 3x^2}{r^2} & \dfrac{-3xy}{r^2} & \dfrac{-3xz}{r^2} \\ \dfrac{-3yx}{r^2} & \dfrac{r^2 - 3y^2}{r^2} & \dfrac{-3yz}{r^2} \\ \dfrac{-3zx}{r^2} & \dfrac{-3zy}{r^2} & \dfrac{r^2 - 3z^2}{r^2} \end{bmatrix} \tag{3.8}$$

And after diagonalization:

$$\text{trace } \hat{D}_{PAS} = \text{trace} \begin{bmatrix} D_{11} & 0 & 0 \\ 0 & D_{22} & 0 \\ 0 & 0 & D_{33} \end{bmatrix} = \text{trace} \begin{bmatrix} 1 & 0 & 0 \\ 0 & 1 & 0 \\ 0 & 0 & -2 \end{bmatrix}$$

$$= D_{11} + D_{22} + D_{33} \tag{3.9}$$

where $\hat{D}_{PAS}$ is the dipolar coupling tensor in the principal axis system (PAS).

29

If however, A and X are different, the interaction will be the summation of all possible pair wise interactions, that is:

$$\mathcal{H}_D(\text{hetero}) = \frac{\gamma_A \gamma_X \hbar^2}{r^3_{AX}} \mathbf{I}_A \cdot \hat{\mathbf{D}}_{AX} \cdot \mathbf{I}_X \qquad (3.10)$$

As can be seen from Equations (1.7) and (1.10), the dipolar interaction is independent of the applied magnetic field, but decreases dramatically with internuclear distance. For this reason, dipolar coupling can be exploited in certain cases to yield information regarding the geometry of a given molecule.

## 3.4. The Chemical Shift Interaction

The electrons that surround a nucleus are not passive in the applied magnetic field, but react to produce a secondary magnetic field. The interaction of the secondary field with the nucleus is known as the shielding interaction; the resulting frequency shift in the NMR spectrum is known as the chemical shift. The Hamiltonian for the chemical shift interaction is given as:

$$\mathcal{H}_{CS} = \gamma \hbar \mathbf{I} \cdot \hat{\sigma} \cdot \mathbf{B}_o \qquad (3.11)$$

When a sample is placed in the external field $\mathbf{B}_o$ it becomes magnetized and the applied field is modified by an induced field. This induced field arises from a perturbation of the electron motion around the nuclei. The induced field $\mathbf{B}_{ind}$ is directly proportional to the applied field $\mathbf{B}_o$:

$$\mathbf{B}_{ind} = -\hat{\sigma}\mathbf{B}_o \qquad (3.12)$$

Therefore the resulting local field at the nucleus is:

$$\mathbf{B}_{local} = (1 - \hat{\sigma})\mathbf{B}_o \qquad (3.13)$$

where $\hat{\sigma}$ is the chemical shielding tensor which describes the orientational dependence of the interaction and can be represented by an ellipsoid centered on the nucleus.

It is useful at this point to decompose $\hat{\sigma}$ into a symmetric ( $\hat{\sigma}^s$ ) and an antisymmetric term ($\hat{\sigma}^a$):

$$\hat{\sigma} = \hat{\sigma}^s + \hat{\sigma}^a \tag{3.14}$$

where

$$\hat{\sigma}^s_{\alpha\beta} = \frac{\sigma_{\alpha\beta} + \sigma_{\beta\alpha}}{2}$$

$$\hat{\sigma}^a_{\alpha\beta} = \frac{\sigma_{\alpha\beta} - \sigma_{\beta\alpha}}{2}$$

$$\tag{3.15}$$

This decomposition is important since only the symmetric portion of the shielding tensor affects the NMR spectrum significantly. Thus, from this point $\hat{\sigma}$ should be taken to mean the symmetric part of the shielding tensor.

In the principal axis system $\hat{\sigma}$ is converted to its diagonal form with three principal elements:

$$\hat{\sigma} = \begin{bmatrix} \sigma_{xx} & \sigma_{xy} & \sigma_{xz} \\ \sigma_{yx} & \sigma_{yy} & \sigma_{yz} \\ \sigma_{zx} & \sigma_{zy} & \sigma_{zz} \end{bmatrix} \xrightarrow{\text{diagonalization}} \hat{\sigma}_{PAS} = \begin{bmatrix} \sigma_{11} & 0 & 0 \\ 0 & \sigma_{22} & 0 \\ 0 & 0 & \sigma_{33} \end{bmatrix} \tag{3.16}$$

The principal elements of the symmetric tensor are $\sigma_{11}$, $\sigma_{22}$ and $\sigma_{33}$ where $\sigma_{11} \leq \sigma_{22} \leq \sigma_{33}$ by convention.

The three principal elements are frequently expressed instead as the isotropic value $\sigma_{iso}$, shielding anisotropy $\Delta\sigma$, and the asymmetry $\eta$. These quantities are defined from the principal elements as follows:

31

$$\sigma_{iso} = \frac{1}{3}\left(\sigma_{11} + \sigma_{22} + \sigma_{33}\right) \qquad (3.17)$$

$$\Delta\sigma = \sigma_{33} - \sigma_{iso} \qquad (3.18)$$

$$\eta = \frac{(\sigma_{11} - \sigma_{22})}{\sigma_{33}} \qquad (3.19)$$

## 3.5. The Spin-Coupling Interaction

An indirect spin-spin coupling interaction can occur between two nuclear spins $I_A$ and $I_X$ via their bonding electrons. The Hamiltonian for the indirect spin-spin coupling interaction is:

$$\mathcal{H}_J = \mathbf{I_A} \cdot \hat{\mathbf{J}}_{AX} \cdot \mathbf{I_X} \qquad (3.20)$$

where $\hat{\mathbf{J}}$ is the indirect spin-spin coupling tensor. Analogous to $\hat{\sigma}$, in the principal axis system $\hat{\mathbf{J}}$ is converted to its diagonal form with three principal elements $J_{11}$, $J_{22}$ and $J_{33}$. The trace of $\hat{\mathbf{J}}$ is non-zero and thus in solution, as a result of motional averaging, an average value is seen:

$$J_{iso} = \frac{1}{3}(J_{11} + J_{22} + J_{33}) \qquad (3.21)$$

As can be seen in Equation (1.20) the spin-coupling interaction is independent of the applied magnetic field. The spin-coupling interaction is generally much smaller than the other interactions but remains a valuable tool for the elucidation of chemical structures.

## 3.6. The Spin Rotation Interaction

The spin-rotation interaction is the interaction between the spin angular momentum, **I**, of the nucleus and the rotational angular moment, **J**, of the molecule or part of the molecule. As a molecule or molecular fragment rotates, the movement of electrons and nuclei generate small electric currents, which in turn induce small magnetic fields. Since the reorientational motion is not continuous, that is it proceeds by a series of random jumps, the magnetic field felt at the nucleus is fluctuating.

The Hamiltonian for the spin-rotation interaction is:

$$\mathcal{H}_{SR} = \hbar \mathbf{I} \cdot \hat{\mathbf{C}} \cdot \mathbf{J} \tag{3.22}$$

where $\hat{\mathbf{C}}$ is the spin-rotation coupling constant tensor.

The spin-rotation interaction is directly proportional to the rate of molecular motion and thus is most important for small molecules, molecules in the gas phase and molecules at high temperatures. The interaction is never directly observed in NMR spectra; however it can contribute to spin-lattice relaxation.

## 3.7. The Quadrupolar Interaction

The majority of NMR active nuclei have spin quantum number I > ½, that is, they are quadrupolar. Quadrupolar nuclei possess a nuclear quadrupole moment (a nuclear property, eQ) in addition to the magnetic moment, $\mu$, possessed by I≠0 nuclei. The nuclear electric quadrupole moment results from the asymmetric distribution of charge within the nucleus, making eQ either positive or negative (Figure 3.1).
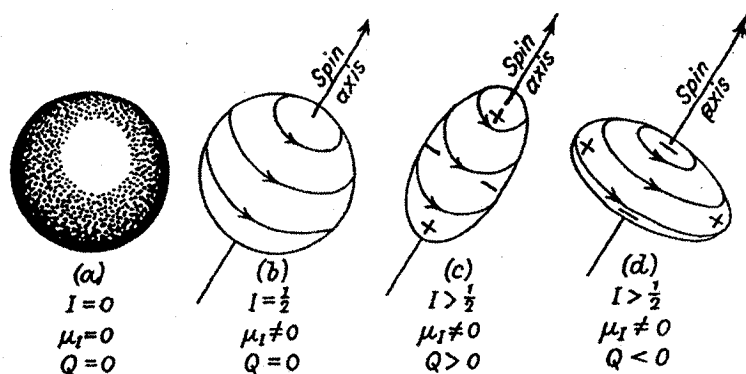
**Figure 3.1**    Charge distribution for a nucleus (a) which does not spin (*i.e.* I=0), (b) which has I=1/2, and (c) and (d) which has I>1/2 [65].

It is the interaction of this quadrupole moment with the electric field gradient (a molecular property, efg) at the nucleus that gives rise to the quadrupolar interaction. The Hamiltonian for the quadrupolar interaction is:

$$\mathcal{H}_Q = \mathbf{I} \cdot \hat{\mathbf{Q}} \cdot \mathbf{I} \tag{3.23}$$

where $\hat{\mathbf{Q}}$ is the quadrupolar tensor which characterizes the three-dimensional nature of the interaction, defined as:

$$\mathbf{Q} = \frac{eQ}{2I(2I-1)\hbar} \cdot \hat{\mathbf{V}} \tag{3.24}$$

where $\hat{\mathbf{V}}$ (often written as **eq**) is the efg tensor at the nucleus. In the principal axis system, the efg tensor is converted into its diagonal form, to give the principal components, $V_{11}$, $V_{22}$ and $V_{33}$. The trace of the efg tensor at a nucleus is zero, thus the following relationship holds:

$$V_{11} + V_{22} + V_{33} = 0 \tag{3.25}$$

The shape of the electric field gradient is described in terms of the asymmetry parameter, $\eta_Q$, which can be defined as:

$$\eta_Q = \frac{V_{22} - V_{11}}{V_{33}} = \frac{eq_{22} - eq_{11}}{eq_{33}} \qquad (3.26)$$

where $|V_{11}| \geq |V_{22}| \geq |V_{33}|$. A special case for the asymmetry parameter is when the efg is axially symmetric about the principal axis. That is, when $V_{11} = V_{22} \neq V_{33}$ and thus $\eta_Q = 0$.

Since the quadrupole moment couples to the electric field gradient, the quadrupolar interaction is very sensitive to the electronic structure at the nucleus. The strength of the interaction is given by the quadrupolar coupling constant (QCC), $\chi$:

$$\chi = \frac{eQV_{33}}{h} = \frac{eQeq_{33}}{h} \qquad (3.27)$$

# 4. Solid State NMR

There is one aspect of solid-state NMR spectroscopy that makes it very different from solution NMR: the orientation dependence (or anisotropy) of some of the nuclear interactions. In solutions molecular motion is random and rapid on the NMR timescale. As a result both the dipolar interaction and the quadrupolar interaction are eliminated through averaging; only the averaged values of the chemical shifts and spin-spin couplings are usually observable in solution NMR. In solids, molecules are generally not free to rotate and as a result, the anisotropic interactions are not completely averaged. For nuclei with spin I=1/2 this anisotropy is largest for the dipolar and chemical shift interactions; for nuclei with spin I>1/2 the anisotropy is usually largest for the quadrupolar interaction.

## 4.1. Anisotropy of the Dipolar Interaction

For a single crystal with only one orientation of the internuclear vector $\mathbf{r}$, a spectrum of two lines is observed with the peak separation (for a homonuclear spin pair) given by:

$$\Delta v(\text{homo}) = v_0 \pm \frac{\mu_0}{4\pi} \frac{\hbar}{2\pi} \frac{\gamma_A^2}{r_{AA}^3} \frac{3}{2} \left( 3\cos^2\theta_{AA} - 1 \right) \tag{4.1}$$

where $\theta_{AA}$ is the angle between the internuclear vector and the magnetic field, $\mu_0$ is the magnetic permeability constant, and $v_0$ is the resonance frequency in the absence of dipolar interactions. For a heteronuclear spin-pair, the spectrum of the A or X nucleus would yield a doublet with a splitting of:

36

$$\Delta v(\text{hetero}) = v_o \pm \frac{\mu_0}{4\pi} \frac{\hbar}{2\pi} \frac{\gamma_A \gamma_x}{r_{AX}^3} \frac{1}{2}\left(3\cos^2\theta_{AX} - 1\right) \qquad (4.2)$$

In a polycrystalline sample, all possible orientations of **r** exist and thus Equations 4.1 and 4.2 must be summed over all values of $\theta$, resulting in a powder pattern spectrum.

## 4.2. Anisotropy of the Chemical Shift Interaction

In solution, an average or isotropic value of the chemical shift, $\sigma_{iso}$ is observed due to motional averaging:

$$\sigma_{iso} = \frac{1}{3}\left(\sigma_{11} + \sigma_{22} + \sigma_{33}\right) \qquad (4.3)$$

However, in the solid state, molecules are not generally free to rotate, and as a result the shielding will be characteristic of a particular orientation of the molecule with respect to the magnetic field.

In a single crystal, an isolated nucleus results in a sharp signal with a frequency that depends on the fixed orientation of the crystal with respect to the applied magnetic field, $\mathbf{B_0}$. The angular dependence of such a frequency can be described using the following equation:

$$v_{obs} = v_o - v_o\left(\sigma_{11}\sin^2\theta\cos^2\phi + \sigma_{22}\sin^2\theta\sin^2\phi + \sigma_{33}\cos^2\theta\right) \qquad (4.4)$$

where $\theta$ is the angle between $B_0$ and $\sigma_{33}$ and $\phi$ is the angle between the projection of $B_0$ onto the plane defined by $\sigma_{11}$ and $\sigma_{22}$ (see Figure 4.1).
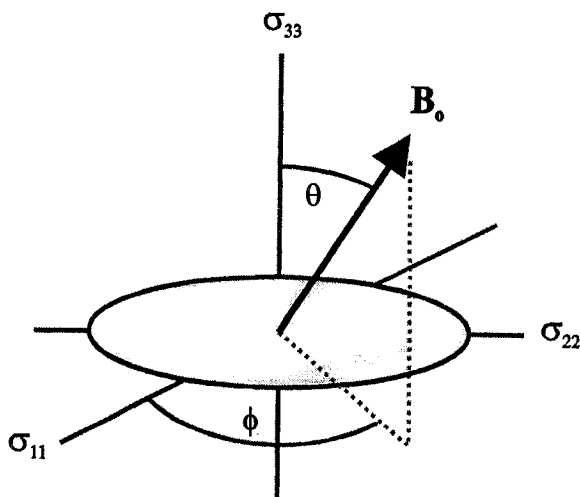
**Figure 4.1    Orientation of $B_0$ in the PAS of the chemical shielding tensor.**

Alternatively, the chemical shift frequency can be expressed in terms of the isotropic component ($\sigma_{iso}$), shielding anisotropy ($\Delta\sigma$) and asymmetry parameter ($\eta$) (see Section 1.4 for definitions):

$$v_{obs} = v_o - v_o\sigma_{iso} - \frac{1}{2}v_o\Delta(3\cos^2\theta - 1 + \eta\sin^2\theta\cos 2\phi) \qquad (4.5)$$

In a polycrystalline sample all orientations are possible, thus the net signal is the sum of all random orientations of the individual crystallites. The resulting spectrum is a broad line with a shape that depends on $\sigma_{11}$, $\sigma_{22}$ and $\sigma_{33}$.

The anisotropic nature of the chemical shift interaction is show in Figure 4.2. When all three tensor components are unique, that is $\sigma_{11} \neq \sigma_{22} \neq \sigma_{33}$, the powder pattern is considered axially asymmetric. On the other hand, a powder pattern is considered to be axially symmetric when two of the principal elements are identical, i.e., $\sigma_{11} = \sigma_{22} \neq \sigma_{33}$. If all of the components are equal, that is $\sigma_{11} = \sigma_{22} = \sigma_{33}$, the interaction is isotropic, this is often referred to as the spherically symmetric case.

38
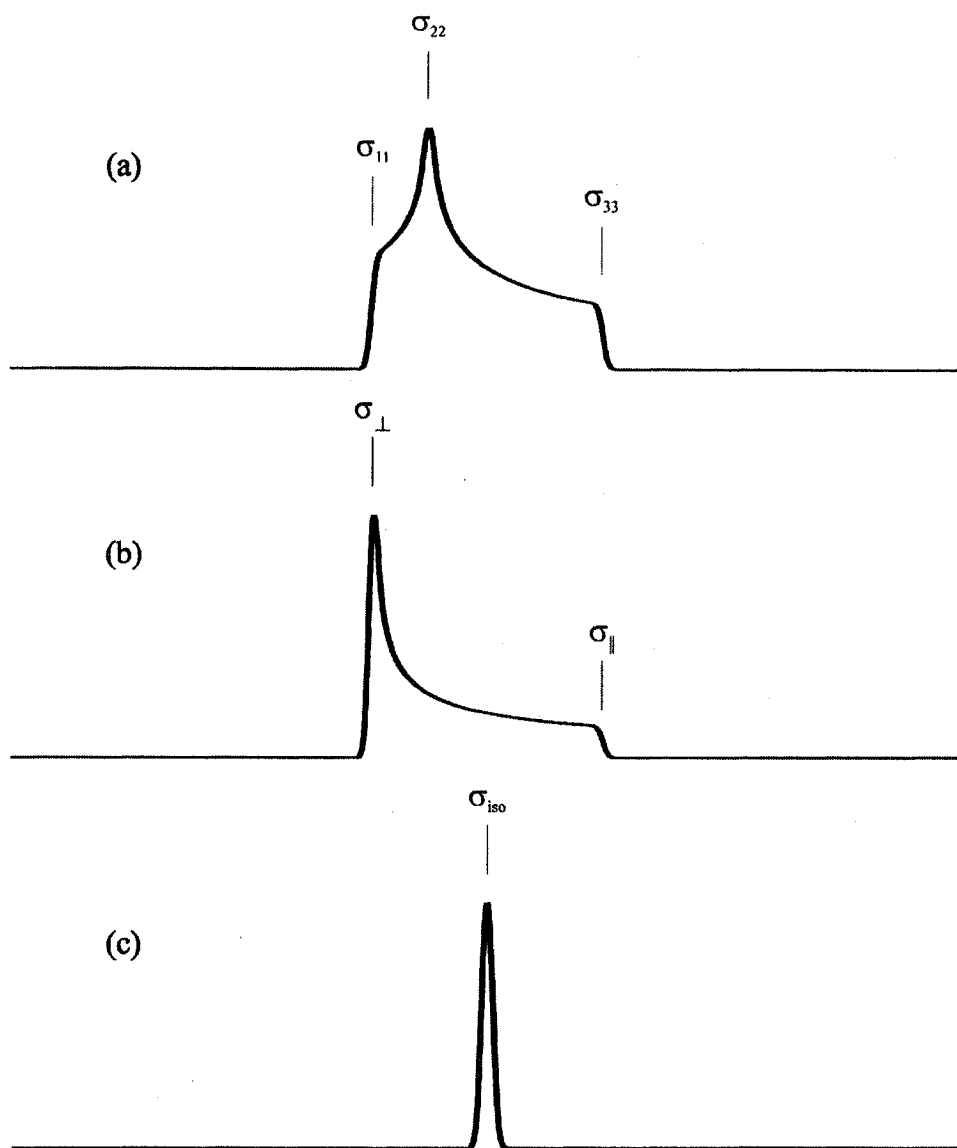
**Figure 4.2**  Schematic powder patterns under the influence of chemical shift anisotropy. (a) Asymmetric (b) axially symmetric and (c) isotropic. Adapted from [62].

## 4.3.  Anisotropy of the Quadrupolar Interaction

The anisotropy of the quadrupolar interaction dominates the lineshape of deuterium spectra and thus will be discussed separately in Section 5.

## 4.4. Line Narrowing Techniques

One of the major difficulties facing solid state NMR spectroscopists is the interpretation of the complicated lineshapes (which result from the anisotropic interactions). In order to obtain high-resolution, high-sensitivity spectra, several line-narrowing techniques are routinely employed including: cross polarization, high power decoupling and magic angle spinning.

### 4.4.1. High-Power Decoupling

Nuclear spin decoupling is a technique of great importance for the simplification and improvement of resolution of NMR spectra. The general idea of the spin decoupling technique, first proposed by Bloch [66], is to observe the behaviour of a rare spin system, S, while applying a second oscillating field, $B_2$, with relatively high strength in the vicinity of the Larmour frequency of an abundant spin system, I. The result is a suppression of the dipolar interaction, and thus an overall narrowing of the line.

In order to obtain complete decoupling, the amplitude of the irradiation field must be larger than the strength of the I-S dipolar interaction. In solid samples this means hundreds of watts of power whereas in solution only 2-3 watts are used. Thus in the solid state this technique requires high powered amplifiers.

### 4.4.2. Magic-Angle Spinning

Magic angle spinning (MAS) is used in the majority of NMR experiments, where its primary goal is to assist in the removal of heteronuclear dipolar-coupling effects and to remove the effects of chemical shift anisotropy.

In solution NMR spectra, effects of chemical shift anisotropy and dipolar coupling are rarely observed. The rapid tumbling of molecules in solution causes the angle $\theta$ to be average over all possible values. This in turn averages the $(3\cos^2\theta\text{-}1)$ dependence of the transition frequencies (refer to Equations 4.1, 4.2 and 4.5) to zero on the NMR timescale, i.e. rate of change of molecular reorientation is fast relative to the chemical shift anisotropy, dipole-dipole coupling, etc.

Magic angle spinning, a technique developed by Lowe and Andrew [67,68], achieves this same result for solids. If a sample is spun about an axis inclined at an angle $\theta_R$ to the applied field, then $\theta$, the angle describing the orientation of the interaction tensor in a molecule within the sample, varies with time. Under these circumstances, the average of $(3\cos^2\theta\text{-}1)$ is:

$$\left\langle 3\cos^2\theta \right\rangle = \frac{1}{2}(3\cos^2\theta_R - 1)(3\cos^2\beta - 1) \tag{4.6}$$

where the angles $\beta$ and $\theta_R$ are defined in Figure 4.3. The angle $\beta$ is fixed for a given nucleus in a rigid solid, but it takes on all possible value in a powder sample. The angle $\theta_R$ is a variable controlled by the experimenter and if set to $54.74°$, then $\left\langle 3\cos^2\theta - 1 \right\rangle$ is zero. Thus, provided that the spinning rate is fast so that $\theta$ is averaged rapidly compared with the anisotropy of the interaction, the interaction anisotropy is averaged to zero.

This technique averages the anisotropy associated with *any* interaction which causes a shift in the energies of the Zeeman spin functions, such as heteronuclear dipolar coupling, chemical shift anisotropy and first-order quadrupolar coupling.
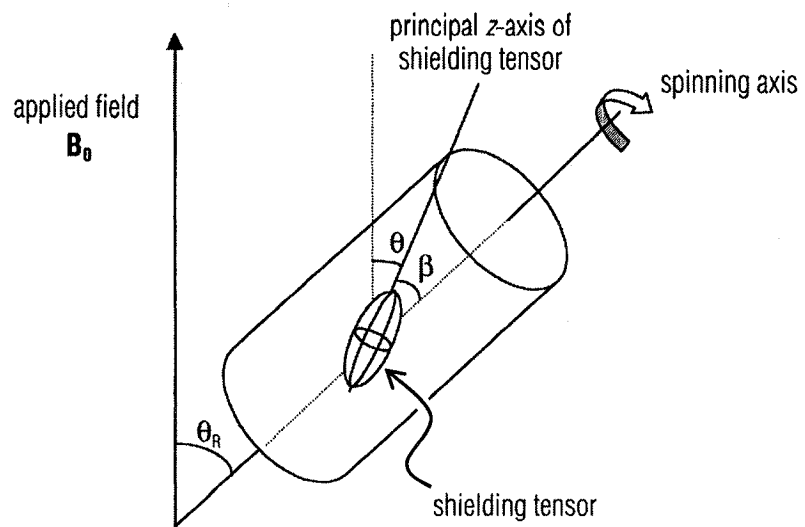
**Figure 4.1    The magic-angle spinning experiment. [69]**

# 5. Solid State Deuterium NMR

In solution, deuterium NMR is of little interest as the NMR properties observed (such as chemical shift) have the same values as those obtained using proton NMR. $^2$H NMR has just two main applications in solution: (1) isotope labelling which can be used by organic chemists to determine reaction mechanisms, and by biologists and biochemists to investigate metabolism, and; (2) T1 measurements which can be employed to study molecular reorientation. On the other hand, the use of solution $^1$H NMR is extremely widespread, stemming from the large natural abundance of $^1$H coupled with its high sensitivity ($^1$H is 690 000 times more receptive than $^2$H).

Based on this, one might expect that $^1$H NMR is the most appropriate technique for studying structural and dynamic aspects of bonding in solids. However, this is not the case as it is generally difficult to record high resolution $^1$H NMR spectra of solids since the strong homonuclear $^1$H-$^1$H dipole-dipole interaction leads to spectra that are typically broad and featureless. $^2$H NMR also tends to win out over $^1$H NMR, as $^1$H NMR spectra provide structural information derived primarily from one interaction: the chemical shift. However, $^2$H NMR spectra allow for structural information to be obtained from both the quadrupole coupling parameters *and* chemical shift parameters.

## 5.1. Effects of the Quadrupolar Interaction

For solid state deuterium NMR (nuclear spin I = 1), the Zeeman interaction ($\mathcal{H}_Z$) and the quadrupolar interaction ($\mathcal{H}_Q$) dominate to the extent that the other terms, such as dipolar interactions, anisotropic chemical shifts and indirect spin-spin couplings may be

neglected to a first approximation. This allows the Hamiltonian to be re-written as:

$$\mathcal{H} = \mathcal{H}_Z + \mathcal{H}_Q \tag{5.1}$$

The dipolar interaction is manifested as line broadening in the $^2H$ powder spectrum.

The primary interaction, the Zeeman interaction, will cause the normal energetically degenerate nuclear spin states of $^2H$ to become discrete. In an external magnetic field, in the absence of any electric field gradient at the nucleus, the Zeeman interaction splits the ground state nuclear energy levels of $^2H$ as shown in Figure 5.1 (a). Thus, two resonance peaks will be observed at $v_o = \gamma_D B_o/2\pi$, due to the transitions from the m=+1 → m=0 and m=0 → m=-1 spin states. Both of these peaks will occur at the same frequency since the energy level splittings are the same for both transitions.

The $^2H$ nucleus, with I=1, possesses an electric quadrupole moment, eQ, which interacts with the efg of the local charge distribution, yielding a shift of these nuclear Zeeman levels. This effect is illustrated in Figure 5.1 (b). The presence of the efg causes the m=+1 → m=0 transition to be compressed by three energy units, while the m=0 → m=-1 transition is expanded by three energy units. This perturbation modifies the energy of the different spin states according to:

$$\Delta v_{m-1 \leftrightarrow m} = \frac{3(eq)(eQ)}{4I(2I-1)\hbar} \left( \frac{3\cos^2\theta - 1}{2} + \frac{\eta_Q \sin^2\theta \cos 2\phi}{2} \right)(1-2m) \tag{5.2}$$

where $\Delta v$ is the separation in frequency units, and $\theta$ and $\phi$ specify the orientation of the efg tensor with respect to the magnetic field vector as shown in Figure 5.2.
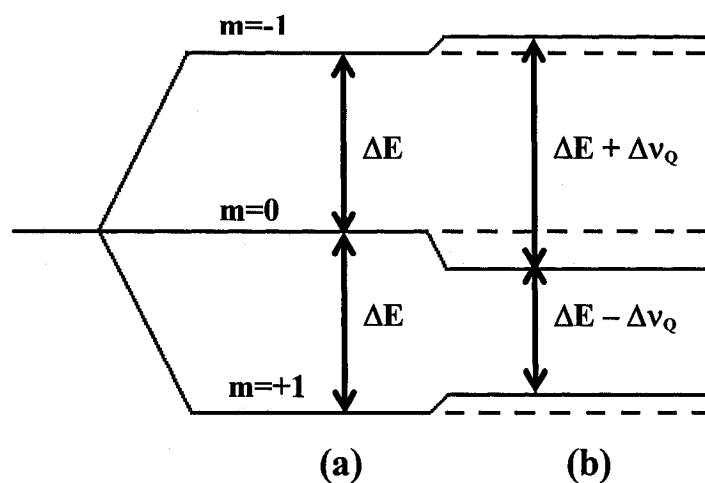
**Figure 5.1** Energy levels of a spin 1 nucleus: (a) splittings due to the Zeeman interaction; (b) first order quadrupolar shifts of the Zeeman levels.
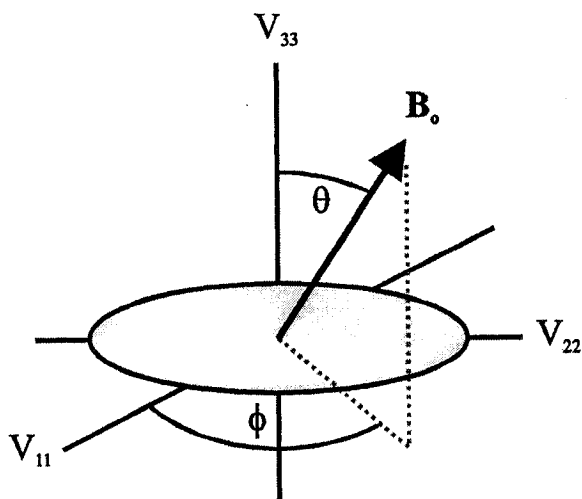


**Figure 5.2** Polar angles ($\theta$, $\phi$) that specify the orientation of the external magnetic field, $B_o$, in the principal axis of the electric field gradient tensor ($V_{11}, V_{22}, V_{33}$).

It is relatively difficult in powder studies to distinguish the effects of slight non-axial symmetry (*i.e.* $\eta_Q > 0$) from those of dipolar broadening. Thus, for typical X–H bonds axial symmetry can be assumed and Equation 5.2 can be reduced to:

$$\Delta v_{m-1 \leftrightarrow m} = \frac{3\chi}{4}(3\cos^2\theta - 1)$$

(5.3)

A single crystal containing a single type of $^2H$ has a spectrum consisting of two signals whose peak separation reflects the angle between the largest component of the efg tensor, $V_{33}$, and the magnetic field vector, as shown in Figure 5.3.
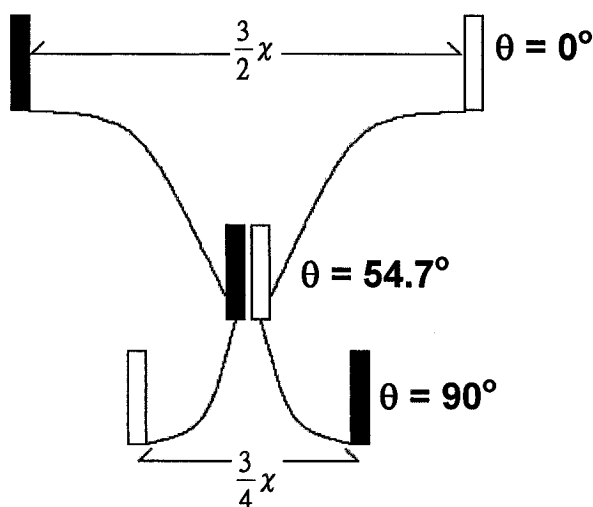


**Figure 5.3**    **Variation of doublet peak separation with $\theta$ (Equation 4.3).**

In a polycrystalline powder sample in which the crystallites are oriented in all possible directions, the transition frequencies are distributed as a profile. The two complimentary patterns, termed the "Pake doublet" [70], correspond to all possible orientations of $V_{33}$ with respect to the magnetic field. The singular peaks of the Pake pattern correspond to the numerous crystallites for which $eq_{33}$ is perpendicular to the

magnetic field. The two low edges of the Pake pattern correspond to the relatively few crystallites where $V_{33}$ lies parallel to the magnetic field.

If axial symmetry is not present, that is $\eta_Q > 0$, the appearance of the Pake pattern changes significantly. Spectra corresponding to various values of the asymmetry parameter are shown in Figure 5.4. The lineshape of the Pake pattern can be described in terms of the quadrupolar coupling constant, $\chi$, and the asymmetry parameter, $\eta$:

$$\Delta \nu_1 = \Delta \nu_{xx} = \frac{3}{4}\chi(1-\eta_Q)$$

$$\Delta \nu_2 = \Delta \nu_{yy} = \frac{3}{4}\chi(1+\eta_Q) \qquad (5.4)$$

$$\Delta \nu_3 = \Delta \nu_{zz} = \frac{3}{2}\chi$$

$\Delta\nu_{xx}=\Delta\nu_{yy}$

$\Delta\nu_{zz}$

$\eta_Q=0$

$\Delta\nu_{xx}$

$\Delta\nu_{yy}$

$\Delta\nu_{zz}$

$\eta_Q\neq0$

$\Delta\nu_{xx}$

$\eta_Q=1$

$\Delta\nu_{yy}=\Delta\nu_{zz}$
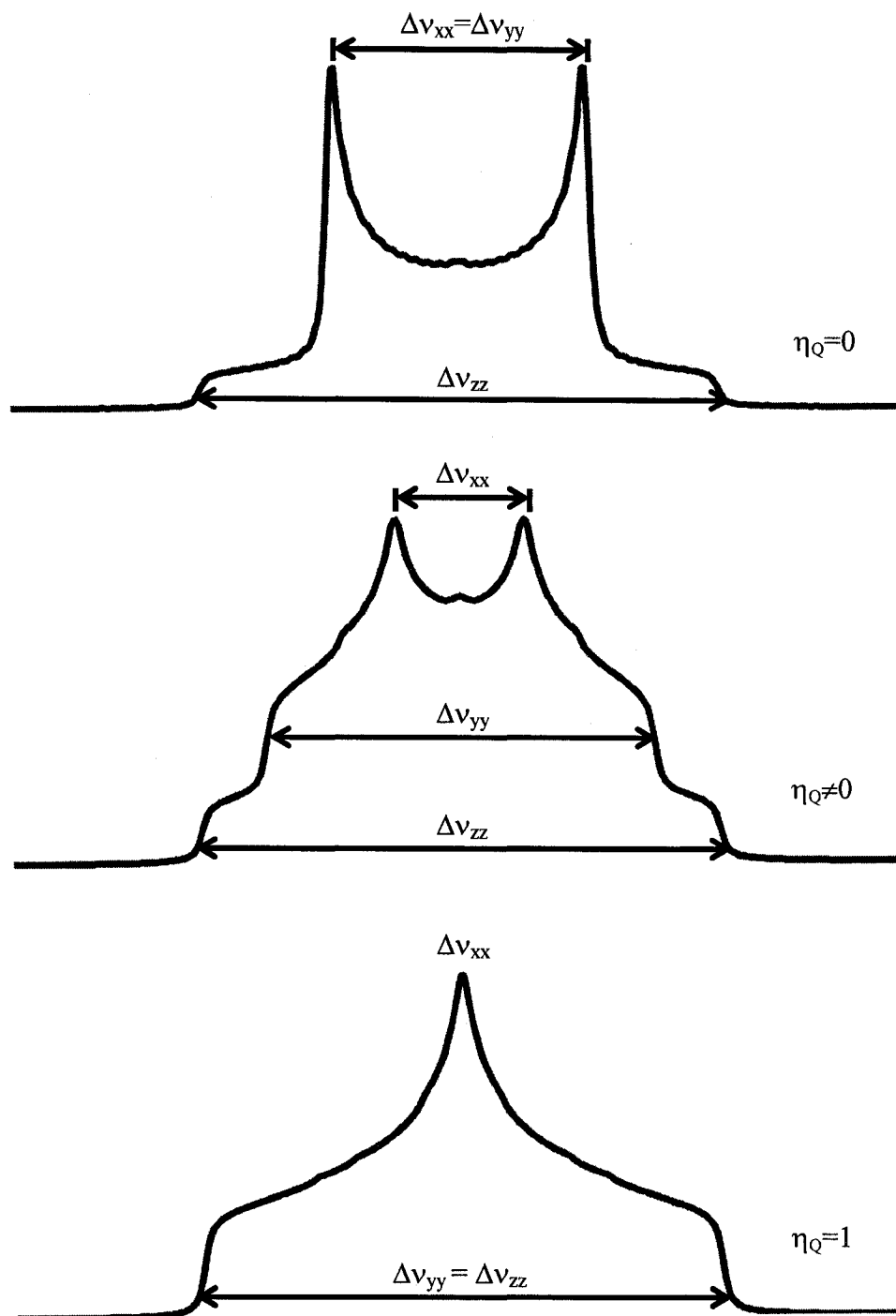
**Figure 5.4     Typical static powder spectra for spin-1 nuclei.**

## 5.2. Effects of Chemical Shift Anisotropy

Though the Zeeman and quadrupolar interactions normally dominate the lineshape of $^2H$ spectra, there are cases where the effect of the chemical shielding interaction cannot be ignored. When the magnitude of the chemical shielding anisotropy becomes comparable to that of the quadrupolar interaction the energy level diagram changes, as illustrated in Figure 5.5.
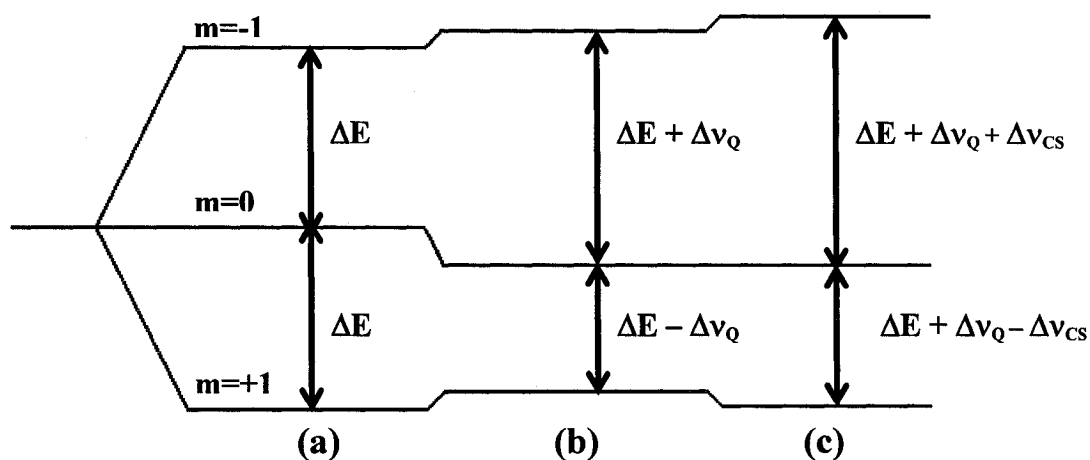
**Figure 5.5**    Energy levels of a spin 1 nucleus with splittings due to: (a) Zeeman interaction; (b) first order quadrupolar interaction; (c) chemical shift interaction.

As a result, the resonance frequencies in a single crystal spectrum follow the expression:

$$v_{m-1\leftrightarrow m} = v_o + v_{CS} + \Delta v_{m-1\leftrightarrow m} \tag{5.5}$$

and the powder spectra are distorted with respect to those shown in Figure 5.5. Equation 5.5 cannot be evaluated as $v_{CS}$ and $\Delta v_{m-1\leftrightarrow m}$ are characterized with respect to two different frames, that is $\hat{\sigma}$ for the former and $\hat{V}$ for the latter. Thus, in order to evaluate the expression, Euler angles ($\alpha$, $\beta$, $\gamma$) must be employed. The angles $\alpha$, $\beta$ and $\gamma$ represent the sequential rotations to bring the efg tensor PAS into coincidence with the shielding

49

tensor PAS: rotation of $\alpha$ about the $V_{33}$ direction; rotation of $\beta$ about the new direction of

$V_{22}$; rotation of $\gamma$ about the new direction of $V_{33}$. The angle $\beta$ may also be visualized as

the angle between the two largest components of the tensors, as seen in Figure 5.6. All

rotations are performed in a mathematically positive direction, that is, counter-clockwise.
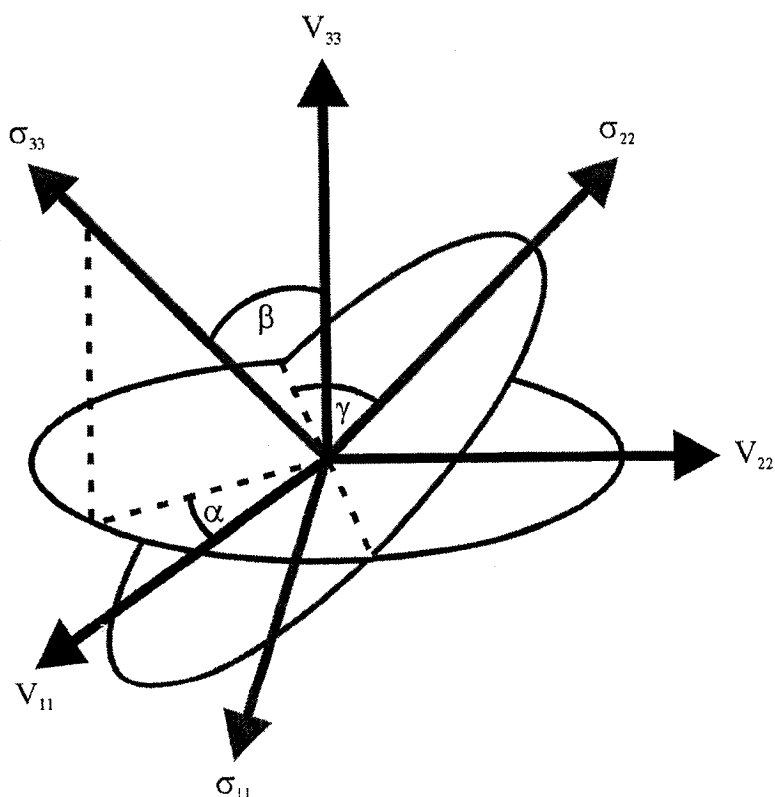


**Figure 5.6     Euler angles relating the $\hat{\sigma}$ PAS to the $\hat{V}$ PAS.**

Figure 5.7 shows typical NMR powder for a spin $I=1$ nucleus, assuming both

axial symmetry (*i.e.* $\eta = \eta_Q = 0$) and coincident $\hat{V}$ and $\hat{\sigma}$ (*i.e.* $\alpha = \beta = \gamma = 0°$). As

illustrated in Figure 5.7, as the chemical shielding contribution increases relative to the

quadrupolar contribution, the spectra gradually change for a Pake doublet to a classic

CSA powder pattern. In cases where $\mathcal{H}_{CS} < \mathcal{H}_Q$, the spectra show unsymmetrical Pake patterns since the chemical shielding contribution serves to compress one transition while stretching the other. In cases where $\mathcal{H}_{CS} > \mathcal{H}_Q$, the spectra resemble CSA patterns with distortions.

$\Delta\sigma \ggg \chi$

$\Delta\sigma = 0.2\chi$

$\Delta\sigma = \chi$

$\Delta\sigma = 5\chi$

$\Delta\sigma \lll \chi$
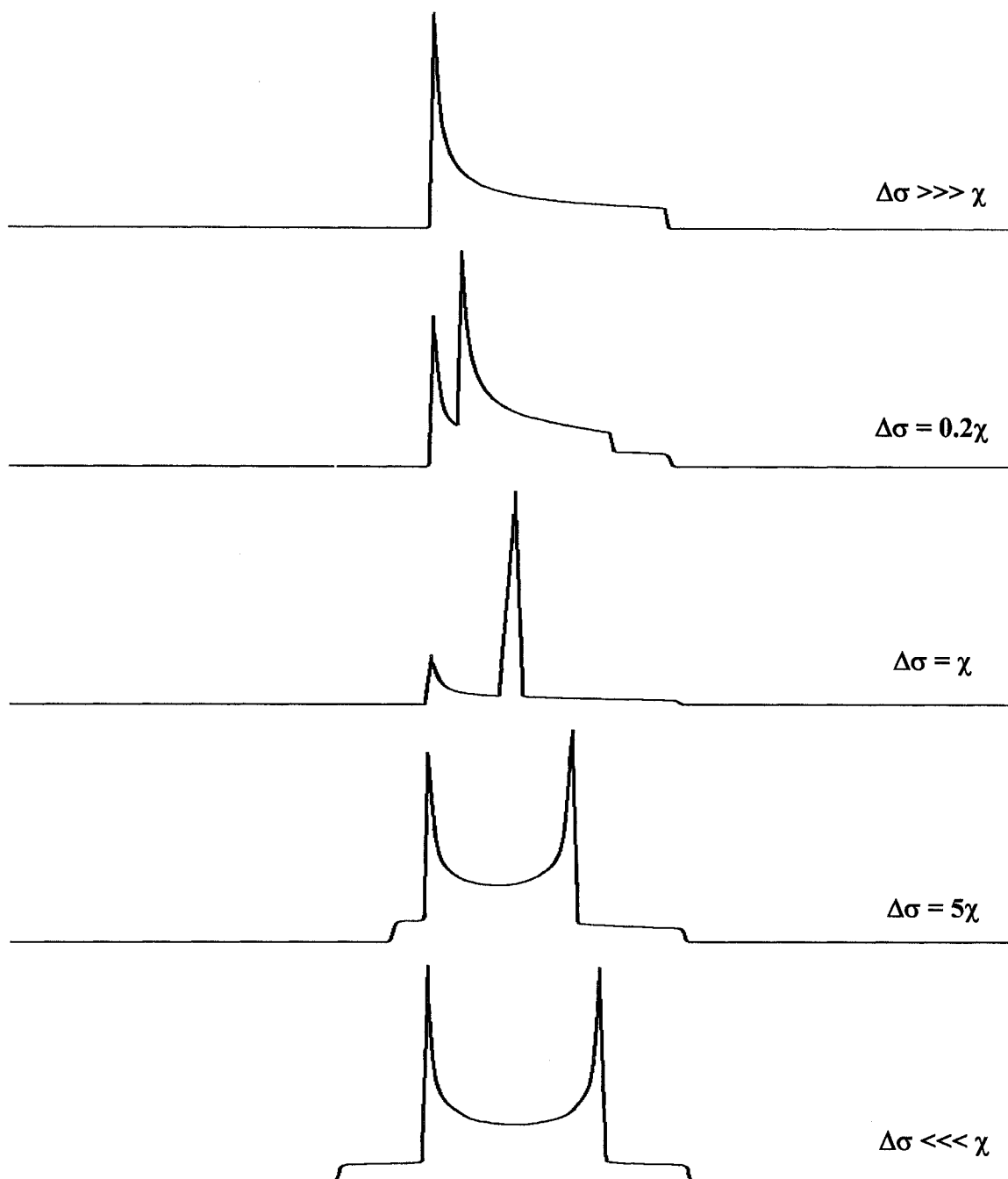
**Figure 5.7**     **Effect of the chemical shift interaction on the lineshape of a quadrupolar nuclei. All spectra were simulated assuming $\eta_Q=0$ and $\eta_{CS}=0$.**

## 5.3. Effects of Magic-Angle Spinning

Both the quadrupolar interaction and the chemical shift anisotropy, the two interactions which dominate $^2$H spectra, can be averaged by magic angle spinning. In order for MAS to reduce a powder pattern to a single line, the rate of the sample spinning must be fast in comparison to the anisotropy of the interaction being spun out. "Fast" in this context means a spinning speed that is 2 times greater than the anisotropy. In the case of $^2$H it is quite feasible to spin at a speed which averages the chemical shift anisotropy (10 kHz spinning is sufficient), but impossible to spin at a speed which averages the quadrupolar interaction (150-400 kHz spinning is required). Currently, spinning speeds of up to 50 kHz are achievable, with 10 kHz being routine on a modern spectrometer.

Slower spinning results in a set of spinning sidebands in addition to the central resonance at the isotropic chemical shift. The spinning sidebands are a set of narrow lines separated by the spinning speed. The overall shape of the spinning sideband manifold is dictated by the quadrupole parameters ($\chi$ and $\eta$) and the chemical shift anisotropy. Examples of spinning sideband patterns are given in Figure 5.8.
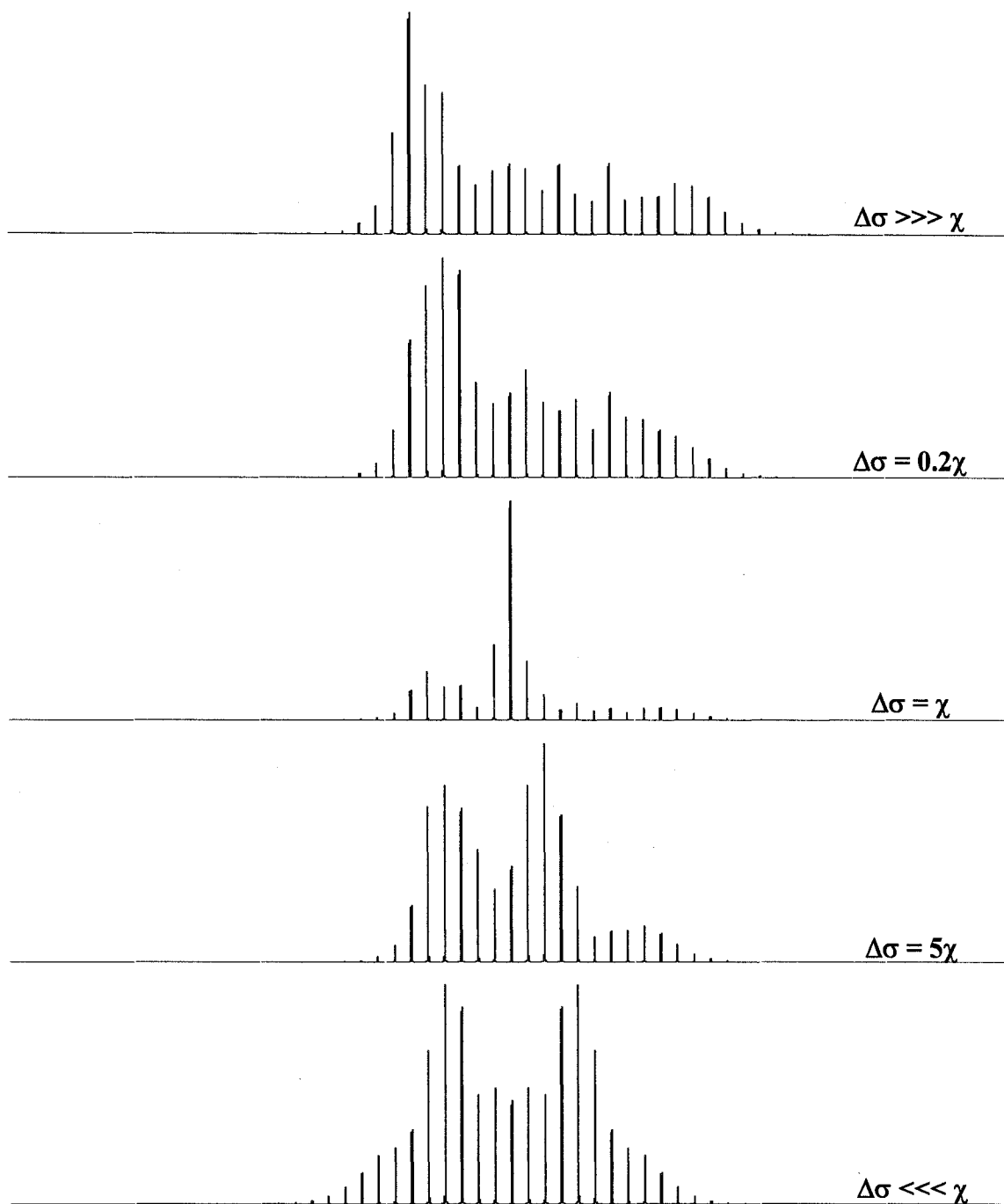
**Figure 5.8**    **Effect of magic-angle spinning on the lineshape of a quadrupolar nucleus, where $\eta_Q=0$ and $\eta_{CS}=0$.**

# 6. The Effect of Hydrogen Bonding on $^2$H NMR Parameters

$^2$H NMR is a powerful technique for studying the structural properties of hydrogen bonded solids. Since the structures of numerous hydrogen-bonded crystals have been determined via X-ray and neutron diffraction, it is possible to make use of these substances as model systems in order to elucidate how characteristic NMR parameters such as the deuterium quadrupolar coupling constant, the isotropic chemical shift, or the chemical shift anisotropy are correlated with structural properties of hydrogen bonds.

## 6.1. Quadrupolar Parameters

The electric field gradient at a nucleus depends on the charge distribution around the nucleus; therefore the efg of a $^2$H nucleus in a crystalline solid depends on the crystal structure. The quadrupole interaction parameters, $\chi$ and $\eta$, are defined in terms of elements of the efg tensor (see Section 1.7) and thus are expected to depend on the bonding arrangement as well.

It was Chiba in 1964 [71] who first proposed a correlation between $^2$H QCCs and hydrogen bonding arrangements. Chiba found that short, strong hydrogen bond systems have smaller QCCs than do long, weak hydrogen bonds. Similar correlations were seen in studies by Blinc and Hadzi in 1966 [72] and Soda and Chiba in 1969 [73].

Attempts were made to derive an empirical relationship between the magnitudes of $^2$H QCCs and hydrogen bond lengths. Initially Soda and Chiba proposed a $(r_{H\cdots O})^{-3}$ dependence of $e^2qQ/h$, in the form:

$$(e^2qQ/h) = A - B(r_{H\cdots O})^{-3} \qquad (6.1)$$

where $e^2qQ/h$ is in units of kHz and $r_{H\cdots O}$ is in units of Å.

However, based on the bond polarization theory [74], it was suggested instead that the QCC is proportional to $(r_{H\cdots O})^{-1}$. This suggestion was confirmed with experimental data for deuterated salts, for which the following relationship was derived [75]:

$$(e^2qQ/h) = A - B(r_{H\cdots O})^{-1} \tag{6.2}$$

where $e^2qQ/h$ is in units of kHz and $r_{H\cdots O}$ is in units of nm.

[2]H QCCs have also been correlated to other aspects of hydrogen bond geometry. Kalsbeek et al. investigated the influence of the asymmetry of a hydrogen bond on values of ^{2}H QCCs [76]. In accordance with the early work of Blinc and Hadzi [72], it was found that in systems where the O$\cdots$O hydrogen bond lengths are comparable, it is the asymmetry of the hydrogen bond (the difference in O–H and H$\cdots$O) that determines the value of the ^{2}H QCC, as seen in Figure 6.1. QCC values for ^{2}H in short symmetric hydrogen bonded systems were in the range 53-59 kHz, with larger values of up to 166 kHz found in systems with short asymmetric hydrogen bonds.

More recently, Zhao et al. [77] studied two systems with extremely short hydrogen bonds: 3-cyano-2,4-pentanedione and 4-cyano-2,2,6,6-tetramethyl-3,5-heptanedione. The latter, in particular, has the shortest O$\cdots$O distance of any O$\cdots$O hydrogen bonded system. In agreement with previous studies, these compounds were found to possess very small QCCs: a mere 96 kHz and 76 kHz respectively.

Correlations between ^{2}H quadrupole parameters and hydrogen bond geometry have been considered for situations other than O–H$\cdots$O hydrogen bonds. Ono et al. [78] studied ^{2}H labeled amino acids, peptides, and polypeptides and found that the QCC values decreased with a decrease in $R_{N\cdots O}$ (Figure 6.2).
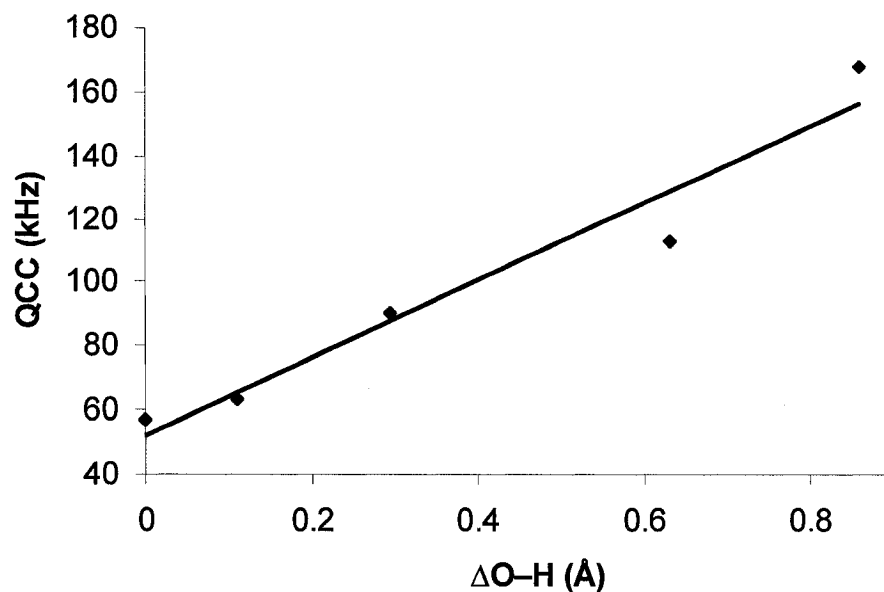
**Figure 6.1**    Correlation of the asymmetry of the hydrogen bond (given as a difference in O···H and H···O bond lengths with the QCC of the $^2$H in the hydrogen bond. Adapted from [72].
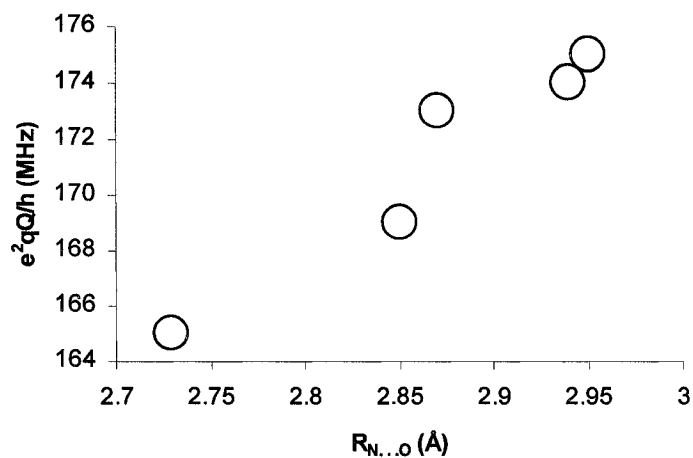


**Figure 6.2**    A plot of the experimental QCC values of N$^2$H-GlyGly, N$^2$H-AlaGly, N$^2$H-PGI, N$^2$H-PGII and N$^2$H-PA against the hydrogen bong length ($r_{N---O}$). Adapted from [78].

The investigation of the effect of hydrogen bonding on $^2$H QCCs has not been limited to experimental studies; several computational studies have also been performed. A systematic study of the methodology for ab initio calculations of $^2$H QCCs was conducted by Camus et al. [79] The study, which focused on the $\alpha$ and $\beta$ polymorphs of oxalic acid dihydrate, showed that calculated QCCs are sensitive to the choice of basis orbitals, particularly those responsible for the distribution of the valence shell charge density. Results also demonstrated the importance of including a neighbouring molecule (dimer) or small cluster of neighbouring molecules, in order to obtain computational predictions in close agreement with experimental values.

Ab initio calculations have also been applied in a study of the geometrical dependence of $^2$H QCCs on the geometry of O–H···O=C hydrogen bonds [80]. Ab initio HF-SCF/6-31G** calculations were carried out as a function of the intermolecular geometry of a formaldehyde-water complex (see Figure 6.3). It was found that the value of $\chi$ depends significantly on the values of all geometric variables; however a *particularly* strong dependence on $r$ was observed.
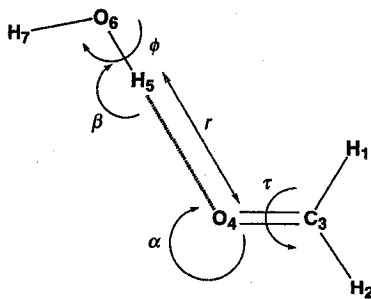


**Figure 6.3**    **Definition of the geometric variables in the formaldehyde-water model complex [80].**

Bailey [81] studied 25 *isolated* molecules, ranging from HD and DF to pyridine and fluorobenzene, in order to determine which basis set and method is most reliable for calculating $^2$H QCCs. Becke's three parameter hybrid method was used in conjunction with the correlation functional of Lee *et al.* [82] with double-split valence basis, designated B3LYP/6-31G. Various combinations of polarization functions were incorporated in the basis, and investigated for the best linear relationship between the calculated efgs and the experimental *gas phase* $^2$H QCCs. Among the various combinations of polarization functions studied, the B3LYP/6-31G(df,3p) model was shown to provide the most accurate results. The results obtained via the B3LYP/6-31G(df,3p) model are comparable to those obtained by Gerber and Huber [83] via MP4 calculations.

Despite a fair number of studies investigating the effect of hydrogen bonding on $^2$H QCCs, there are only a few studies that correlate the asymmetry parameter to molecular geometry. Michal *et al.* [84] were the first to present a relationship between the asymmetry parameter and hydrogen bond geometry. Using experimental data for deuterated salts, it was shown that the effect of the hydrogen bond acceptor on the components of the efg is proportional to the projection of the hydrogen bond on that component. It was also found that the value of the asymmetry parameter was not largely affected by hydrogen bond acceptor variation.

Ab initio calculations have also been applied in a study of the dependence of the asymmetry parameter on specific geometric parameters defining the hydrogen bonded system [80]. Using a water-formaldehyde model system, illustrated in Figure 6.3, it was found that the asymmetry parameter had a particularly strong dependence on $\beta$ and a

moderate dependence on $r$. It was shown that $\eta_Q$ was at a maximum when $\beta=180°$ and

when r (H$\cdots$O distance) was short (see Figure 6.4). The dependence on the other variables

$(\alpha, \phi, \tau)$ was minor.
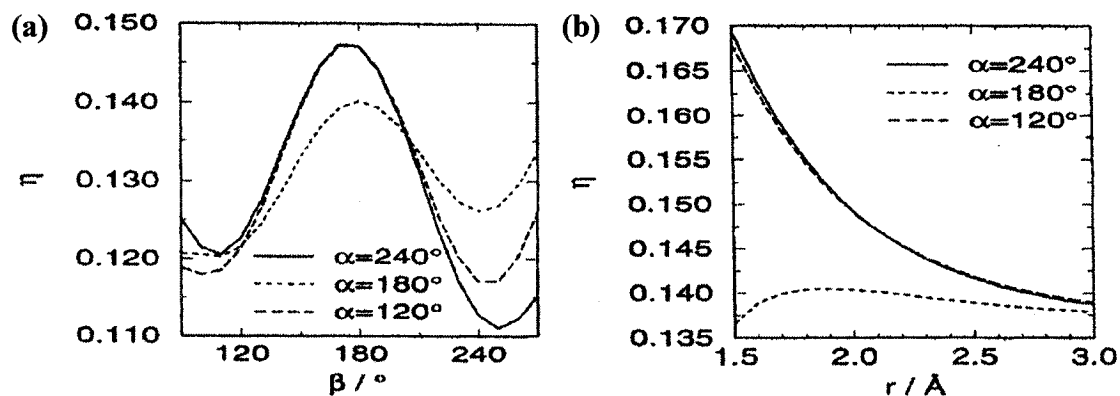


**Figure 6.4**    (a) Plot of $\eta$ as a function of $\beta$ for fixed values of r = 2.1 Å, $\phi$ = 180° and
$\tau$ = 0°. (b) Plot of $\eta$ as a function of r for fixed values of $\beta$ = 180°, $\phi$ = 180° and $\tau$
= 0° [80].

## 6.2. Chemical Shift Parameters

Both the isotropic chemical shift and the chemical shift anisotropy of a crystalline

solid are sensitive to the bonding state. The majority of studies that investigate the effect

of hydrogen bonding on these parameters have been conducted using the ^{1}H isotope of

hydrogen. The values of $\delta_{iso}$ and $\Delta$ are the same for both isotopes of hydrogen, neglecting

an extremely small isotope effect (on the order of ppb), and thus studies focusing on [1]H

and ^{2}H will be highlighted interchangeably.

Berglund and Vaughan [85], Rohlfing, Allen and Ditchfield [52], Jeffrey and

Yeon [86], Harris *et al.* [87], and Yamauchi *et al.* [88] have all observed a correlation

between ^{1}H proton chemical shits and distances in crystals. The first two publications

sought a correlation between O–H···O distances and $\delta_H$, while the third used neutron

diffraction data to extend this to H···O distances resulting in the plot shown in Figure 6.5.

The fourth paper gives values of the carboxylic acid ^{1}H shifts for 83 compounds. A

definite trend is seen as the very strongly hydrogen bonding KH maleate with O···O =

2.437 Å has a chemical shift of 21.0 ppm while the weakly hydrogen bonded tartaric acid

with O···O = 2.909 Å has a chemical shift of just 4.8 ppm.

Correlations between isotropic ^{1}H chemical shifts and hydrogen bonding

geometry have also been reported for situations other than O–H···O. Yamauchi et al. [88]

have shown that the values of $\delta_{iso}$ for the Gly amide protons of Gly-containing peptides

and polypeptides increase as the N···O distance in the N–H···O hydrogen bond decreases.

The chemical shift anisotropy (CSA) also shows a trend toward higher values for

shorter hydrogen bond distances [86, 89]. Earlier studies such as these found that the

relationship between the CSA and H···O was more scattered than the relationship seen

with $\delta_{iso}$ (see Figure 6.6). This result contradicted theoretical studies which indicated that

variations in hydrogen bond geometry should be *more* strongly manifested in the CSA

than in the chemical shift. This contradiction recently prompted further research.
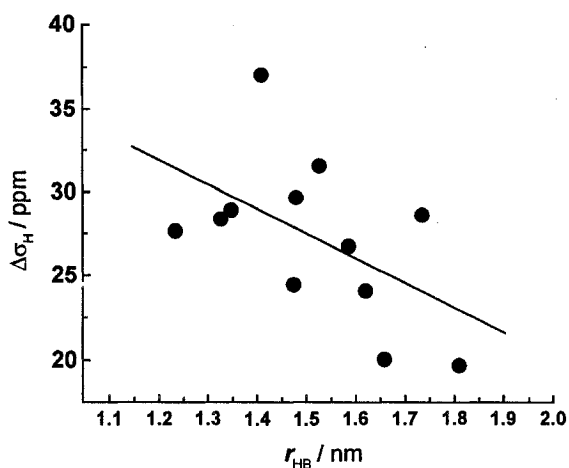


**Figure 6.6**     **Chemical shift anisotropy of hydrogen-bonded protons in various solids plotted as a function of the distance $r_{HB}$. Only substances where $r_{HB}$ is determined by neutron diffraction are considered. The correlation coefficient for the regression curve is 0.536 [86].**

A significantly improved study was undertaken by Wu *et al.* [90] in which a set of

closely related solids was chosen in order to reduce data scatter. In particular, weakly

hydrogen bonded water molecules in magnetically $^1H$ dilute crystalline hydrates were

used for CSA measurements. It was found that the most shielded and least shielded

components of the $^1H$ chemical shift tensor change in opposite directions as a function of

the hydrogen bond distance. Hence, it was confirmed that $^1H$ CSA is a more sensitive

measure of hydrogen bond strength than the $^1H$ isotropic chemical shift.

Hauch *et al.* [91] illustrated that it was possible to determine $^2$H CSAs for polycrystalline samples using $^2$H MAS, provided high magnetic field strengths were employed (14.1 T). It was found that in most cases stronger hydrogen bonds, i.e. linear and symmetric bonds, had larger CSA values.

An improved method of determining $^1$H CSAs in solid powders was developed very recently by Brower and Ripmeester [92]. A two-dimensional NMR experiment on an ultrahigh-field NMR instrument was employed to give high resolution spectra and reliable values of $^1$H CSAs. The study verified past theoretical work which suggested that CSAs are a more powerful indicator of hydrogen bond strength than isotropic chemical shifts.

# 7. The Effect of Deuteration on Hydrogen Bond Geometry

On deuteration of a hydrogen bond the characteristic distances, i.e. the donor

acceptor separation X···A, and the covalent bond length X–H, often change. Such

changes are understood by considering the differences in the potential energy wells for

protonated and deuterated hydrogen bonds. For a weak hydrogen bond the occupied,

zero-point level for the hydrogen stretching vibration in A–H is well below the potential

barrier, and that for deuterium in the isotopomer is still lower because of the mass effect

(Figure 7.1 (a)). Thus, both H and D are essentially confined to the well, as in a normal

chemical bond, and the average X–H distance, $r_{XH}$, is almost the same as the average X–D

distance, $r_{XD}$.
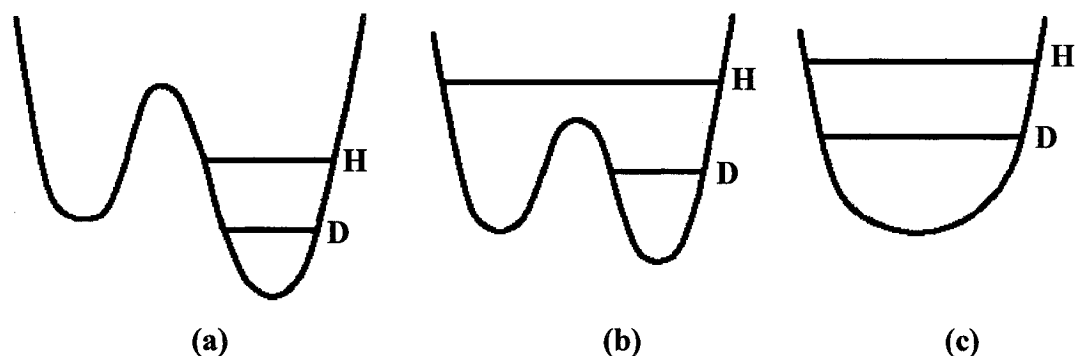


**Figure 7.1**  Potential energy wells for hydrogen bonds, illustrating the zero-point vibrational levels for hydrogen and deuterium. (a) Weak hydrogen bonds; (b) Strong hydrogen bonds; (c) Very strong hydrogen bonds.

For stronger hydrogen bonds, the barrier drops below the zero-point level, first

just for hydrogen and then for hydrogen and deuterium (Figure 7.1 (b)) . As a result, the

average $r_{XH}$ and $r_{XD}$ may differ sufficiently. According to neutron diffraction data, upon

replacing H by D in a strong hydrogen bond, the equilibrium X–H distance decreases by a value on the order of $10^{-2}$ to $10^{-3}$ Å [10, 60, 93]. For very strong hydrogen bonds, for example (FHF)$^-$, the potential function is one with a single minimum (Figure 7.1 (c)), and thus the effect of isotopic substitution is very small.

Abstraction of a deuteron from a hydrogen bond donor (i.e. X–D) is more difficult than abstraction of a proton (i.e. X–H) due to the lower zero-point vibrational energy of deuterium. As a result, the equilibrium X···H distance also varies in compounds with hydrogen bonds upon replacement of hydrogen by deuterium [94]. For strong hydrogen bonds, upon deuteration the X···A distance increases by $10^{-3}$ to $6 \cdot 10^{-2}$ Å [10, 60, 93]. In very strong hydrogen bonds, those with a single-minimum potential well a decrease in the X···A distance is expected (on the order of $10^{-3}$Å) [10, 60, 93].

In most cases, the effect of deuteration on hydrogen bond distances is smaller than the standard uncertainties of the bond lengths [95]. However, sometimes deuteration has a very strong effect: for example, in $KH_2PO_4$ the protonated structure has a tetragonal space group, but the fully deuterated structure has a monoclinic space group [96]. Deuteration, therefore, does change the hydrogen-bond potential energy well, although often by only a small amount.

# 8. Proposed Research

## 8.1 Main Objective

The main objective of the proposed research is to examine hydrogen bonded systems using solid state deuterium NMR. $^2$H NMR can be used, in principle, to study hydrogen bonding since $^2$H is directly involved in the bonds of interest. The $^2$H isotropic chemical shift, chemical shift anisotropy, quadrupolar coupling constant and asymmetry parameter are all sensitive to the bonding state. The degree to which these parameters are affected by hydrogen bonding can be determined experimentally or by quantum chemical calculations. The combination of these methods can provide information regarding the nature of the hydrogen bonds in the systems under study.

## 8.2 $^2$H NMR

$^2$H NMR will be used to study the hydrogen bonded systems, as it is a direct probe of the structurally significant environment. $^1$H NMR is obviously diagnostic of a hydrogen bond as well, but in solid state NMR it is practically impossible to separate the many proton signals, making analysis extremely difficult. By selectively deuterating the compound, such that deuterium is *only* present in the hydrogen bond, analysis becomes straightforward.

## 8.3 Quantum Chemical Calculations

Using a computational quantum chemical program known as Gaussian 03 [97], it is possible to calculate the isotropic chemical shift, CSA, QCC and asymmetry parameter

for the compounds to be investigated. In order to ensure that appropriate basis sets are being used to calculate these NMR parameters, extensive basis set studies will be employed.

Upon determination of the appropriate basis sets, calculations can be undertaken. Crystal coordinates, preferably from neutron diffraction studies, are imported from the Cambridge Crystallographic Database and act as the starting points for the calculation of the various NMR parameters. In cases where neutron data is unavailable, proton positions in X-ray structures are optimized and then the X-ray geometry is used for further calculations.

Quadrupolar and chemical shift parameters for the isolated molecule, dimer, and cluster (up to 6 neighbouring molecules where computational abilities allow) will be calculated. These calculations will determine how much of the hydrogen bonding shell must be included in the calculations in order to give results comparable to those obtained experimentally.

# CHAPTER II

## *EXPERIMENTAL*

# 1.   Sample Preparation

All of the compounds used in this study were purchased from Aldrich, with the exception of 2,4,6–trimethylbenzamide. Since deuterium has a very low natural abundance (0.015%) it was necessary to deuterate the compounds studied. The compounds, with the exception of the triphenylsilylacetylene (TPSiA) – triphenylphosphine oxide (TPPO) complex, were deuterated by dissolving in methan-$d_1$-ol (99%), allowing sufficient time for exchange (~ 30 minutes) and then rotary evaporating to remove the solvent. The deuteration procedure resulted in compounds that included $^2H$ rather than $^1H$ in all labile positions (i.e. those in NH, OH, or SH functionalities). All deuteration products were used directly, with the exception of 2-aminopyridine. To obtain a quality sample of 2-aminopyridine, the deuterated product was dissolved in ether and the ether was allowed to slowly evaporate under nitrogen. The product, 2,4,6-trimethlybenzamide, was characterized by $^1H$ solution NMR (see Appendix A). The co-crystallization product of triphenylsilylacetylene and triphenylphosphine oxide was characterized using $^{31}P$ NMR (see Appendix A)

## 1.1.   Preparation of 2,4,6-trimethylbenzamide

Ammonia gas was bubbled through a stirring solution of 2,4,6-trimethylbenzoyl chloride (0.9234 g, 5.055 mmol) in $CH_2Cl_2$ (25 mL) until the solution was found to be basic (~ 15 minutes). The reaction mixture was shaken vigorously with distilled water and the organic later was separated and dried with $MgSO_4$. The solvent was removed using rotary evaporation. Recrystallization from hexane gave 2,4,6-trimethylbenzamide in good yield (0.6942 g, 84%, m.p. 182-184).

## 1.2. Co-crystallization of triphenylsilylacetylene and triphenylphosphine oxide

In order to study the TPSiA-TPPO complex, it was first necessary to deuterate the triphenylsilylaceylene. A 2 M solution of t-BuLi in cyclohexane was slowly added to a solution of ether (8mL) and $Ph_3SiC\equiv CH$ (1.0214g, 3.590 mmol) while stirring at $0^{\circ}C$ under an argon atmosphere. After the reaction mixture reached room temperature, $D_2O$ (2mL) was slowly added dropwise. Precipitate formed in the reaction vessel and HCl was added to redissolve it. The reaction mixture was separated and the product was isolated from the organic layer via rotary evaporation. Recrystallization from hot methanol resulted in pale yellow crystals (0.2432 g, 24% yield).

To prepare the complex, equal molar quantities of TPSiA-d and TPPO were dissolved in methanol. Slow evaporation resulted in large plate-like crystals, off-white in colour.

## 2. NMR Experiments

All $^2H$ solid state spectra were obtained on a Bruker Avance-500 spectrometer ($B_o$=11.74 Tesla) , utilizing a 4 mm MAS probe tuned to the resonance frequency for $^2H$ of 76.76 MHz.

In order to reference the chemical shift values, a rotor containing a drop of $CDCl_3$ was used and set to 7.24 ppm with respect to TMS. Since $CDCl_3$ is a liquid, using it as a solid state reference is not ideal. In order to increase the efficiency of future experiments, a solid reference with a high signal-to-noise ratio (to determine $90^{\circ}$ pulse lengths) is required. The SR value from the $CDCl_3$ sample (SR = -487.47 Hz) was used to determine

the chemical shift of $(CD_3)_2SO_2$ (a more suitable reference) with respect to TMS. This process allowed $(CD_3)_2SO_2$, which has a chemical shift of 2.77 ppm with respect to TMS, to be used as an external reference for all of the compounds studied.

$^2H$ NMR experiments were set up with the standard, dimethyl sulfone $(CD_3)_2SO_2$, using a 90° pulse of ~3.3 μs. In most cases high power proton decoupling was employed to reduce spectral line width and increase resolution between multiple deuterium sites in a single spectrum. Line broadening factors of -20 Hz and – 40 Hz were applied to 2-aminopyridine and catechol, respectively, in order to resolve the two deuterium sites present in each spectrum.

## 3.    Simulations

Spectra were simulated using Simpson [98], a general simulation program designed to work as a 'virtual spectrometer'. Simpson input files containing parameters defining the spin system, external manipulation conditions and the pulse sequence were created. These input files generated spectra which were then compared to those obtained experimentally. NMR parameters (i.e. $\chi$, $\eta_Q$, $\delta_{iso}$, and $\Delta\delta$) were extracted from the input file which afforded the 'best fit'. An example of a Simpson input file is found in Appendix B.

## 4.    Quantum Chemical Calculations

All calculations were performed using the Gaussian-03 [97] package on a Pentium III 450 MHz PC.

Dunning's correlation consistent (cc) basis sets [99, 100] were used to calculate efgs for a set of thirteen molecules (for which the experimental QCCs were known). These calculations were performed to determine if the addition of diffuse functions and polarization functions improved the accuracy of the calculated efgs. Dunning's basis sets are specifically designed for high quality calculations using correlation methods. There are four basis sets:

**cc-pVDZ** of valence double zeta quality

**cc-pVTZ** of valence triple zeta quality

**cc-pVQZ** of valence quadruple zeta quality

**cc-pV5Z** of valence quintuple zeta quality

Each of these basis sets includes polarization functions by definition. The cc-pVDZ basis set adds 2s and 1p functions to H and He; 3s, 2p and 1d functions to B – Ne; and 4s, 3p and 1d functions to Al-Ar. The basis sets can be augmented to include diffuse functions of each type: s, p, f, and g, h.

The chemical shift and quadrupolar parameters for the 11 compounds investigated in this work were calculated using the Becke three-parameter hybrid exchange [101-103] and the Lee, Yang, and Parr non-local correlational functionals (B3LYP) [104].

For NMR calculations, 6-31G was the basis set of choice. In this basis set, 6 gaussian-type functions were used to describe the core electrons, and two sets of gaussian-type functions were used to describe the valence electrons (one with three gaussians, the other with one gaussian). To account for the notorious gauge-origin problem, London's gauge invariant atomic orbitals (GIAO) method [105] was employed for all calculations of chemical shielding.

To calculate the quadrupolar parameters the 6-311++G** basis set was employed. This basis set differs from the 6-31G, as the 6-311++G** uses *three* sets of gaussian functions to describe the valence electrons. In addition polarization functions (denoted by **) of the p-type (on hydrogen) and d-type (on heavier atoms) are added to accommodate an asymmetric charge distribution at the nucleus. Diffuse functions are also added (denoted by ++). These shallow Gaussian basis functions allow for the 'tail' portion of the atomic orbitals to be more accurately represented.

When neutron structures were available, they were used as the geometry with which the chemical shielding and quadrupolar parameters were calculated. When only X-ray structures were available, the positions of the hydrogen atoms directly involved in the hydrogen bonds were optimized using the B3LYP method and the 6-311++G** basis set. The resulting structures were then used to calculate $\chi$, $\eta$, $\delta_{iso}$ and $\Delta\delta$.

# CHAPTER III

## *RESULTS AND DISCUSSION*

# 1.     Calculation of Deuterium Quadrupole Parameters

Calculation of the molecular electric field gradient allows for theoretical prediction of the $^2$H quadrupolar coupling constant, the QCC being proportional to the efg. For accurate calculation of the efg, the need to include electron correlation in conjunction with a fairly large basis set is generally acknowledged [81]. Gerber and Huber [83] performed deuterium efg calculations at the level of fourth-order Møller-Plesset perturbation theory (MP4). In order to extend to fairly large molecules the possibility of calculation at this high level of correlation, these authors employed a large basis set of high quality only on the deuterium atom, with medium sized bases on neighbouring atoms and still smaller bases on atoms further removed. The MP4 calculations (with basis sets of local high quality) yielded efgs for medium sized molecules with 'experimental' accuracy. However, computer demands severely limited the application of this method to medium sized molecules or small clusters.

Calculations were performed using augmented versions of Dunning's correlation consistent (cc) basis sets, to determine if a lower level of correlation could be used to accurately determine efgs. In order to assess the accuracy of these calculations, the results were compared to QCC tensor components measured from the radiofrequency spectra. Experimentally, the coupling constants measurable from the radiofrequency spectra are the diagonal elements $\chi_{aa}$, $\chi_{bb}$, and $\chi_{cc}$, where $a$, $b$, and $c$ are the principal axes of the inertia tensor of the molecule. For direct comparison with the experimental data, the components of the efgs calculated in this work were transformed to the $a$, $b$, $c$ system of coordinates.

The molecules and experimental QCCs [106-118] listed in Table 1.1 were those used to assess the quality of the basis sets. Calculations of the efgs were performed on the equilibrium structures [119-128] using three levels of theory: Hartree-Fock (HF) theory, second-order Møller-Plesset perturbation (MP2) theory and density functional theory (DFT).

The QCCs calculated with the three levels of theory and four basis sets, along with the experimental values, are shown in Table 1.1. Overall the values obtained with B3LYP are closer to the experimental values than those obtained with HF and MP2. With all of the methods, increasing the number of polarization and diffuse functions (i.e. in going from aug-cc-pVDZ to aug-cc-pVTZ) significantly improves the QCC values.

The most accurate QCCs were obtained using the B3LYP method and the aug-cc-pV5Z basis set. In this case, the root mean square (rms) difference between the calculated and experimental QCCs is 16.3 kHz, which is 11.4% of the average absolute experimental QCC. This result is poorer than that of Gerber and Huber [83], who claim for their MP4 calculations an accuracy better than 3% in general.

The poor agreement between calculated and experimental values seen with Dunning's basis sets prompted a change in direction. A study conducted by Bailey [81] demonstrated that accurate QCC values could be calculated using the B3LYP method with a double-split valence basis set (6-31G). Polarization functions, specifically (df,3p) enhanced the accuracy of the B3LYP/6-31G calculations. Using these findings, calculations were performed to determine if the B3LYP method with the 6-311++G (d,p) basis set could accurately calculate $^2$H QCCs.

The results of the B3LYP/6-311++G (d,p) calculations are shown in Table 1.2, along with the values calculated by Bailey and the experimental values. The QCCs calculated with the 6-311++G (d,p) basis set differ significantly from the experimental values. The rms between the calculated and experimental QCCs is 77.5 kHz, which is over 50% of the average absolute experimental QCC. The basis set employed by Bailey faired much better with an rms of 8.0 kHz, which is only 5.6% of the average absolute experimental QCC. Despite the success of the 6-31G (df,3p) basis set in calculating $^2$H QCCs it was not used any further in this work. In cases of large molecules (i.e. the TPSiA-TPPO complex) and large clusters (i.e. the hexamer used for catechol) the 6-31G (df,3p) basis set was simply too computationally demanding.

To assess the use of the slightly *smaller* 6-311++G** basis set, a plot of calculated QCCs versus experimental QCCs was constructed (Figure 1.1). Linear regression analysis showed that despite the large rms, the residual standard deviation and correlation coefficient were reasonable, 16.4 kHz and 0.998, respectively. In order to increase the accuracy of the results using this basis, the model was calibrated and the best fit value of eQ/h (609.4 kHz/a.u.) was obtained. After re-calculating the values of $\chi$ (for the molecules in Table 1.2) using the best fit value of eQ/h, the rms was lowered substantially, from 77.5 kHz to 22.5 kHz, providing results with a level of accuracy similar to MP2/aug-cc-pV5Z calculations.

## Table 1.1
### Deuterium nuclear quadrupole coupling constants (kHz)

| Molecule | ij | Experimental* | Calculated§ aug-cc-pV5Z | | | Calculated§ aug-cc-pV4Z | | | Calculated§ aug-cc-pVTZ | | | Calculated§ aug-cc-pVDZ | | |
|---|---|---|---|---|---|---|---|---|---|---|---|---|---|---|
| | | | HF | MP2 | B3LYP | HF | MP2 | B3LYP | HF | MP2 | B3LYP | HF | MP2 | B3LYP |
| DD | aa | 225.04 | 229.42 | 229.55 | 223.00 | 230.73 | 230.86 | 224.51 | 233.69 | 233.79 | 228.49 | 256.78 | 256.78 | 254.3 |
| CH$_3$D | aa | 193.48 | 202.47 | 202.38 | 194.46 | 202.53 | 202.44 | 194.03 | 208.10 | 208.02 | 200.69 | 228.01 | 227.97 | 218.07 |
| HCOOD | aa | -119.30 | -121.19 | -120.95 | -124.53 | -118.00 | -117.84 | -122.03 | -129.58 | -125.91 | -130.39 | -125.16 | -125.36 | -126.09 |
| | bb | 267.50 | 274.21 | 274.34 | 276.07 | 276.66 | 276.84 | 278.40 | 292.35 | 292.55 | 294.96 | 293.28 | 293.88 | 287.10 |
| | cc | -148.20 | -153.03 | -153.39 | -151.54 | -158.66 | -159.00 | -156.37 | -161.56 | -166.64 | -164.55 | -168.13 | -168.52 | -161.00 |
| DF | aa | 354.24 | 345.88 | 346.53 | 357.06 | 348.20 | 348.48 | 359.13 | 365.16 | 365.42 | 377.21 | 379.01 | 379.01 | 378.34 |
| DCl | aa | 188.80 | 189.35 | 189.25 | 187.42 | 190.15 | 190.06 | 186.61 | 197.09 | 197.03 | 194.56 | 213.79 | 213.76 | 209.14 |
| DBr | aa | 146.90 | 151.93 | N/A | 148.04 | 151.86 | N/A | 147.70 | 154.64 | N/A | 152.45 | 170.65 | N/A | 165.67 |
| D$_2$S | aa | 51.84 | 54.52 | 54.47 | 52.73 | 54.66 | 54.65 | 52.55 | 56.17 | 56.18 | 53.89 | 60.38 | 60.34 | 57.93 |
| | bb | 36.54 | 37.34 | 37.31 | 36.50 | 37.54 | 37.41 | 36.34 | 38.66 | 38.55 | 38.24 | 43.09 | 43.11 | 41.82 |
| | cc | -88.38 | -91.87 | -91.78 | -89.23 | -92.21 | -92.06 | -88.90 | -94.08 | -94.72 | -92.14 | -103.47 | -103.45 | -99.74 |
| DCN | aa | 200.65 | 213.41 | 213.35 | 209.63 | 213.58 | 213.53 | 209.30 | 218.18 | 218.13 | 214.73 | 243.84 | 243.87 | 238.92 |
| D$_2$CO | aa | -12.53 | -13.32 | -13.17 | -12.49 | -13.39 | -13.24 | -12.57 | -13.84 | -13.69 | -12.92 | -16.13 | -16.12 | -15.83 |
| | bb | 97.23 | 101.10 | 101.11 | 98.61 | 101.21 | 101.22 | 98.49 | 104.42 | 104.43 | 102.03 | 115.45 | 115.53 | 111.54 |
| | cc | -84.70 | -87.78 | -87.93 | -86.12 | -87.82 | -87.98 | -85.92 | -90.58 | -90.74 | -89.11 | -99.32 | -99.41 | -95.71 |
| CF$_3$D | aa | 170.80 | 171.04 | 171.71 | 169.28 | 171.22 | 171.91 | 169.08 | 177.89 | 177.89 | 175.68 | 197.96 | 198.03 | 191.98 |
| HD | aa | 224.55 | 229.47 | 229.59 | 223.04 | 230.78 | 230.90 | 224.55 | 233.73 | 233.84 | 228.54 | 256.83 | 256.83 | 254.35 |
| BD$_3$CO | aa | -48.50 | -56.26 | -56.18 | -55.11 | -56.21 | -56.12 | -54.54 | -57.38 | -57.19 | -56.20 | -64.11 | -64.11 | -62.99 |
| CD$_3$CN | aa | -55.10 | -58.24 | -58.14 | -56.81 | -58.27 | -58.17 | -56.70 | -59.90 | -59.80 | -58.63 | -65.81 | -65.82 | -64.17 |
| RMS | | | 23.87 | 23.16 | 16.29 | 26.42 | 26.06 | 18.54 | 46.10 | 46.74 | 46.62 | 100.02 | 97.45 | 83.82 |

* Experimental data obtained from [106-118].
§ Calculated using equilibrium geometries from [119-128].

78

## Table 1.2
### Deuterium nuclear quadrupole coupling constants (kHz)

| Molecule | ij | Experimental* | Calculated§ B3LYP 6-311++G(d,p) | Calculated† B3LYP 6-31G(df,3p) |
|----------|-----|---------------|-------------------------------|-------------------------------|
| DD | aa | 225.04 | 237.78 | 223.9 |
| $CH_3D$ | aa | 193.48 | 215.96 | 193.1 |
| HCOOD | aa | -119.30 | -132.80 | -118.9 |
| | bb | 267.50 | 296.07 | 267.1 |
| | cc | -148.20 | -162.57 | -148.2 |
| DF | aa | 354.24 | 383.60 | 354.7 |
| DCl | aa | 188.80 | 209.85 | 186.5 |
| DBr | aa | 146.90 | 171.52 | 145.7 |
| $D_2S$ | aa | 51.84 | 58.58 | 52.68 |
| | bb | 36.54 | 41.03 | 36.56 |
| | cc | -88.38 | -99.61 | -89.24 |
| DCN | aa | 200.65 | 234.47 | 204.5 |
| $D_2CO$ | aa | -12.53 | -15.27 | -13.84 |
| | bb | 97.23 | 110.55 | 96.9 |
| | cc | -84.70 | -95.28 | -83.06 |
| $CF_3D$ | aa | 170.80 | 189.09 | 167.4 |
| HD | aa | 224.55 | 237.82 | 224.0 |
| $BD_3CO$ | aa | -48.50 | -60.18 | -44.7 |
| $CD_3CN$ | aa | -55.10 | -62.93 | -56.05 |
| **RMS** | | | **77.54** | **7.97** |

\* Experimental data obtained from [106-118].
† Calculations by Bailey [81].
§ Calculated using equilibrium geometries from [119-128].
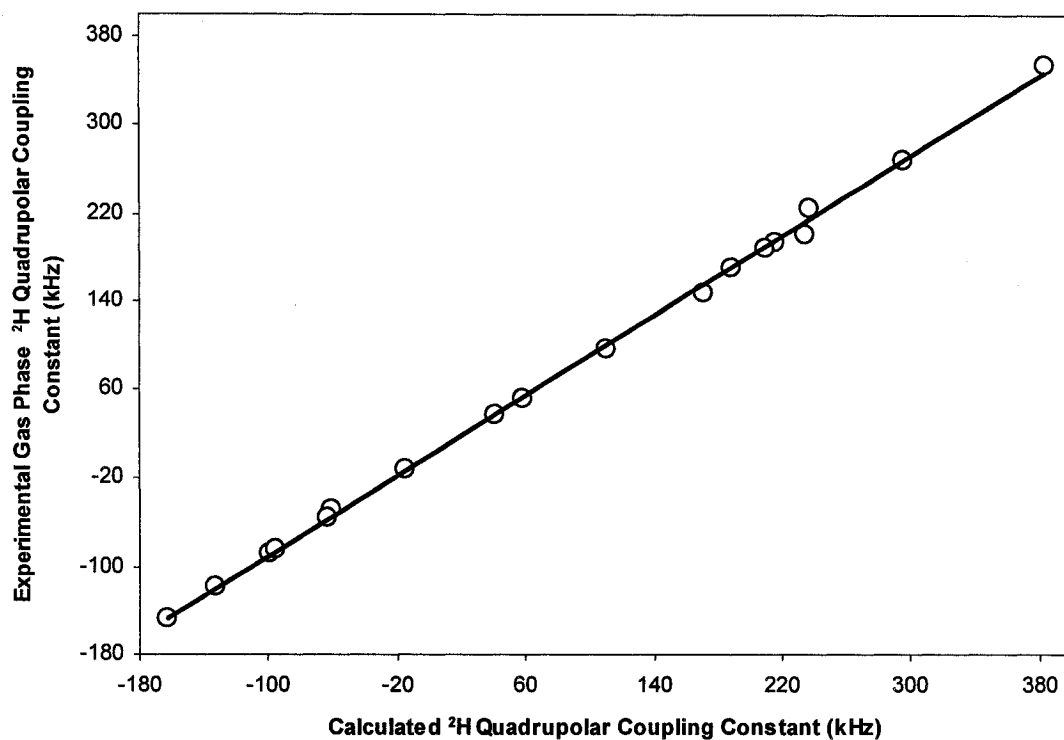
**Figure 1.1** B3LYP/6-311++G(d,p) quadrupolar coupling constants compared to those obtained experimentally from radiofrequency spectra.

## 2. Calculation of Deuterium Chemical Shifts

Ab initio calculations allow the prediction of chemical shielding parameters in an absolute sense, i.e. with respect to a bare nucleus. However, NMR experiments provide chemical shift information with regard to some standard references. In order to correlate the theoretical ab initio values (shielding) and the experimental results (shift), it is necessary to convert the calculated values. Generally, this conversion is performed by taking the difference between the calculated shielding and that found for a reference molecule such as tetramethylsilane (TMS). However, as Chesnut [129] as well as Forsyth and Sebag [130] have pointed out, this is not the best procedure and better results can be obtained by setting up a linear regression between calculated shieldings and experimental shifts.

A small dataset (12 compounds) was taken from a compilation of experimental spectra recorded in $CDCl_3$ solution [131]. Geometries of these 12 compounds were optimized at the B3LYP level with the 6-311++G** basis set. For the shielding calculations B3LYP theory was used with three separate basis sets: 6-31G, 6-31G (d), and 6-311G. The addition of polarization functions on hydrogen has been shown to have no impact on $^1H$ chemical shift accuracy and thus, polarization functions were limited to heavier atoms. Larger basis sets were not investigated, as high computational demand limited their applicability in later study.

The experimental and calculated chemical shifts are shown in Table 2.1. These results were derived from simple linear regression equations of the form:

$$\delta = \delta^0 + \kappa \cdot \sigma \qquad (2.1)$$

## Table 2.1

**Experimental ¹H NMR chemical shifts, calculated magnetic shieldings and chemical shifts**

| | Chemical Shift* | B3LYP/6-31G | | | B3LYP/6-311G | | | B3LYP/6-31G(d) | | |
|---|---|---|---|---|---|---|---|---|---|---|
| | | σ (ppm) | δ (ppm) Predicted | Error | σ (ppm) | δ (ppm) Predicted | Error | σ (ppm) | δ (ppm) Predicted | Error |
| Acetone | 2.09 | 30.52 | 2.39 | 0.30 | 29.91 | 2.94 | 0.85 | 30.34 | 1.92 | -0.17 |
| Acetonitrile | 1.98 | 31.00 | 1.91 | -0.07 | 31.04 | 1.81 | -0.17 | 30.68 | 1.58 | -0.40 |
| Acetylene | 1.8 | 31.55 | 1.36 | -0.44 | 31.34 | 1.51 | -0.29 | 31.12 | 1.14 | -0.66 |
| Benzene | 7.26 | 25.55 | 7.36 | 0.10 | 25.55 | 7.30 | 0.04 | 25.02 | 7.24 | -0.02 |
| Ethane | 0.86 | 31.84 | 1.07 | 0.21 | 31.80 | 1.05 | 0.19 | 31.28 | 0.98 | 0.12 |
| Ethylene | 5.28 | 27.01 | 5.9 | 0.62 | 27.07 | 5.78 | 0.50 | 26.77 | 5.49 | 0.21 |
| Fluromethane | 4.27 | 28.48 | 4.43 | 0.16 | 28.44 | 4.41 | 0.14 | 27.96 | 4.3 | 0.03 |
| Formamide | 7.97 | 24.33 | 8.58 | 0.61 | 24.25 | 8.60 | 0.63 | 24.20 | 8.06 | 0.09 |
| Methane | 0.23 | 32.46 | 0.45 | 0.22 | 32.48 | 0.37 | 0.14 | 31.98 | 0.28 | 0.05 |
| Nitromethane | 4.28 | 28.43 | 4.48 | 0.20 | 28.43 | 4.42 | 0.14 | 28.34 | 3.92 | -0.36 |
| Silane | 3.23 | 29.65 | 3.26 | 0.03 | 29.59 | 3.26 | 0.03 | 28.58 | 3.68 | 0.45 |
| TMS | 0 | 32.91 | 0 | 0.00 | 32.85 | 0.00 | 0.00 | 32.26 | 0 | 0.00 |

* Experimental data obtained from [131].

82

where $\delta$ is the calculated chemical shift on the $\delta$-scale relative to TMS, $\sigma$ is the calculated

shielding and $\kappa$ and $\delta^0$ are the slope and intercept, respectively. The three basis sets

employed give the regression equations, and standard deviations shown in Table 2.2.

**Table 2.2**
**Regression equations and errors obtained from plots of**
**chemical shielding versus chemical shift (relative to TMS)**

| Level | $\kappa$ | $\delta^0$ | $R^2$ | Standard deviation |
|---|---|---|---|---|
| B3LYP/6-31G | -0.9408 | 31.00 | 0.9919 | 0.29 |
| B3LYP/6-31G(d) | -0.9666 | 31.35 | 0.9880 | 0.30 |
| B3LYP/6-311G | -0.9474 | 31.12 | 0.9874 | 0.33 |

Figure 2.1 shows a plot of the experimental versus calculated values for the B3LYP/6-

31G level of theory. The linear regression equation for B3LYP/6-31G shows the highest

correlation coefficient (0.992) and the smallest standard deviation (0.29 ppm). It can be

concluded that B3LYP/6-31G is an adequate level for calculating chemical shifts for $^1$H

economically and reliably, thus it was used for all NMR calculations in this work.
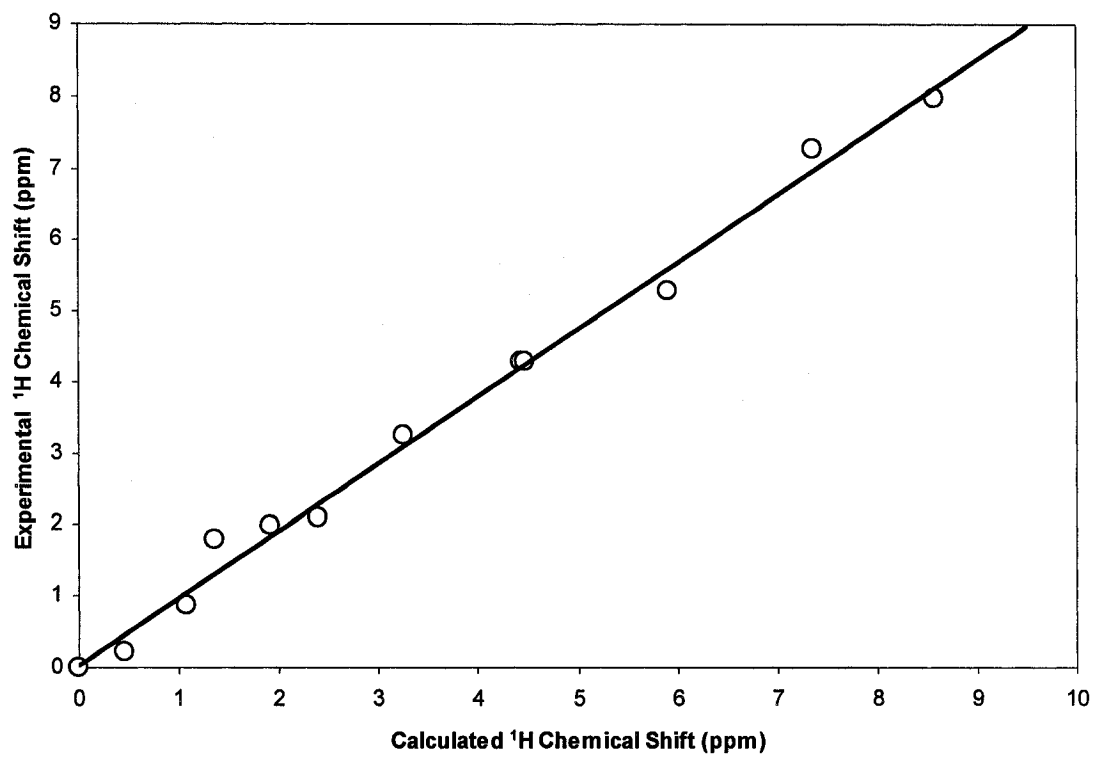
Figure 2.1    Experimental and calculated $^1$H shifts obtained using the fitted regression equation from Table 2.2 at B3LYP/6-31G.

# 3.    Investigation of a C–H Hydrogen Bond

The investigation of a hydrogen bond interaction with NMR spectroscopy requires that the interaction be strong enough to affect the quadrupolar and chemical shift parameters. C–H···O hydrogen bonds in general are much weaker interactions than conventional O/N–H···O/N hydrogen bonds, and have much longer donor-acceptor separations. As a result of this inherent weakness, C–H···O interactions have never been studied by solid state NMR spectroscopy.

The shortest C–H···O bonds known today have H···O and C···O separations of around 2.0 Å and 3.0 Å respectively and are formed by highly activated H atoms. Particularly short C–H···O bonds are formed if a strong donor is combined with a strong acceptor like P=O. A deliberately designed example is the complex of triphenylsilylacetylene-triphenylphosphine oxide (TPSiA-TPPO) [132] seen in Figure 3.1.

The crystal structure of the TPSiA-TPPO complex contains four symmetry-independent quasi-centrosymmetric C–H···O hydrogen bonded dimers. All dimers have somewhat different geometries as seen in Table 3.1. The combination of the acidic acetylene donor with the basic P=O acceptor results in unusually short C–H···O contacts: the H···O distances are between 1.99 Å and 2.05 Å, mean value 2.02 Å. This means that the complex contains the shortest C≡C–H···O bond known to date. Although the H···O distances in the complex are in a narrow range, the C–H···O angles vary over a rather wide range, 152-176°. This variability in hydrogen bond angle is a consequence of the well known flexibility of hydrogen bonds in general: they tend to be linear but can be easily distorted without much of a loss in bond energy.
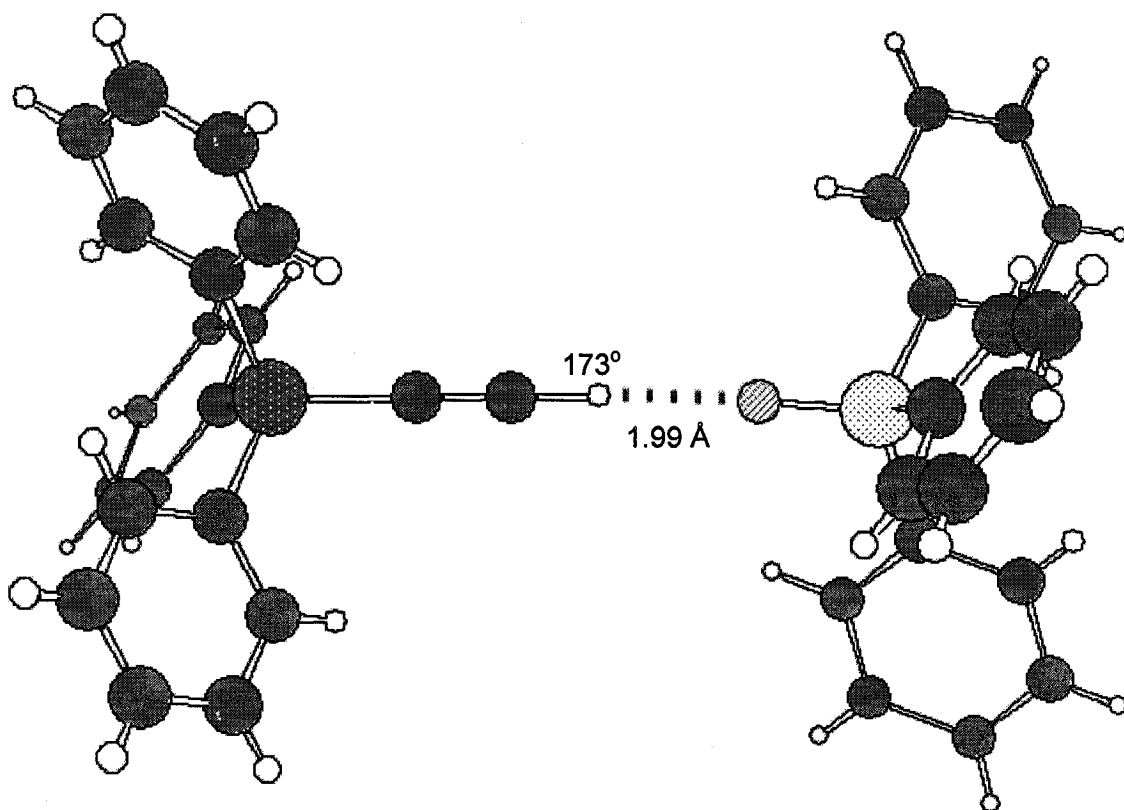
**Figure 3.1** One of the four symmetry-independent dimers of triphenylsilyacetylene-triphenylphosphine oxide. Atom designations are provided in Appendix C.

**Table 3.1**
**Hydrogen bond geometry based on a linear Si–C≡C–H group**
**with C–H=1.08 Å**

| Dimer | H···O (Å) | C···O (Å) | C–H···O (°) | H···O=P (°) |
|-------|-----------|-----------|-------------|-------------|
| A | 2.01 | 3.02 | 155 | 145 |
| B | 2.05 | 3.04 | 152 | 143 |
| C | 2.02 | 3.09 | 173 | 176 |
| D | 1.99 | 3.06 | 173 | 173 |

The strength of the TPSiA-TPPO hydrogen bond made it suitable for study by means of NMR spectroscopy. Before NMR experiments were undertaken, quantum chemical calculations were performed on each of the four dimers in the X-ray structure; calculated values of $\chi$, $\eta_Q$ and $\delta$ are given in Table 3.2. Despite the range of H···O bond distances and the range of C–H···O bond angles, the values obtained for $\chi$, $\eta_Q$ and $\delta$ are very similar. Thus, for further comparison with experimentally determined values, the computational results were averaged.

**Table 3.2**
**Calculated parameters for the four**
**symmetry-independent TPSiA-TPPO dimers**

| Dimer | $\chi$ (kHz) | $\eta$ | $\delta$ (ppm) |
|-------|--------------|--------|----------------|
| A | 170 | 0.00 | 5.8 |
| B | 174 | 0.00 | 5.6 |
| C | 172 | 0.00 | 5.6 |
| D | 172 | 0.00 | 5.6 |

$^2$H NMR experiments were performed using MAS (10 kHz sample spinning). Two spectra were obtained, one for the deuterated TPSiA (Figure 3.2) and one for the co-crystals of TPSiA-d and TPPO (Figure 3.3). Both the TPSiA-d and the complex-d spectra were simulated using the Simpson simulation package, and the results can be seen in

Figures 3.2 and 3.3, respectively. From the simulations, values of $\chi$, $\eta_Q$ and $\delta$ were extracted. These experimental values are given in Table 3.3.

Calculations were performed on the X-ray structure of TPSiA [133] to obtain values of $\chi$, $\eta_Q$ and $\delta$ prior to co-crystal formation. The results of these calculations along with the averages for the TPSiA-TPPO calculations are given in Table 3.3.

During the simulation process, it was noted that distinct asymmetries were present in the spinning sideband manifolds. These asymmetries indicate that the spectra are not only influenced by the $^2H$ quadrupolar parameters, but also by chemical shift anisotropy $\Delta\delta$. The chemical shift anisotropy was determined for both TPSiA and the TPSiA-TPPO complex using simulations, the results of these simulations are seen in Figure 3.2 and Figure 3.3, respectively. Simulating the TPSiA and TPSiA-TPPO spectra in order to determine $\Delta\delta$ values proved to be very difficult, as evidenced by the large errors associated with both values (see Table 3.3). In order to obtain more accurate values of $\Delta\sigma$, experimental spectra would have to be obtained at a higher field (i.e. 800 or 900 MHz), where the effects of $\Delta\delta$ are magnified.

**(a)**

**(b)**

**(c)**

| 200000 | 100000 | 0 | -100000 | -200000 |

kHz
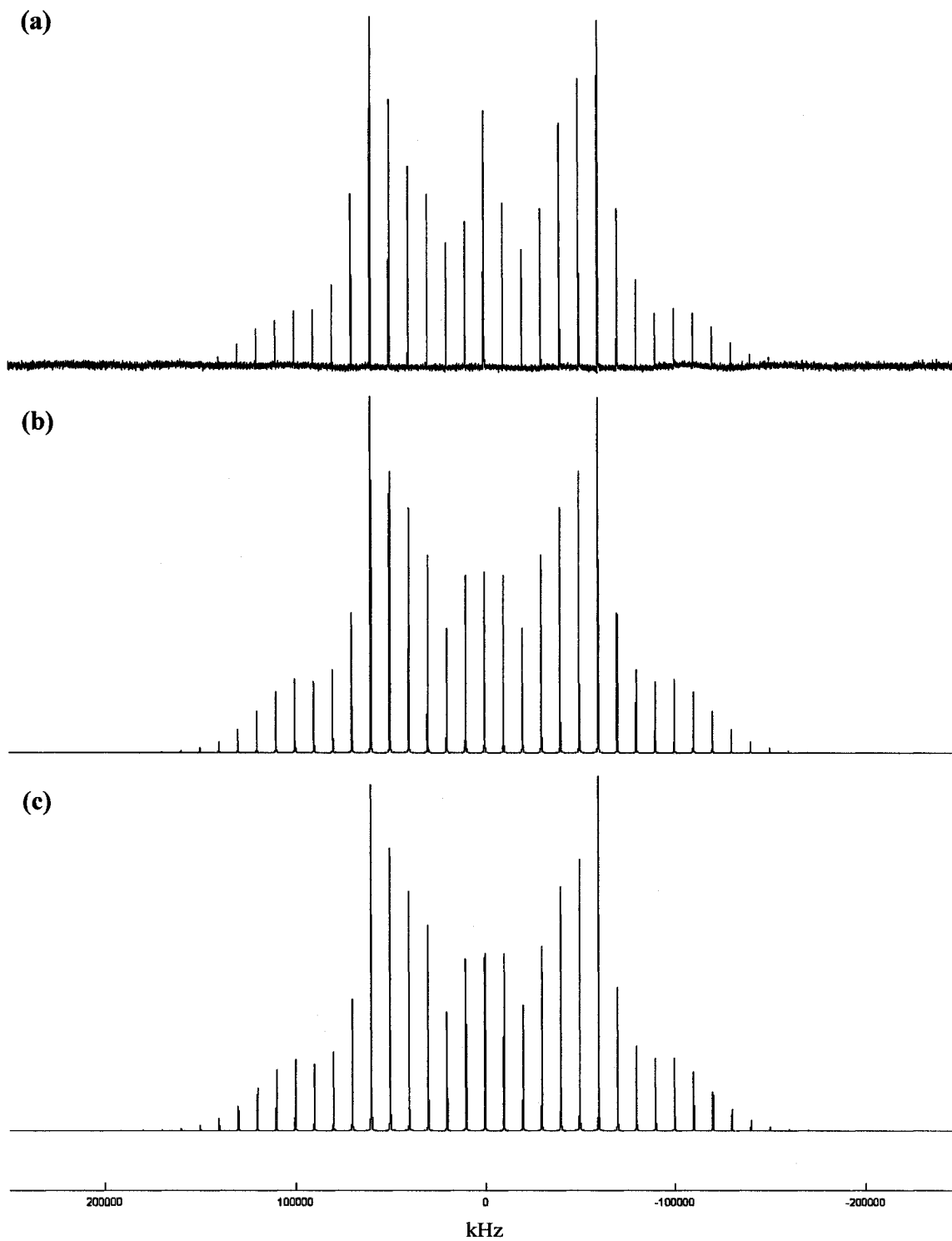
Figure 3.2     $^2$H MAS spectrum of TPSiA-d: (a) Experimental (b) Simulation (c) Simulation with $\Delta\delta$ = 15ppm.

**(a)**

**(b)**

**(c)**

| 200000 | 100000 | 0 | -100000 | -200000 |

**kHz**
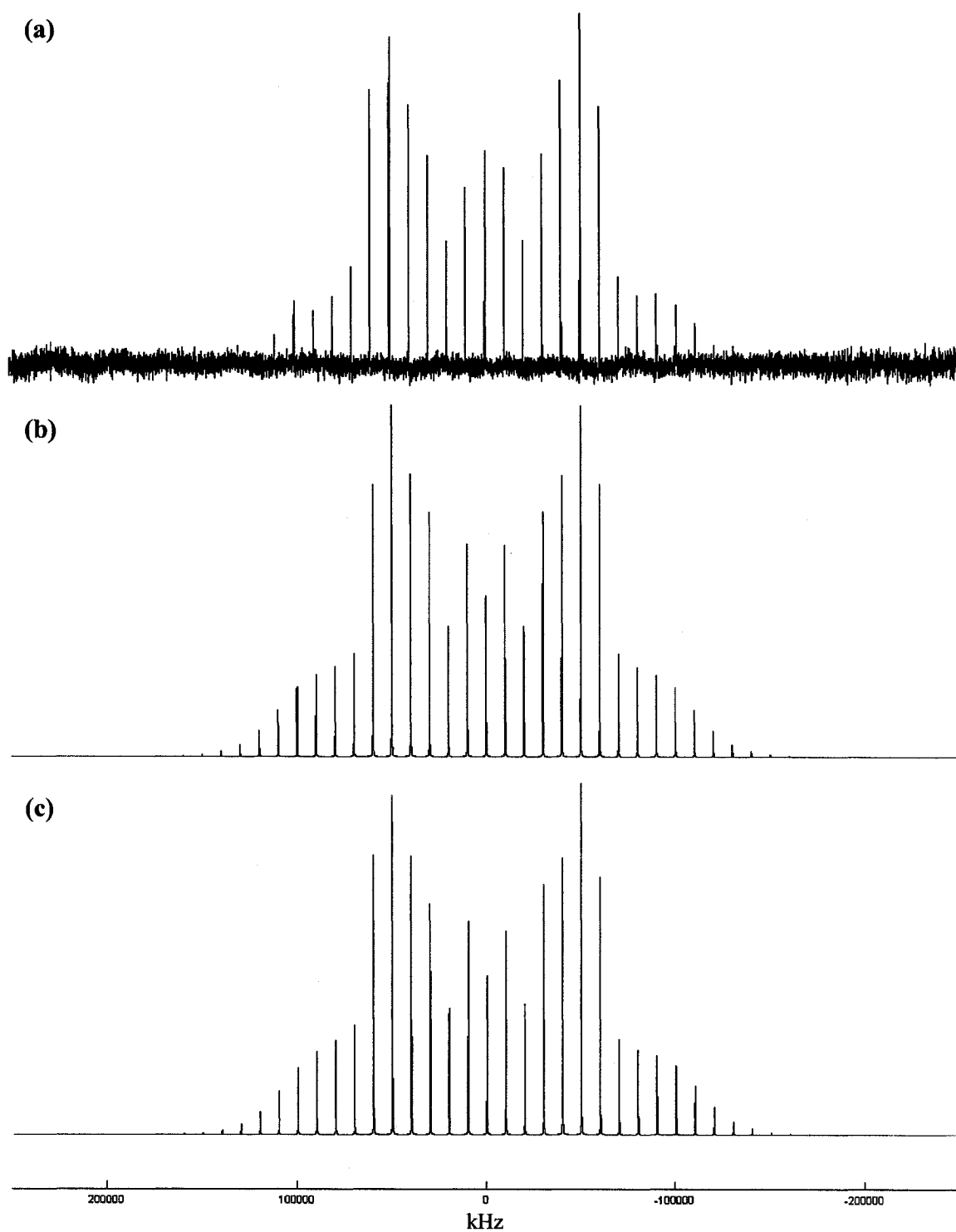
Figure 3.3      $^2$H MAS spectrum of the complex of TPSiA-d and TPPO: (a) Experimental
(b) Simulation (c) Simulation with $\Delta\delta$ = 20ppm.

90

**Table 3.3**
**Quadrupolar and chemical shift parameters for TPSiA-d and TPSiA-d–TPPO**

| | $\chi$ (kHz) | | $\eta_Q$ | | $\delta$ (ppm) | | $\Delta\delta$ (ppm) | |
|---|---|---|---|---|---|---|---|---|
| | Expt. | Calc. | Expt. | Calc. | Expt. | Calc. | Expt. | Calc. |
| **TPSiA** | 180±2 | 199 | 0.05±0.05 | 0.00 | 2.9 | 3.1 | 15±15 | 14 |
| **TPSiA-TPPO** | 167±3 | 172 | 0.05±0.05 | 0.00 | 5.6 | 5.7 | 25±5 | 27 |
| **Difference** | 13±4 | 27 | 0.00 | 0.00 | -2.7 | -2.6 | -10±16 | -13 |

The calculated quadrupolar (B3LYP 6-311++G**) and chemical shift (B3LYP 6-31G) parameters compare favourably with the experimental values, with one notable exception. The calculated value of $\chi$ for TPSiA-d is much larger than that determined experimentally. The overestimated value of $\chi$ results from fact that the TPSiA was calculated using a monomer, rather than a cluster. Using a TPSiA cluster in the calculation of $\chi$ should result in a more accurate value; however such calculations were not attempted due to the high computational demand.

The quadrupolar and chemical shift parameters strongly indicate the presence of a C–H···O hydrogen bond in the TPSiA-TPPO complex. TPSiA has a larger value of $\chi$ (180 kHz) than the complex of TPSiA-TPPO (167 kHz). Previous work has shown that the presence of hydrogen bonding reduces the values of $^2$H QCCs [71-80], thus the decrease of $\chi$ after formation of the complex is as expected. The value of the chemical shift increases from 2.9 ppm to 5.6 ppm in moving from TPSiA to TPSiA-TPPO; chemical shifts are strong indicators of hydrogen bonding [52, 85-88], and the shift to a higher value is consistent with previous findings. The value of the chemical shift anisotropy is higher for TPSiA-TPPO than for TPSiA. Chemical shift anisotropy has been found to be a better indicator of hydrogen bond formation than chemical shift [92];

this phenomenon is clearly seen here as $\delta_{iso}$ changes by only 2.7 ppm while $\Delta\delta$ changes by 10 ppm.

The value of the asymmetry parameter is unchanged in moving from the uncomplexed TPSiA to the TPSiA-TPPO complex. The asymmetry parameter has been shown to increase upon formation of a hydrogen bond; however, even in the presence of hydrogen bonding $\eta_Q$ values are still small, $\leq 0.3$. The unchanging value of $\eta_Q$ is attributed to the deviation from linearity (average C–H$\cdots$O angle is $163°$) of the hydrogen bond geometry.

# 4. Investigation of Amide Hydrogen Bonds

Hydrogen-bonding interactions involving amides are of interest, as the two hydrogens of the amide have the potential to hydrogen bond in different ways. When considering a monomer, i.e. in the absence of hydrogen bonding, the quadrupolar and chemical shift parameters for the two amide hydrogens are comparable. When considering a cluster, where the two amide H atoms hydrogen bond in different ways, the values of $\chi$, $\eta_Q$ and $\delta$ are distinct for each donor. By measuring $\chi$, $\eta_Q$ and $\delta$ using NMR spectroscopy the relative strengths of the two distinct hydrogen-bonding interactions can be inferred.

## 4.1. 2,4,6-Trimethylbenzamide

The crystal structure of 2,4,6-trimethylbenzamide [134] displays an infinite one-dimensional network composed of primary amide molecules connected by N–H$\cdots$O=C hydrogen bonds involving the *anti* NH amide H atoms. The network is additionally stabilized by a weak N–H$\cdots$$\pi$ interaction between the *syn*-oriented amide H atom and the aromatic ring of a neighbouring molecule. The parameters of the hydrogen bond geometry are outlined in Table 4.1. The hydrogen bonding motif is illustrated in Figure 4.1.

**Table 4.1**
**Hydrogen bonded geometry of 2,4,6-trimethylbenzamide**

| X–H$\cdots$A | X–H (Å) | H$\cdots$A (Å) | X$\cdots$A (Å) | X–H$\cdots$A (°) |
|---|---|---|---|---|
| N–H$\cdots$$\pi$ | 0.90 | 2.50 | 3.40 | 173 |
| N–H$\cdots$O | 0.90 | 1.97 | 2.87 | 177 |
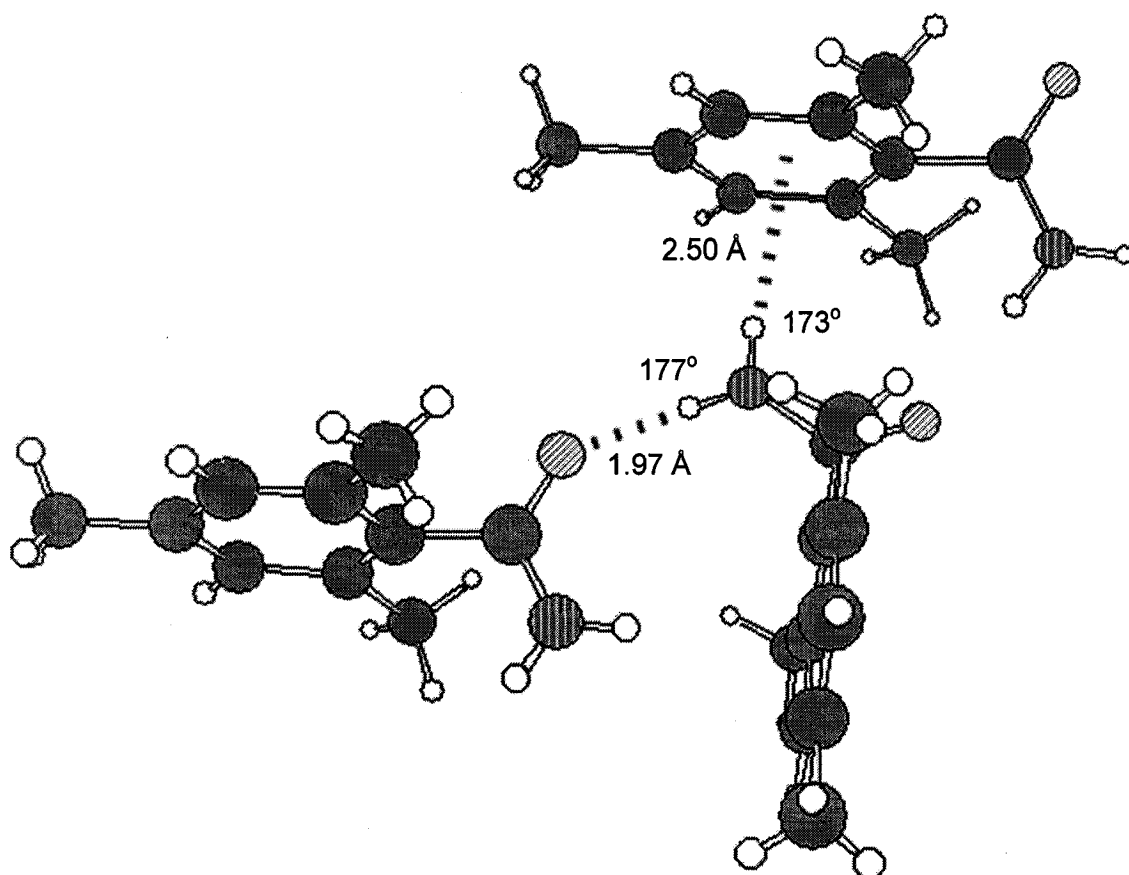
**Figure 4.1** A hydrogen-bonded chain in 2,4,6-trimethylbenzamide. Atom designations are provided in the Appendix.

A $^2$H NMR spectrum of selectively deuterated 2,4,6-trimethylbenzamide was obtained using MAS (sample spinning of 10kHz), see Figure 4.2. The effect of the differential hydrogen bonding was seen as two overlapping spinning sideband manifolds, offset by 4.9 ppm. Simulations of the two separate sites were performed using the Simpson simulation program as seen in Figure 4.2. The values of $\chi$, $\eta_Q$ and $\delta$ extracted from the simulations are tabulated in Table 4.2.

The X-ray structure of 2,4,6-trimethylbenzamide contained N–H bond lengths that were shorter than expected based on standard bond lengths. Thus, an optimization of the hydrogen positions was performed to 'normalize' these lengths. A table of the hydrogen bond geometries after the hydrogen positions were optimized is found in Appendix D. Calculations of the quadrupolar and chemical shift parameters were performed on a trimer (see Figure 4.1), and the results are given in Table 4.2.
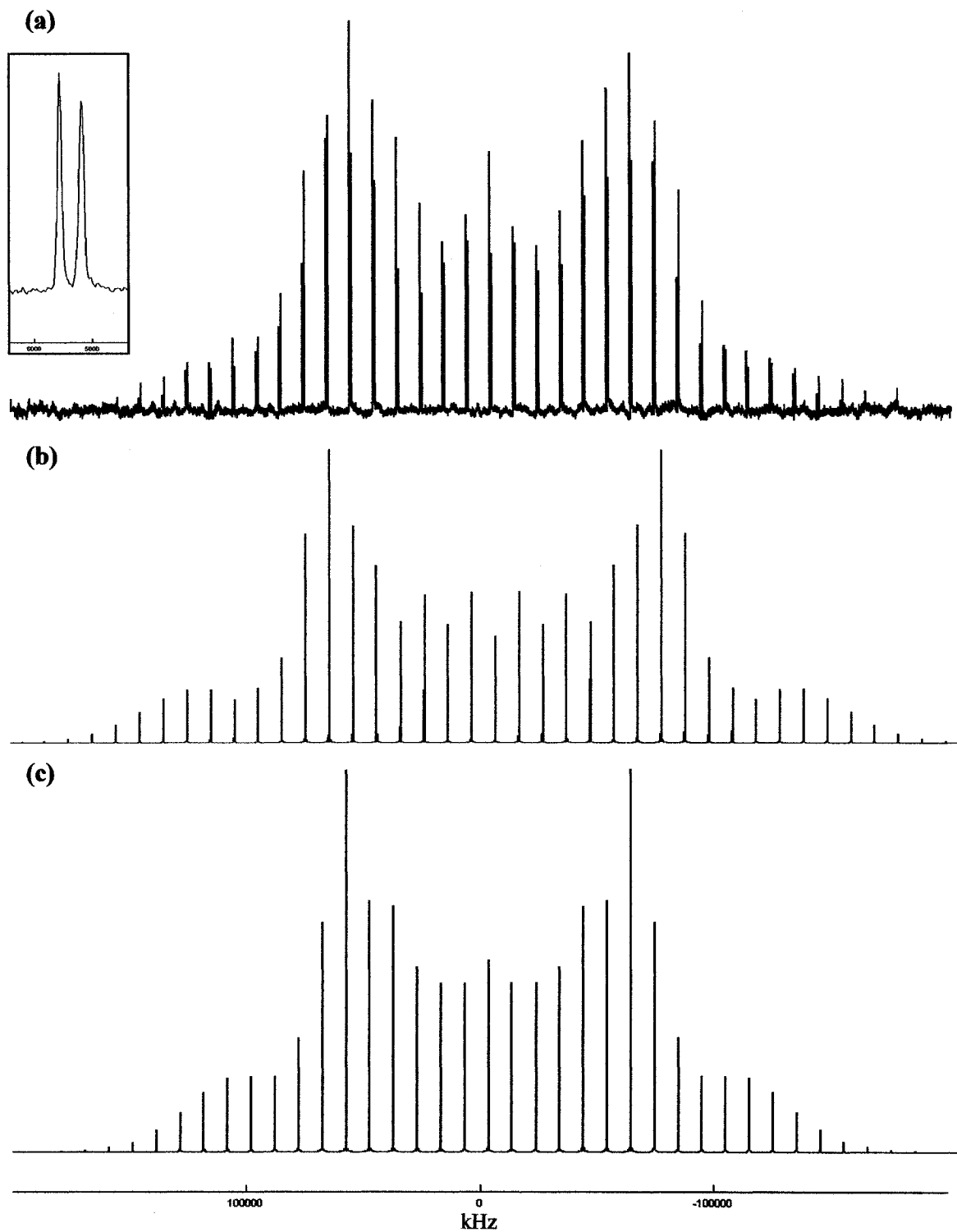
**Figure 4.2** $^{2}$H MAS spectrum of 2,4,6-trimethylbenzamide-$d_2$: (a) Experimental (the two sites have been highlighted for clarity) Inset: Fully resolved resonances seen in the experimental spectrum (b) Simulation - site 1 (c) Simulation -site 2.

## Table 4.2
### Quadrupolar and chemical shift parameters for 2,4,6-trimethylbenzamide

| Site | X–H···A | $\chi$ (kHz) Expt. | Calc. | $\eta_Q$ Expt. | Calc. | $\delta$ (ppm) Expt. | Calc. |
|------|---------|------|------|------|------|------|------|
| 1 | N–H···$\pi$ | 220±10 | 234 | 0.05±0.05 | 0.15 | 3.9 | 2.5 |
| 2 | N–H···O | 195±4 | 206 | 0.13±0.03 | 0.19 | 8.8 | 7.4 |
| **Difference** | | 25±11 | 28 | -0.08±0.06 | -0.04 | -4.9 | -4.9 |

The experimental results and calculated values are in good agreement. The value of $\chi$ is much larger for the N–H···$\pi$ than for the N–H···O bond, indicating that the N–H···O bond is the stronger of the two. The asymmetry parameter is 0.05±0.05 for the N–H···$\pi$ bond but larger, 0.013±0.03, for the N–H···O bond; again indicating that the N–H···O bond is the stronger interaction. Final confirmation is seen in the chemical shift data; the chemical shift of the more strongly hydrogen-bonded amide H is 8.8 ppm while that of the more weakly hydrogen-bonded amide H is only 3.9 ppm.

## 4.2. Benzamide

The structure of benzamide [135] consists of cyclic dimers linked laterally to form ribbons which extend throughout the crystal. The crystal structure contains two distinct N–H···O=C bonds which vary in length and N–H···O angle. The parameters of the hydrogen bond geometry are outlined in Table 4.3. The hydrogen bonding motif is illustrated in Figure 4.3

## Table 4.3
### Hydrogen bonded geometry of benzamide

| X–H···A | X–H (Å) | H···A (Å) | X···A (Å) | X–H···A (°) |
|---------|---------|-----------|-----------|-------------|
| N–H···O | 1.01 | 1.96 | 2.97 | 153 |
| N–H···O | 1.02 | 1.91 | 2.93 | 174 |
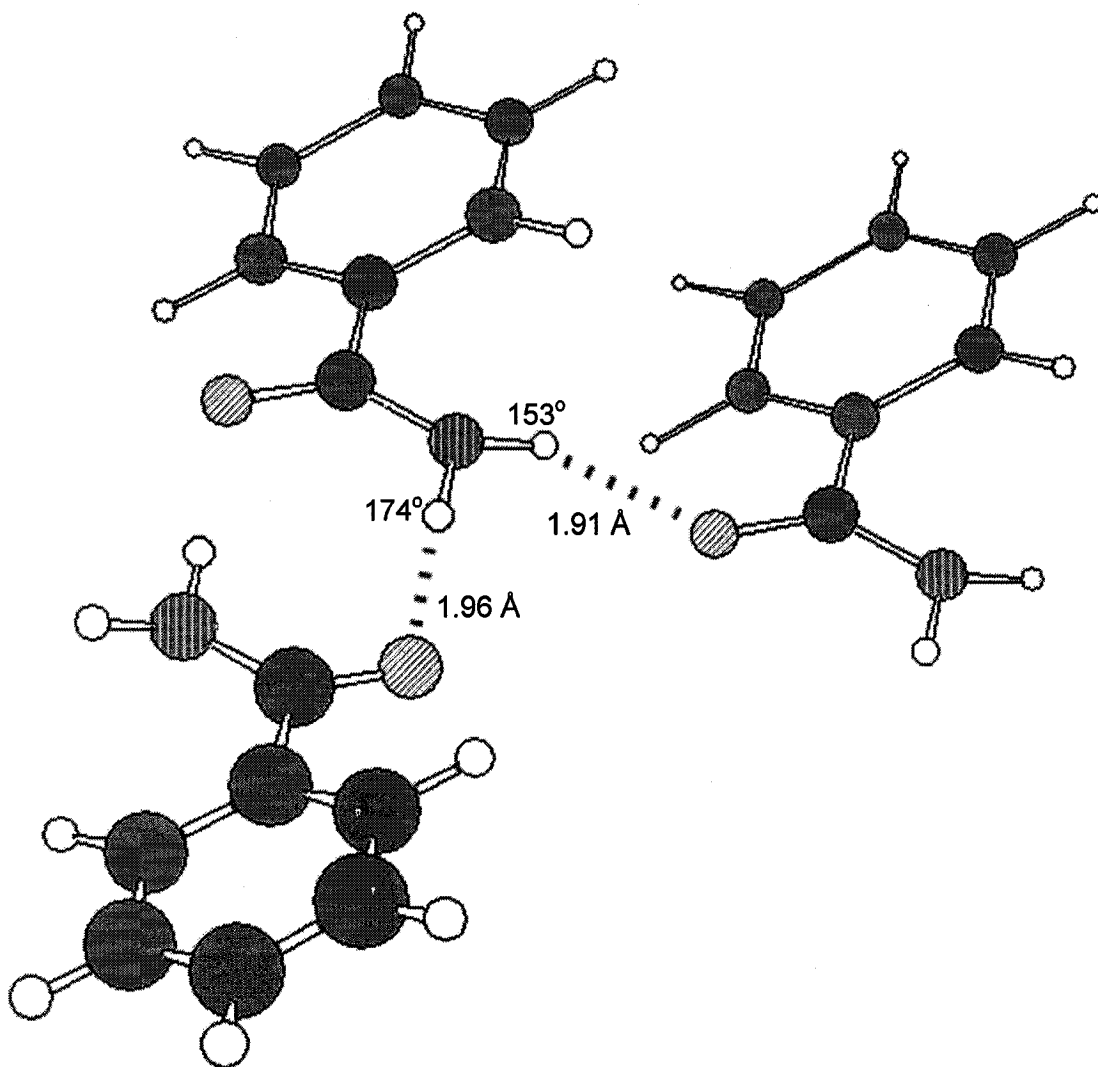
**Figure 4.3** A hydrogen-bonded chain in benzamide. Atom designations are provided in the Appendix.

A $^2$H NMR spectrum of selectively deuterated benzamide was obtained, and is shown in Figure 4.4. Based on the crystal structure of benzamide [135], it was expected that the two amide H atoms would possess different quadrupolar and chemical shift parameters, and thus be resolved. However, as seen in Figure 4.4 only a single resonance is present in the benzamide spectrum. There are two possible reasons for this result: (1) the $NH_2$ group is flipping rapidly and the spectrum represents an average of the two sites; (2) the two hydrogens are bonding in such a similar fashion that the difference in the quadrupolar coupling constants and chemical shifts cannot be resolved. In order to determine which of the two possibilities resulted in the lack of resolution, calculations were performed.

**(a)**



**(b)**



200000          100000           0          -100000          -200000
                            kHz
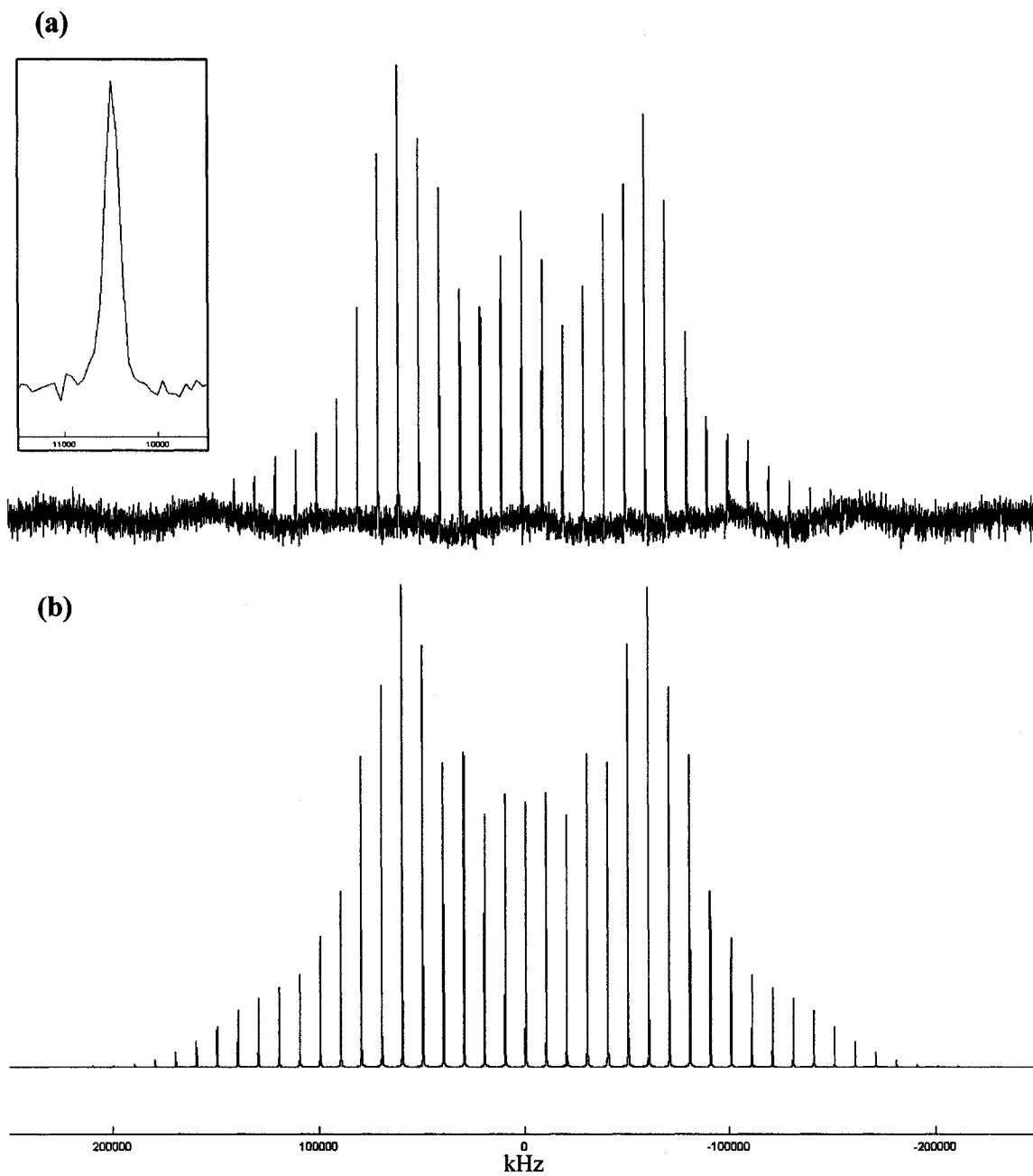
Figure 4.4     $^2$H MAS spectrum of benzamide-d$_2$: (a) Experimental Inset: Single resonance seen in the experimental spectrum (b) Simulation.

Using the program NMR Weblab [136] the effects of motional averaging can be simulated. Using a cone angle of 60° and a flip angle of 180° (both obtained using the amide geometry), and assuming a QCC of 220 kHz, a spectrum under the effects of fast motional averaging was simulated. The averaged spectrum had a very large asymmetry parameter, $\eta_Q$=0.625, which defined its overall shape as seen in Figure 4.5. The overall shape of the averaged spectrum was much different than the shape of the experimental benzamide spectrum, and thus, motional averaging was discounted.
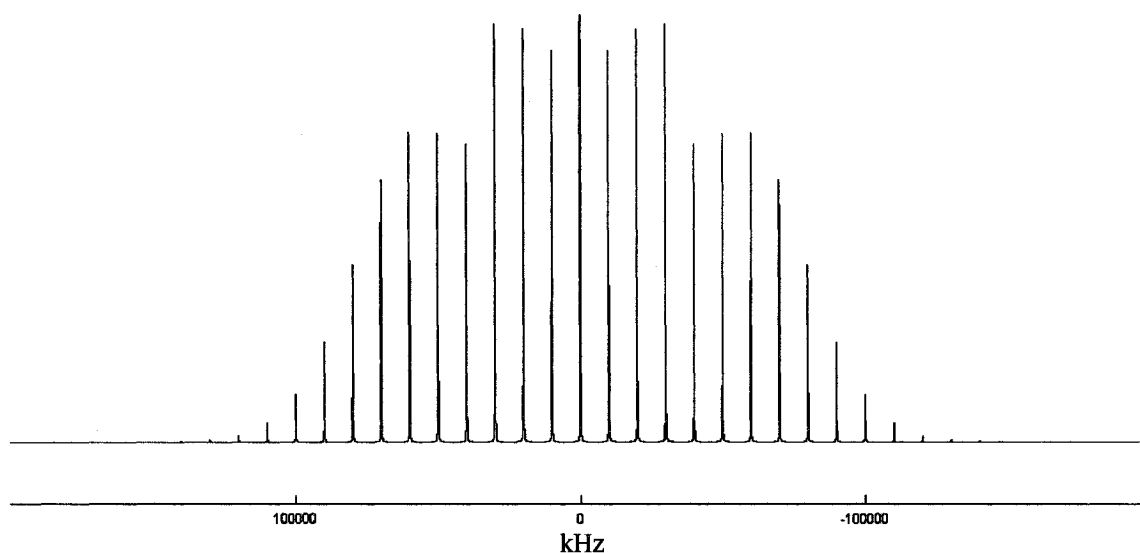


**Figure 4.5** **Simulation illustrating the effect of fast motional averaging on the spectrum of a differential hydrogen bonding amide.**

After discounting motional averaging, the second possibility was further investigated. In order to determine if the two sites were overlapping completely, calculations were performed. Using the crystal structure geometry, a benzamide tetramer was used to calculate the quadrupolar and chemical shift parameters. The results of these calculations are tabulated in Table 4.4. The calculations show that the chemical shifts of

the two sites should differ by 1.4 ppm; however fairly large line widths in the experimental spectrum (2.4 ppm) could easily mask this separation.

In order to further investigate this hypothesis, the benzamide spectrum was simulated using two sites with the same chemical shift but different quadrupolar parameters. The simulation proved to be possible with two sites (after being found impossible with a single site) and the results are seen in Figure 4.4 and tabulated in Table 4.4. When simulating the two completely overlapping sites it was found that the overall spectral shape was extremely sensitive to changes in both $\chi$ values but very insensitive to changes in $\eta_Q$. This insensitivity is reflected in the large errors associated with $\eta_Q$ for both sites.

**Table 4.4**
**Quadrupolar and chemical shift parameters for benzamide**

| Site | X–H···A | $\chi$ (kHz) Expt. | Calc. | $\eta_Q$ Expt. | Calc. | $\delta$ (ppm) Expt. | Calc. |
|------|---------|------|------|------|------|------|------|
| 1 | N–H···O | 230±5 | 236 | 0.05±0.05 | 0.16 | 8.4* | 7.6 |
| 2 | N–H···O | 180±3 | 172 | 0.10±0.10 | 0.21 | 8.4* | 8.9 |
| **Difference** | | 50±6 | 64 | -0.05±0.11 | -0.05 | 0 | -1.3 |

*Experimental line widths (2.4 ppm) meant that the two overlapping spectra could not be resolved.

Despite difficulties in simulating the benzamide spectrum, the experimentally obtained values compare favourably with the calculated values. The shorter, more linear N–H···O hydrogen bond (Site 2) has a smaller $\chi$ value (180 kHz) and a larger $\eta Q$ value (0.10), indicating that it is the stronger of the two hydrogen bonds. Since the two sites could not be resolved, the experimental chemical shifts are the same, and thus provide no indication of which of the two hydrogen bonds is stronger. However, the calculated values of $\delta$ are in agreement with the experimentally obtained quadrupolar parameters; $\delta$

for site 2 is larger than for site 1 by 1.3 ppm, which indicate that it is indeed the stronger hydrogen bond.

## 4.3. Nicotinamide

The crystal structure of nicotinamide [137] consists of molecules that are stacked along the $a$ axis with a plane-to-plane distance of 3.579 Å. Two intermolecular hydrogen bonds are formed in the crystal. An N–H⋯O hydrogen bond forms between the *anti* NH amide H atoms and the carbonyl oxygen. An additionally stabilizing N–H⋯N bond is formed between the *syn*-oriented amide H atom and the nitrogen of the pyridine ring. The parameters of the hydrogen bond geometry are outlined in Table 4.5. The hydrogen bonding motif is illustrated in Figure 4.6.

**Table 4.5**
**Hydrogen bonded geometry of nicotinamide**

| X–H⋯A | X–H (Å) | H⋯A (Å) | X⋯A (Å) | X–H⋯A (°) |
|---|---|---|---|---|
| N–H⋯N | 1.02 | 2.09 | 3.11 | 164 |
| N–H⋯O | 1.00 | 1.99 | 2.99 | 175 |

A $^2$H NMR spectrum of selectively deuterated nicotinamide was obtained as seen in Figure 4.7. Based on the differential hydrogen bonding seen in the crystal structure of nicotinamide [137], it was expected that the two amide H atoms would possess different NMR parameters, and thus be resolved. However, as in the benzamide case, only a single resonance was seen in the experimental spectrum. Based on the shape of the nicotinamide spectrum, the possibility of $NH_2$ flipping was ruled out. Thus, it appeared that once again the two spinning sideband manifolds were simply overlapping. In order to confirm this idea, calculations were performed.
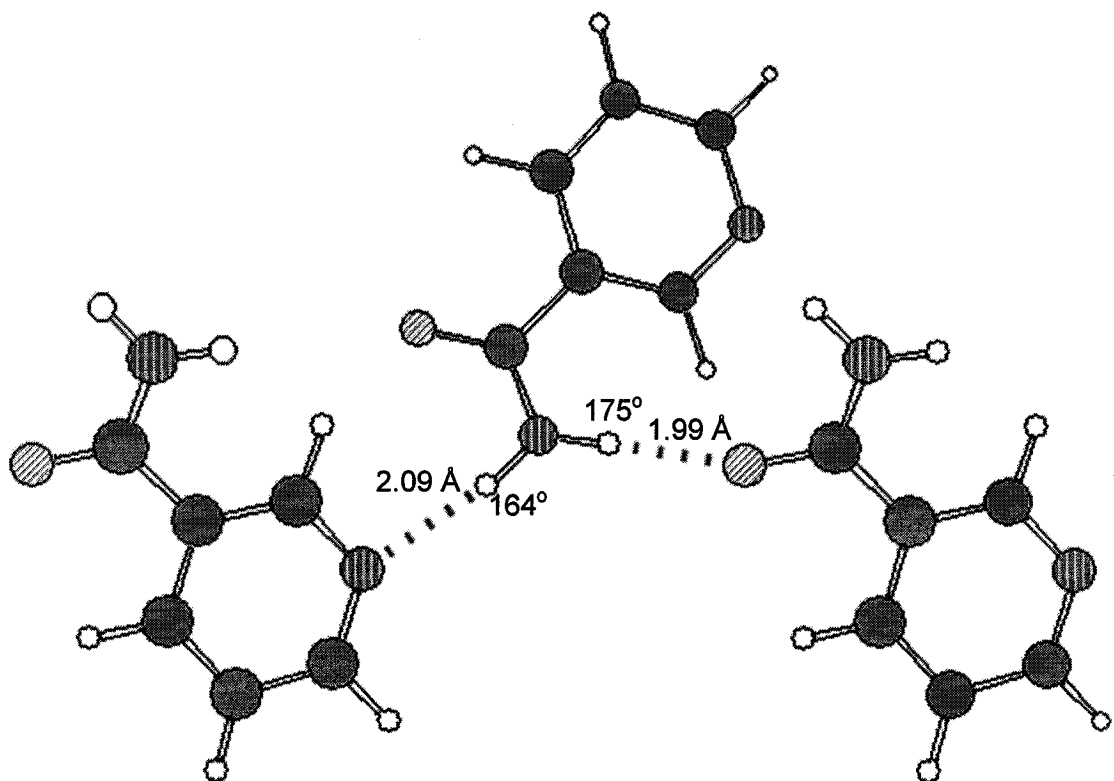
**Figure 4.6** A hydrogen-bonded chain in nicotinamide. Atom designations are provided in the Appendix.

A trimer from the nicotinamide neutron structure [137] was used to calculate the chemical shift, while a pentamer was used to calculate the quadrupolar parameters. The results of these calculations are provided in Table 4.6. The calculations show that in theory the two hydrogen-bonding amide H atoms are set 0.3 ppm apart. Such resolution is not easily achievable, especially where line widths are quite large (4.8 ppm in this case).

In order to confirm the presence of two completely overlapping sites, the experimentally obtained nicotinamide spectrum was simulated using the Simpson simulation package. As was the case with benzamide, simulation with two sites worked while simulation with a single site failed. The simulated spectrum and the NMR parameters extracted from it are seen in Figure 4.7 and Table 4.6, respectively. When simulating the two completely overlapping sites it was found that the overall spectral shape was extremely sensitive to changes in $\chi$ but very insensitive to changes in $\eta_Q$. This insensitivity is reflected in the large errors associated with $\eta_Q$ for both sites.

**(a)**

**(b)**

200000        100000        0        -100000        -200000

kHz
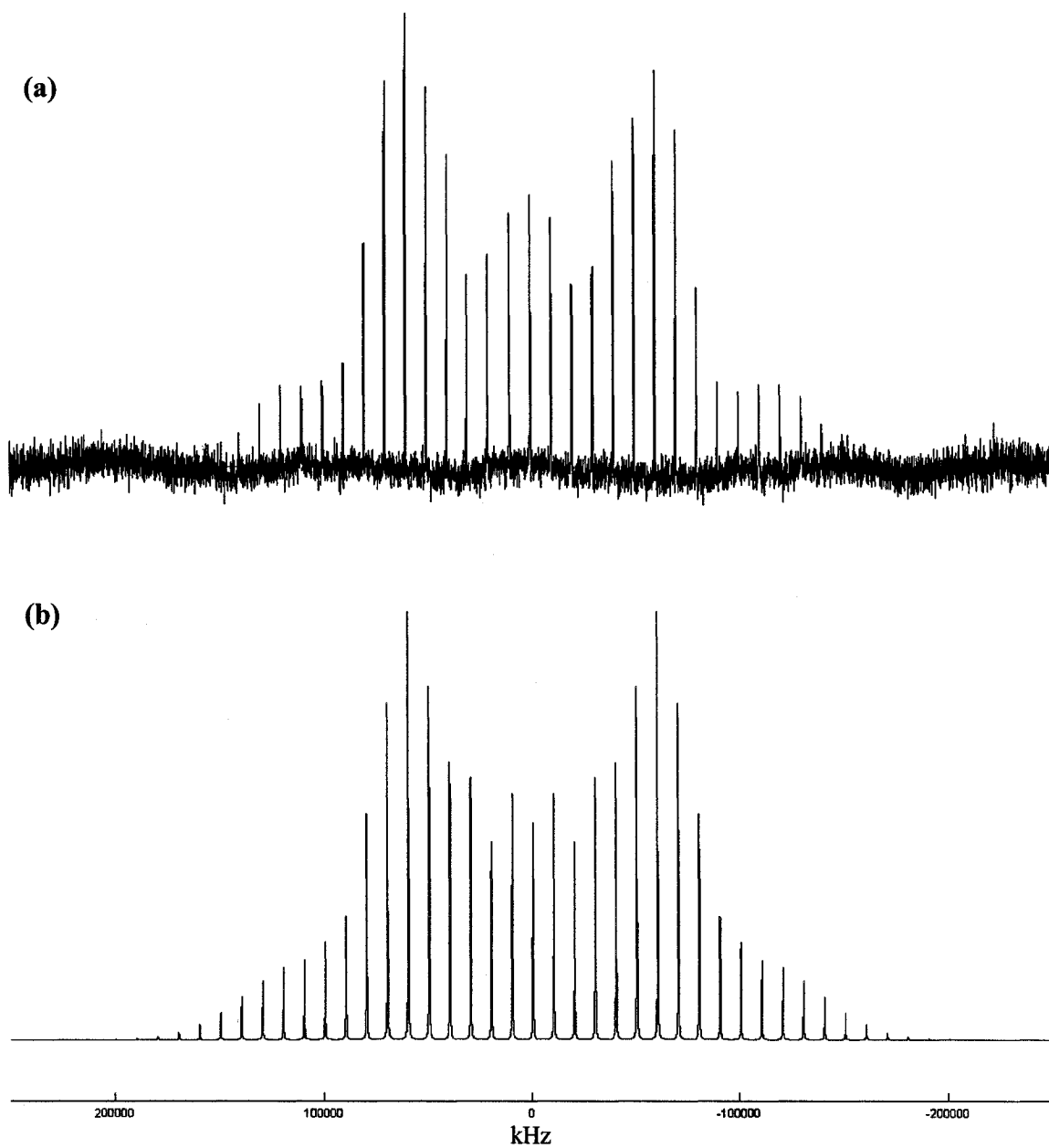
**Figure 4.7**      $^2$H MAS spectrum of nicotinamide-d$_2$: (a) Experimental (b) Simulation.

**Table 4.6**
**Quadrupolar and chemical shift parameters for nicotinamide**

| Site | X–H···A | $\chi$ (kHz) Expt. | $\chi$ (kHz) Calc. | $\eta_Q$ Expt. | $\eta_Q$ Calc. | $\delta$ (ppm) Expt. | $\delta$ (ppm) Calc. |
|------|---------|------|------|------|------|------|------|
| 1 | N–H···N | 220±5 | 266 | 0.10±0.10 | 0.17 | 7.7[*] | 7.3 |
| 2 | N–H···O | 180±4 | 245 | 0.15±0.10 | 0.17 | 7.7[*] | 7.0 |
| **Difference** | | 40±6 | 21 | -0.05±0.14 | 0.00 | 0 | -0.3 |

*Experimental line widths (4.8 ppm) meant that the two overlapping spectra could not be resolved.

The values of $\chi$ extracted from the 2-site simulation are much different than the calculated values. The experimental values of $\chi$ for the N–H···N and N–H···O bonds are 27% and 17% lower than the values determined computationally. The reason for the large error is not understood, and it can only be assumed that if resolution of the two sites was achieved the accuracy of the experimental values would increase. Nevertheless, both the experimental and calculated differences between $\chi$ values (for Site 1 and 2) indicate that the N–H···O bond is the stronger of the two. The values of $\eta_Q$ and $\delta$ do not provide any further evidence for this conclusion. The values of $\eta_Q$ obtained experimentally had large errors associated with them, making a comparison impossible. The calculated values of $\eta_Q$ were the same for each site, inferring nothing about the relative strengths of the hydrogen bonds. Since the two sites could not be resolved, the experimental chemical shifts are the same for both, providing no evidence of the relative strengths of the two hydrogen bonds. The calculated values of $\delta$ are extremely close (within 0.3 ppm) and thus the difference between the two values is almost equal to the error determined for such calculations (±0.29 ppm). Therefore, in this case the calculated chemical shifts cannot be used to determine relative hydrogen bond strengths.

# 5.    Investigation of 2-Aminopyridine

The crystal structure of 2-aminopyridine [138] consists of molecules linked together in centrosymmetric dimers via pairs of N–H⋯N hydrogen bonds. Only one of the two amino H atoms participates in this hydrogen bonding, as seen in Figure 5.1. The crystal structure of 2-aminopyridine is extremely interesting in terms of this work, as it allows the QCC of a hydrogen bonding amino H and a non-hydrogen bonding amino H to be determined simultaneously. The geometry of the hydrogen-bonding amino H is outlined in Table 5.1.

| Table 5.1 Hydrogen bonded geometry of 2-aminopyridine | | | | |
|---|---|---|---|---|
| X–H⋯A | X–H (Å) | H⋯A (Å) | X⋯A (Å) | X–H⋯A (°) |
| N–H⋯N | 0.92 | 2.15 | 3.07 | 171 |

A $^2$H NMR spectrum of selectively deuterated 2-aminopyridine was obtained using 10 kHz sample spinning, see Figure 5.1. The hydrogen bonded and non-hydrogen bonded amino H atoms were seen as two overlapping spinning sideband manifolds, offset by 2.7 ppm. Due to large line widths, the two sites were only partially resolved, as seen in Figure 5.2. In order to simulate the partially resolved sites, a Simpson two-site input file was used; the results of this simulation are seen in Figure 5.2. The values of $\chi$, $\eta_Q$ and $\delta$ extracted from the simulation are tabulated in Table 5.2.

The X-ray structure of 2-aminopyridine contained N–H bond lengths that were shorter than expected based on standard bond lengths. Thus, an optimization of the two amino hydrogen positions was performed to 'normalize' these lengths (see Appendix D for normalized lengths). Calculations of the quadrupolar and chemical shift parameters were performed on the isolated dimer and the results are given in Table 5.2.

108
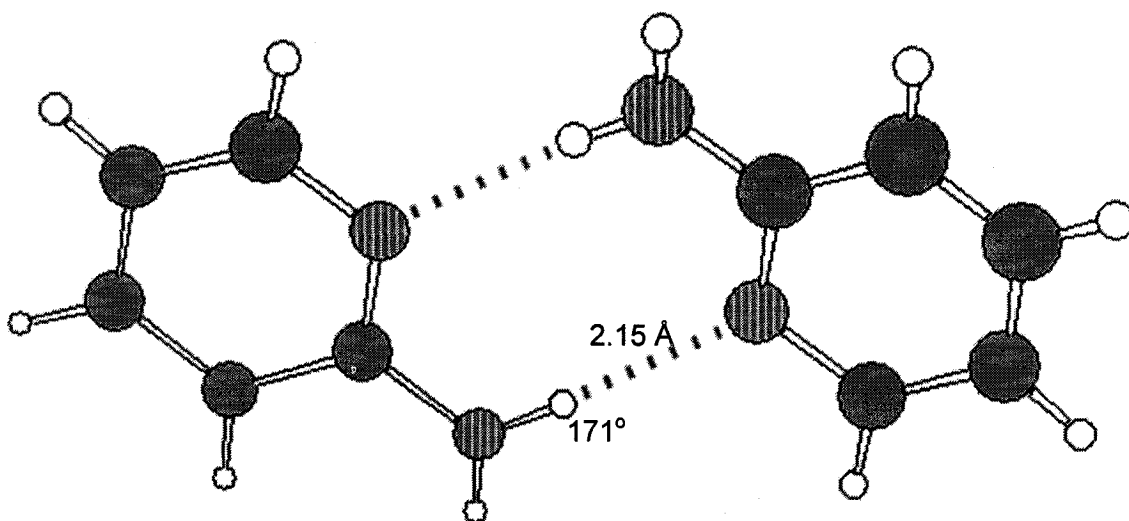
**Figure 5.1**  A centrosymmetric dimer of 2-aminopyridine. Atom designations are provided in the Appendix.
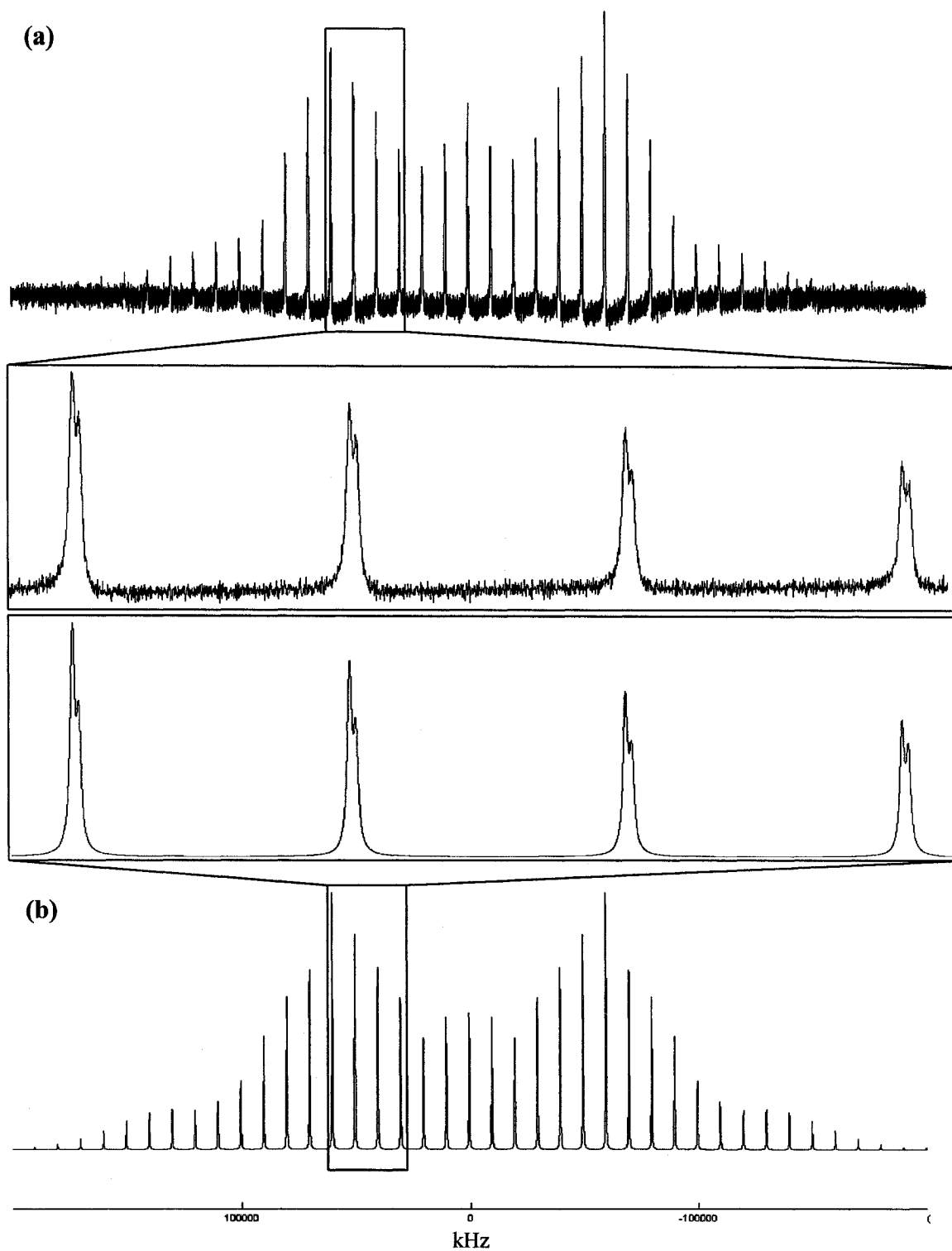
**Figure 5.2**    $^2$H MAS spectrum of 2-aminopyridine-d$_2$: (a) Experimental (b) Simulation. Inset: Partially resolved resonances seen in the experimental and simulated spectra.

**Table 5.2**
**Quadrupolar and chemical shift parameters for 2-aminopyridine**

| Site | X–H⋯A | $\chi$ (kHz) Expt. | $\chi$ (kHz) Calc. | $\eta_Q$ Expt. | $\eta_Q$ Calc. | $\delta$ (ppm) Expt. | $\delta$ (ppm) Calc. |
|------|--------|------|------|------|------|------|------|
| 1 | N–H | 230±10 | 259 | 0.20±0.05 | 0.19 | 5.2 | 3.3 |
| 2 | N–H⋯N | 180±5 | 199 | 0.20±0.05 | 0.23 | 8.3 | 8.1 |
| **Difference** | | 50±11 | 60 | 0±0.07 | -0.04 | -3.1 | -4.8 |

The calculated quadrupolar and chemical shift parameters compare favourably with those determined experimentally. The amino H atom involved in the hydrogen bond has a much smaller $\chi$ value (180 kHz) than its non-hydrogen bonding counterpart. This is as expected since $^2$H QCCs are known to decrease upon hydrogen bond formation. The hydrogen bonding H atom has a much larger value of $\delta$ than the non-hydrogen bonding H atom. Such a difference is expected as $^2$H chemical shifts tend to increase upon hydrogen bond formation. The amino H atoms have very similar $\eta_Q$ values, which is unexpected as one H atom participates in hydrogen bonding while the other does not. The $\eta_Q$ value may remain unchanged in this case due to the weakness of the N–H⋯N hydrogen bond (i.e. relative to the strength of an O–H⋯O bond which is known to affect $\eta_Q$).

# 6. Investigation of Hydrogen Bonds Involving O–H Donors

Using $^2$H NMR it is also possible to investigate hydrogen bond situations

involving distinct donors. Such studies provide an advantage, as investigating two

separate donors should result in distinct chemical shifts so that problem of overlapping

spectral lines (as seen in two of the amide cases) can be avoided. O–H$\cdots$O hydrogen

bonds are very common and thus finding structures in which two O–H donors (within the

same molecule) participate in different hydrogen bonding situations was simple. By

measuring $\chi$, $\eta_Q$ and $\delta$ of the two donors using NMR spectroscopy the relative strengths

of the distinct hydrogen-bonding interactions can be inferred.

## 6.1. Salicylic acid

The crystal structure of salicylic acid [139] consists of hydrogen bonded cyclic

dimers with inversion symmetry, a kind of association that is well known for the majority

of carboxylic acids. Two hydrogen bonds exist in the structure; a nearly linear

intermolecular O–H$\cdots$O bond and a less linear intramolecular O–H$\cdots$O bond (the

deviation a result of the molecular geometry). The dimensions of the hydrogen bonds are

given in Table 6.1. The hydrogen bonding motif is illustrated in Figure 6.1.

**Table 6.1**
**Hydrogen bonded geometry of salicylic acid**

| X–H$\cdots$A | X–H (Å) | H$\cdots$A (Å) | X$\cdots$A (Å) | X–H$\cdots$A (°) |
|---|---|---|---|---|
| O–H$\cdots$O | 0.96 | 1.77 | 2.61 | 145 |
| O–H$\cdots$O | 0.99 | 1.65 | 2.64 | 179 |
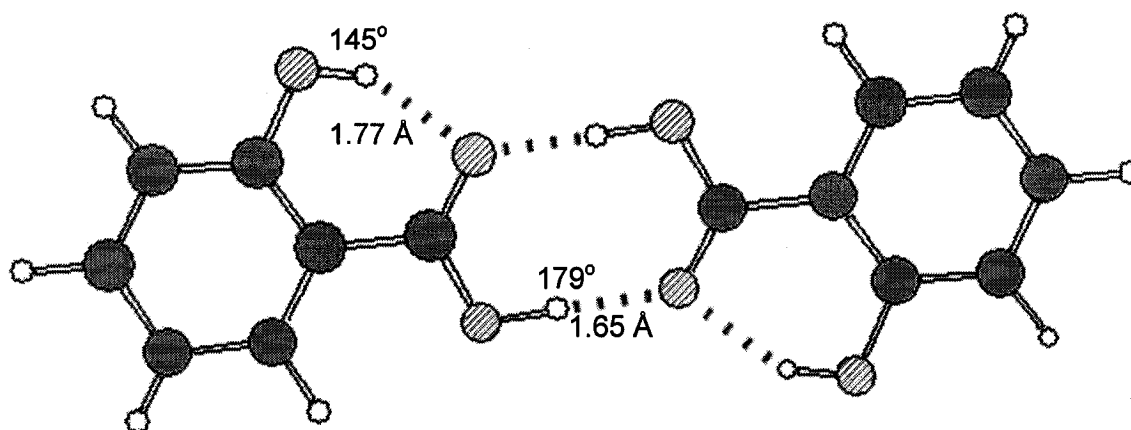
**Figure 6.1**     A hydrogen bonded cyclic dimer of salicylic acid. Atom designations are provided in the Appendix.

**(a)**

**(b)**

**(c)**

100000                    0                    -100000
                       kHz
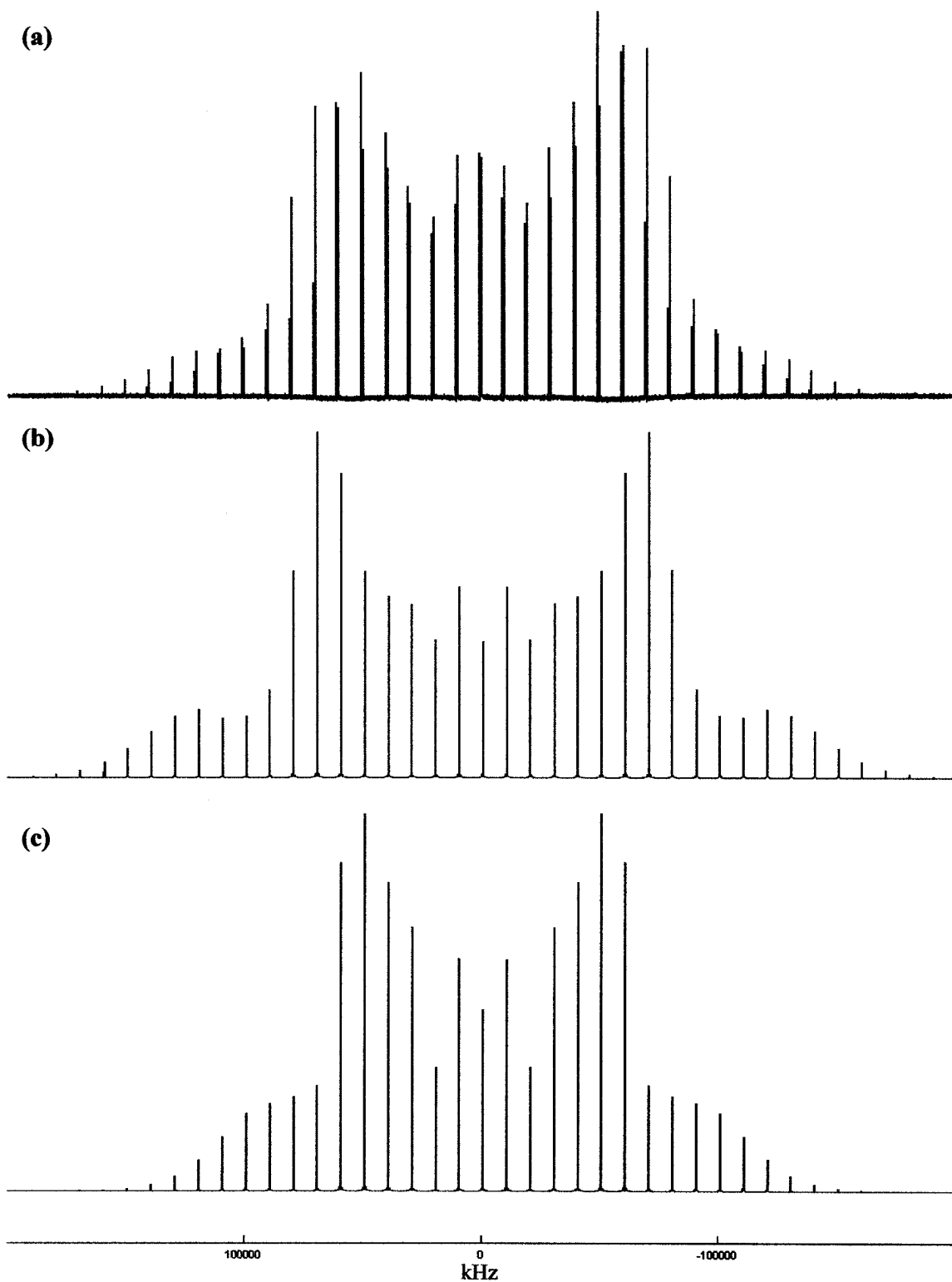
Figure 6.2    $^2$H MAS spectrum of salicylic acid-d$_2$: (a) Experimental (the two sites have been highlighted for clarity) (b) Simulation - site 1 (c) Simulation -site 2.

114

A $^2$H NMR spectrum of selectively deuterated salicylic acid was obtained with a sample spinning speed of 10 kHz, see Figure 6.2. The effect of the differential hydrogen bonding was seen as two overlapping spinning sideband manifolds, offset by 2 ppm.

Simulations of the two separate sites were performed using the Simpson simulation program, the results are illustrated in Figure 6.2. The values of $\chi$, $\eta_Q$ and $\delta$ extracted from the simulations are tabulated in Table 6.2.

An isolated dimer from the neutron structure [139] of salicylic acid at 296 K was used to calculate both the quadrupolar and chemical shift parameters, the results are given in Table 6.2.

**Table 6.2**
**Quadrupolar and chemical shift parameters for salicylic acid**

| Site | X–H⋯A | $\chi$ (kHz) Expt. | Calc. | $\eta_Q$ Expt. | Calc. | $\delta$ (ppm) Expt. | Calc. |
|------|--------|------|-------|------|-------|------|-------|
| 1 | O–H⋯O | 213±5 | 229 | 0.05±0.05 | 0.17 | 8.9 | 9.6 |
| 2 | O–H⋯O | 169±5 | 188 | 0.15±0.05 | 0.15 | 10.9 | 11.6 |
| Difference | | 44±7 | 41 | -0.10±0.07 | 0.02 | -2.0 | -2.0 |

The values obtained experimentally are found to be quite similar to the values determined computationally, with one exception. The calculated value of $\eta_Q$ is larger for Site 1 and smaller for Site 2, while the experimental values show the opposite trend. The error may be the result of using an isolated dimer to calculate the quadrupolar parameters rather than a more extended cluster. The experimentally determined value of $\chi$ is larger for Site 1 than Site 2, inferring that the intermolecular hydrogen bond is stronger than the intramolecular hydrogen bond. Further evidence to this end is provided by the chemical shift values. The experimental value of $\delta$ is much smaller for the intramolecular hydrogen bond (8.9 ppm) than for the intermolecular hydrogen bond (10.9 ppm), implying the latter

is stronger. Due to the contradicting values of $\eta_Q$ (experimental and calculated), the relative strengths of the hydrogen bonds cannot be deduced using this parameter.

## 6.2. Catechol

In the crystal structure of catechol [140], pairs of molecules are linked together by means of two hydrogen bonds. Successive pairs of molecules form thick layers by means of a further system of hydrogen bonds which form helical chains. The dimensions of the two types of O–H$\cdots$O hydrogen bonds are given in Table 6.3. The hydrogen bonding motif is illustrated in Figure 6.3.

**Table 6.3**
**Hydrogen bonded geometry of catechol**

| X–H$\cdots$A | X–H (Å) | H$\cdots$A (Å) | X$\cdots$A (Å) | X–H$\cdots$A (°) |
|---|---|---|---|---|
| O–H$\cdots$O | 0.70 | 2.12 | 2.82 | 146 |
| O–H$\cdots$O | 0.81 | 1.99 | 2.80 | 170 |

A $^2$H NMR spectrum of selectively deuterated catechol was obtained as seen in Figure 6.4. The effect of the differential hydrogen bonding was seen as two overlapping spinning sideband manifolds, offset by 1.4 ppm. The two separate sites were simulated independently, the results of these simulations are illustrated in Figure 6.4. The values of $\chi$, $\eta_Q$ and $\delta$ extracted from the simulations are tabulated in Table 6.4.

The X-ray structure of catechol [140] severely underestimated the O–H bond lengths and thus it was necessary to optimize the hydrogen positions before further calculations could be performed. A table of the hydrogen bond geometries after the hydrogen positions were optimized is found in Appendix D. A hexamer (with hydrogen

116

positions optimized) was used to calculate the quadrupolar and chemical shift parameters.

The results of these calculations are given in Table 6.4.
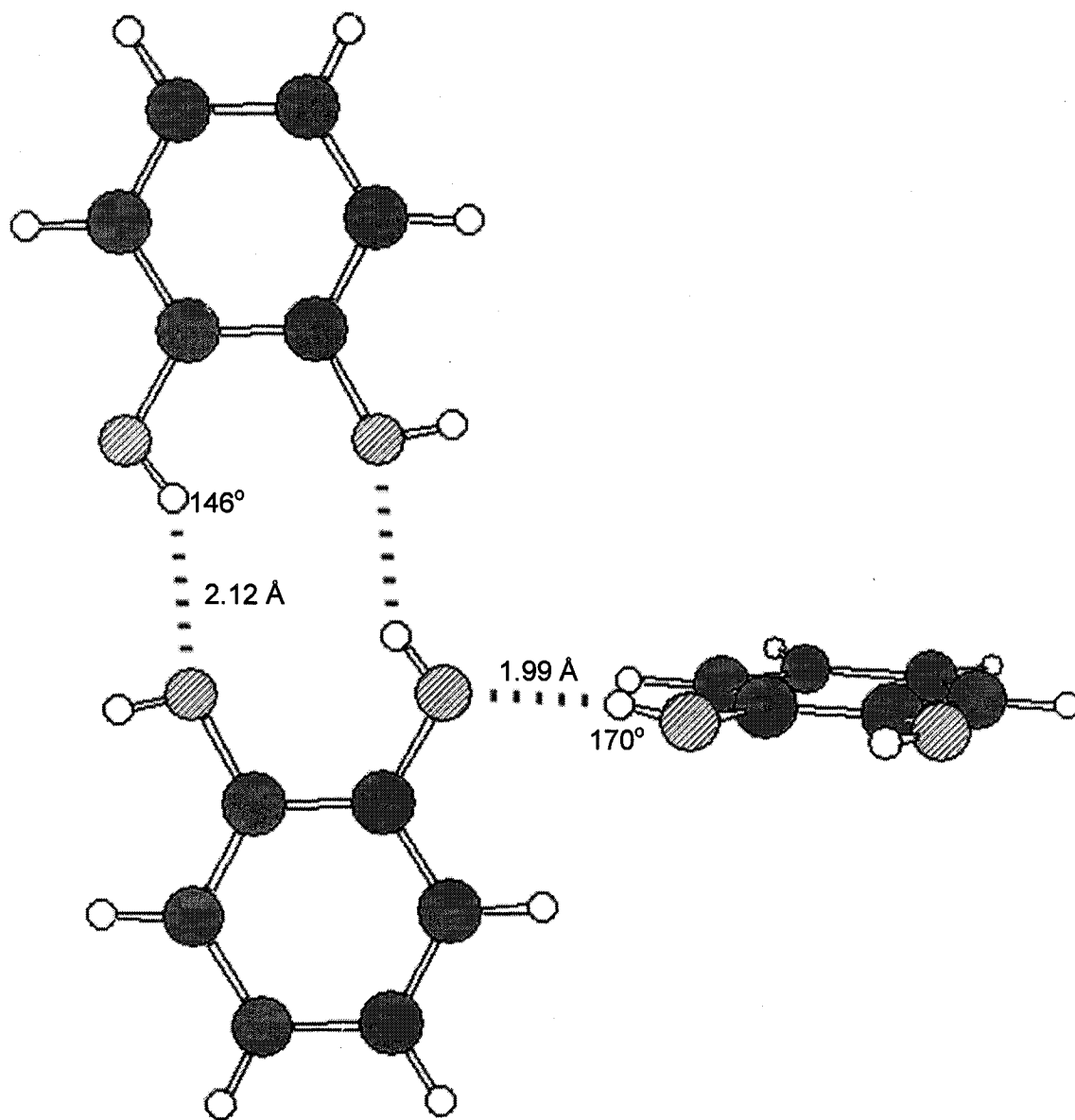
**Figure 6.3** A hydrogen-bonded chain in catechol. Atom designations are provided in the Appendix.

**(a)**

**(b)**

**(c)**

|                | 100000 | 0 | -100000 |
|                |        |   |         |

kHz
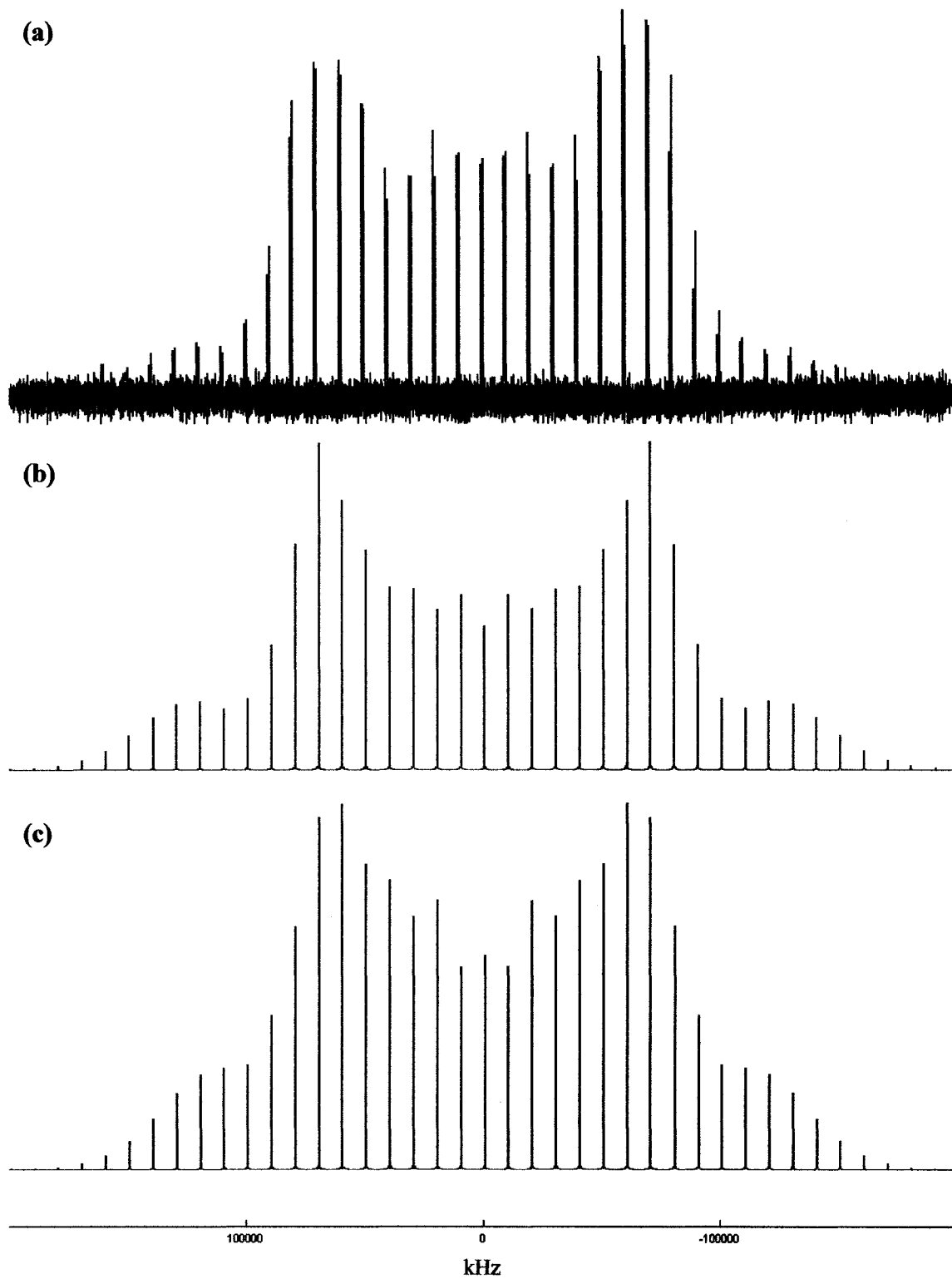
**Figure 6.4** $^2$H MAS spectrum of catechol-d$_2$: (a) Experimental (the two sites have been highlighted for clarity) (b) Simulation - site 1 (c) Simulation -site 2.

119

**Table 6.4**
**Quadrupolar and chemical shift parameters for catechol**

| Site | X–H···A | $\chi$ (kHz) Expt. | Calc. | $\eta_Q$ Expt. | Calc. | $\delta$ (ppm) Expt. | Calc. |
|------|---------|------|-------|------|-------|------|-------|
| 1 | O–H···O | 217±5 | 231 | 0.15±0.10 | 0.13 | 6.6 | 7.5 |
| 2 | O–H···O | 205±3 | 210 | 0.25±0.08 | 0.14 | 8.0 | 7.9 |
| **Difference** | | 12±6 | 21 | -0.10±0.13 | 0.01 | -1.4 | -0.4 |

Within experimental error, the values obtained from the simulations were found to be quite similar to the values determined computationally. Both the calculated and experimentally obtained values of $\chi$ are larger for Site 1 than Site 2, indicating that the shorter, more linear hydrogen bond (Site 2) is the stronger of two. The strength of Site 2 is further evidenced by the values of the chemical shift which are higher for this more linear hydrogen bond. The values of $\eta_Q$ are interpreted with caution as the experimental values have large errors associated with them, and the calculated values are extremely close (0.13 for Site 1 and 0.14 for Site 2). Nevertheless, the values of $\eta_Q$ are larger for Site 2 and smaller for Site 1, indicating that Site 2 is the stronger of the two O–H···O bonds.

## 6.3. Pyridine-3,5-dicarboxylic Acid

The crystal structure of pyridine-3,5-dicarboxylic acid [141] consists of molecules linked together in infinite two-dimensional planar sheets by a strong O–H···O and a strong O–H···N hydrogen bond. The hydrogen bonding motif is illustrated in Figure 6.5. The dimensions of the hydrogen bonds are given in Table 6.5.
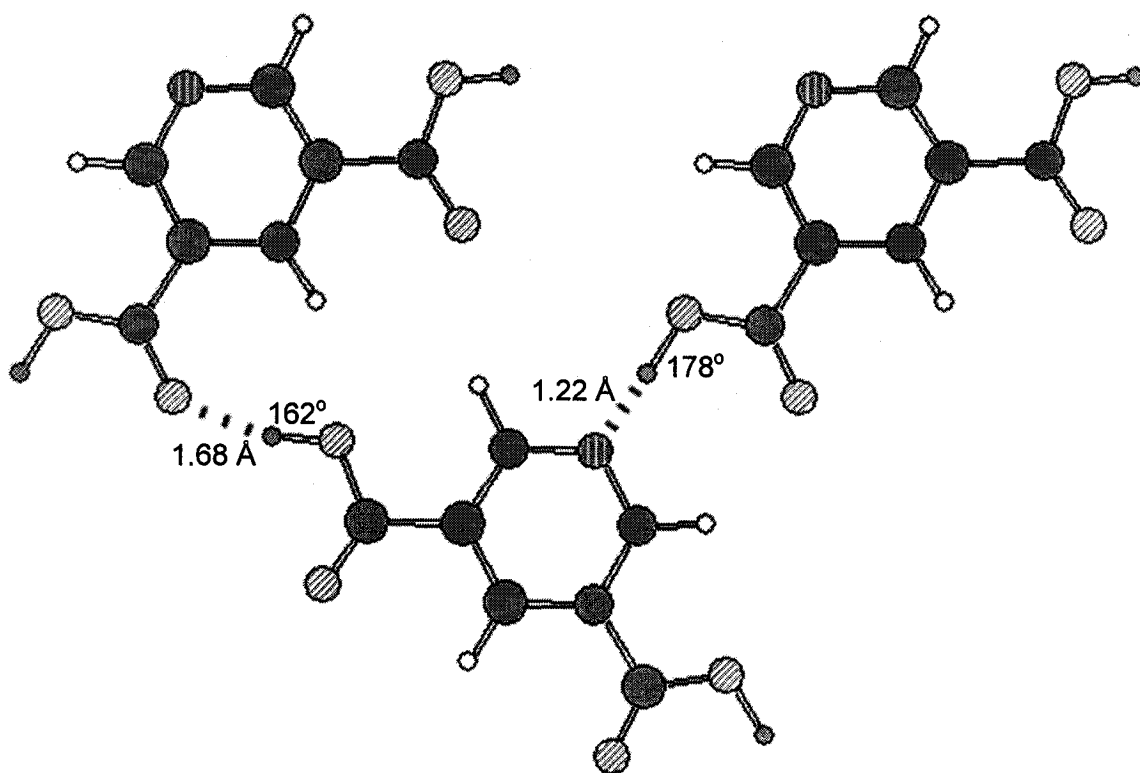
**Figure 6.5**   A hydrogen-bonded chain in pyridine-3,5-dicarboxylic acid-d$_2$.  Atom designations are provided in the Appendix.

**Table 6.5**
**Hydrogen bonded geometry of pyridine-3,5-dicarboxylic acid**

| X–H⋯A | X–H (Å) | H⋯A (Å) | X⋯A (Å) | X–H⋯A (°) |
|---|---|---|---|---|
| O–H⋯O | 0.99 | 1.68 | 2.64 | 162 |
| O–H⋯N | 1.11 | 1.46 | 2.56 | 178 |

A $^2$H NMR spectrum of pyridine-3,5-dicarboxylic acid-$d_2$ was obtained, as seen

in Figure 6.6. The effect of the differential hydrogen bonding was seen as two

overlapping spinning sideband manifolds, offset by 5.8 ppm. The two separate sites were

simulated independently, the results of which are illustrated in Figure 6.6 and tabulated in

Table 6.6.

A tetramer from the neutron structure of deuterated pyridine-3,5-dicarboxylic acid

[141] was used as the basis for the calculations. The results of these calculations are

given in Table 6.6.

**(a)**

**(b)**

**(c)**

100000          0          -100000

kHz
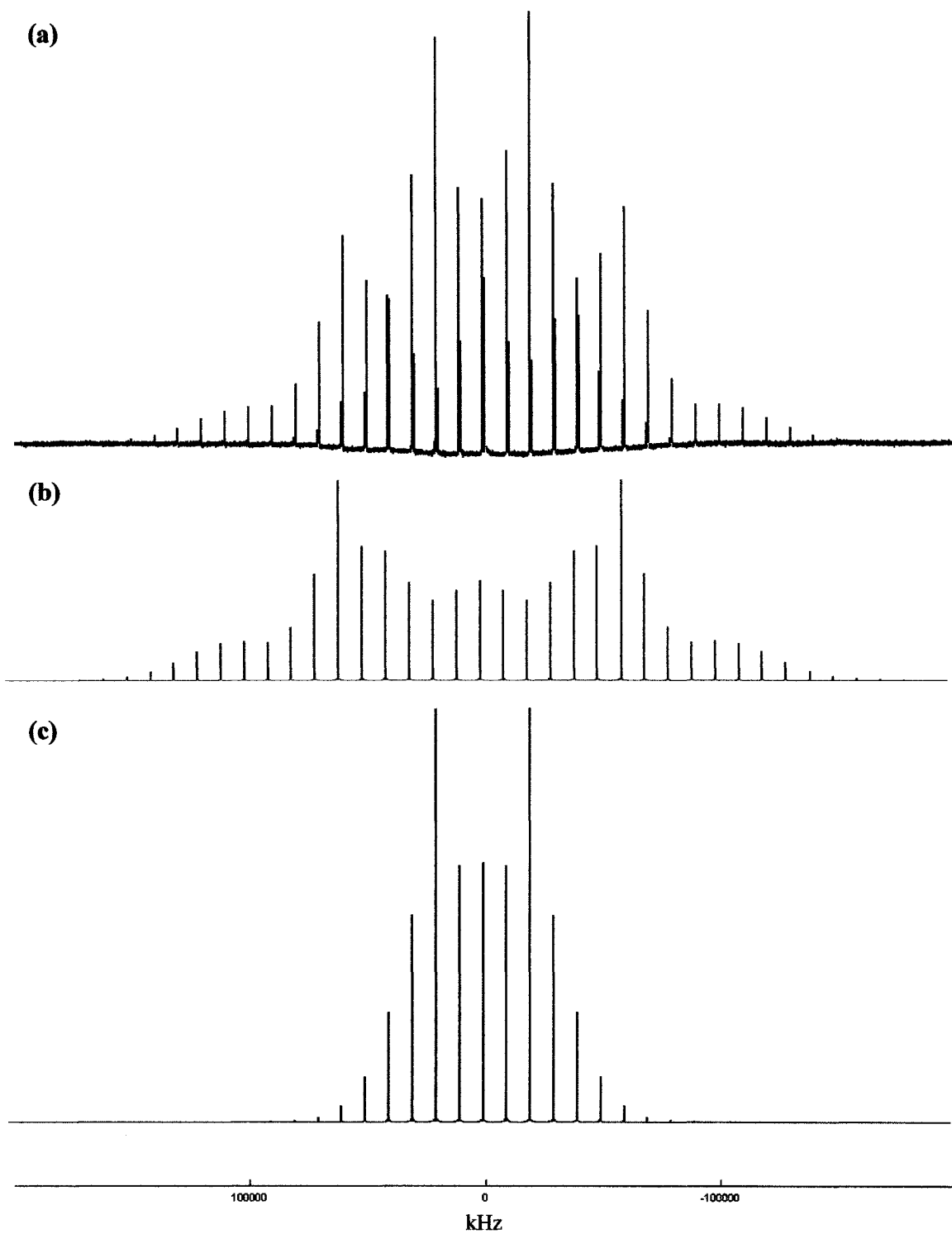
**Figure 6.6**   $^2$H MAS spectrum of pyridine-3,5-dicarboxylic acid-$d_2$: (a) Experimental (the two sites have been highlighted for clarity) (b) Simulation - site 1 (c) Simulation -site 2.

123

## Table 6.6
### Quadrupolar and chemical shift parameters for pyridine-3,5-dicarboxylic acid

| Site | X–H⋯A | $\chi$ (kHz) Expt. | Calc. | $\eta_Q$ Expt. | Calc. | $\delta$ (ppm) Expt. | Calc. |
|------|--------|------|------|------|------|------|------|
| 1 | O–H⋯O | 188±12 | 209 | 0.10±0.05 | 0.11 | 12.3 | 10.9 |
| 2 | O–H⋯N | 75±3 | 71 | 0.18±0.10 | 0.29 | 18.1 | 17.3 |
| **Difference** | | 113±12 | 138 | -0.08±0.11 | -0.18 | -5.8 | -6.4 |

The values calculated for the pyridine-3,5-dicarboxylic acid tetramer compared well with the values obtained experimentally. The values of $\chi$ for the two different hydrogen bonds were found to differ by 113 kHz! Using the geometry of the two hydrogen bonds, this large difference is easily explained. The O–H⋯O hydrogen bond has a small O–H distance (0.99 Å) and a much longer H⋯O separation (1.68 Å). Thus, the efg at the hydrogen results mainly from the oxygen to which it is strongly bonded, and to a lesser extent the oxygen with which it is weakly interacting. The O–H⋯N hydrogen bond has a very elongated O–H distance, and as a result the O–H and H⋯N separations are similar at 1.11 Å and 1.46 Å, respectively. Oxygen and nitrogen are relatively the same in terms of electronegativity, and as a result their independent contributions to the efg at the hydrogen atom nearly cancel; the result is an extremely low QCC.

According to the QCC data, the O–H⋯N hydrogen bond appears to be much stronger than the O–H⋯O hydrogen bond. The asymmetry parameter data also infers such a conclusion, as the O–H⋯N hydrogen bond has a much larger value of $\eta_Q$. The chemical shift data is almost as striking as the QCC data; the chemical shift difference for the two sites is 5.8 ppm! The larger value of $\delta$ is associated with the O–H⋯N hydrogen bond indicating that it is the stronger of the two interactions.

### 6.3.1. *Proton Migration in Pyridine-3,5-dicarboxylic acid*

The protonated structure of pyridine-3,5-dicarboxylic acid contains a very short

O···H···N hydrogen bond [O···N 2.52 Å at 15 K] [141]. Upon heating to room temperature,

the O–H bond length decreases by 0.093 Å and the N–H bond length increases by 0.095

Å, equivalent to the proton migrating ~0.1 Å across the hydrogen bond. The overall O···N

distance does not change significantly with temperature. The O–H···O hydrogen bond in

pyridine-3,5-dicarboxylic acid is also affected by temperature changes. The O···O

distance of the hydrogen bond increases by 0.022 Å upon heating to room temperature.

As expected, the O–H distance increases (0.022 Å) as the O···O distance decreases and

the H···O distance consequently decreases (0.050 Å).

In deuterated pyridine-3,5-dicarboxylic acid, the temperature-dependent changes

are much more pronounced. On heating to room temperature the O–D bond length

decreases by 0.280 Å and the O–D bond length increases by 0.306 Å; equivalent to the

proton migrating ~0.3 Å! In the O–D···O hydrogen bond the O···O distance increases by

0.078 Å in going from 15 to 296 K.

[2]H QCCs have been correlated with hydrogen bond geometry, specifically donor

and acceptor separation. Thus, the deuteron migration observed in pyridine-3,5-

dicarboxylic acid should affect the $\chi$ values for both of the deuterons involved. In order

to investigate this hypothesis, calculations were performed on the crystal structures

obtained at 15, 150 and 296 K. The results of these calculations are provided in Table 6.7.

**Table 6.7**
**The effects of temperature-dependent deuteron migration on the quadrupolar parameters**

| Temp. (K) | X···A (Å) | X–H (Å) | H···A (Å) | $\chi$ (kHz) | $\eta$ |
|-----------|-----------|---------|-----------|--------------|--------|
|           | O···N     | O–H     | H···N     |              |        |
| 296       | 2.564     | 1.457   | 1.107     | 51           | 0.39   |
| 150       | 2.531     | 1.192   | 1.341     | 21           | 0.96   |
| 15        | 2.537     | 1.151   | 1.388     | 40           | 0.54   |
|           | O···O     | O–H     | H···O     |              |        |
| 296       | 2.640     | 1.677   | 0.993     | 197          | 0.10   |
| 150       | 2.581     | 1.579   | 1.016     | 156          | 0.11   |
| 15        | 2.562     | 1.553   | 1.021     | 146          | 0.13   |

The calculated values show that $\chi$ depends on both the donor-acceptor separation as well as the symmetry of the hydrogen bond (i.e. X–H versus H···A distances). In the case of the O–H···N hydrogen bond, the donor-acceptor separation remains nearly constant at the three different temperatures. However, the symmetry of the hydrogen bond is very different at each of the three temperatures. The hydrogen bond is most symmetric at 150 K (the difference in O–H and H···N distances is a mere 0.15 Å) and most asymmetric at 296 K (the difference in O–H and H···N distances is 0.35 Å). The values of $\chi$ scale accordingly, with the smallest value found for the most symmetric case and the largest value for the most asymmetric case. In the case of the O–H···O hydrogen bond, both the donor-acceptor separation and the asymmetry of the hydrogen bond, decrease with temperature. For the 296 K case, in which the O–H···O hydrogen bond is the longest and most asymmetric, the value of $\chi$ is large. The smallest value of $\chi$ corresponds to the crystal structure at 15 K, in which the hydrogen bond is the shortest and most symmetric.

The calculations also show that the value of the asymmetry parameter depends strongly on the symmetry of the hydrogen bond. The most symmetric O–H···N hydrogen bond (seen at 150 K) has the largest value of $\eta_Q$, while the least symmetric O–H···N hydrogen bond (seen at 296 K) has the smallest value of $\eta_Q$. The symmetry of the O–H···O bond is nearly the same at all three temperatures, and therefore the value of $\eta_Q$ is fairly consistent. Nevertheless, the largest value of $\eta_Q$ is associated with the most symmetric O–H···O hydrogen bond, and the smallest value with the least symmetric hydrogen bond.

Based on these calculations, an NMR investigation of the temperature-dependent deuteron migration in pyridine-3,5-dicarboxylic acid appeared to be an interesting prospect. However, such an investigation was never performed for two reasons. Firstly, the relaxation time of pyridine-3,5-dicarboxylic acid at room temperature is reasonable (~120 s) but at lower temperatures the relaxation delay would be longer, resulting in long experimental times (>24 hours). Secondly, it was seen through other investigations, that as the probe is cooled the MAS rod contracts and the magic angle deviates from its normal value of 54.74°. If the magic-angle is 'off', the characteristic splitting due to the differential hydrogen bonding in pyridine-3,5-dicarboxylic acid would be either absent or not fully resolved due to increased line widths.

# 7. Investigation of Hydrogen Bonds Involving S–H Donors

Though nominally a typical non-metallic element and placed just one position below oxygen in the periodic table, sulfur has a much smaller electronegativity. As a result, the S–H group is a much weaker hydrogen bond donor than the more conventional O/N–H. Due to the inherent weakness of S–H⋯X hydrogen bonds and the small number of accurate crystal structures [142] these interactions have never been studied using solid state NMR spectroscopy. By studying such systems, the effect of S–H⋯X hydrogen bonding on $\chi$, $\eta$ and $\delta$ can be determined.

## 7.1. Thiosalicylic Acid

In crystalline thiosalicylic acid [143], the carboxylic acid groups form hydrogen-bonded dimers, whereas the S–H groups form an infinite S–H⋯S–H⋯S–H hydrogen-bond chain, with an S⋯S distance of 3.99 Å. The dimensions of the two hydrogen bonds are given in Table 7.1. The hydrogen bonding motif is illustrated in Figure 7.1.

**Table 7.1**
**Hydrogen bonded geometry of thiosalicylic acid**

| X–H⋯A | X–H (Å) | H⋯A (Å) | X⋯A (Å) | X–H⋯A (°) |
|---|---|---|---|---|
| S–H⋯S | 1.30 | 2.72 | 3.99 | 164 |
| O–H⋯O | 0.91 | 1.75 | 2.66 | 174 |

A $^2$H NMR spectrum of thiosalicylic-$d_2$ was obtained, as seen in Figure 7.1. The effect of the differential hydrogen bonding was seen as two overlapping spinning sideband manifolds, offset by 8.4 ppm. The two separate sites were simulated independently, the results of which are illustrated in Figure 7.2 and tabulated in Table 7.2.
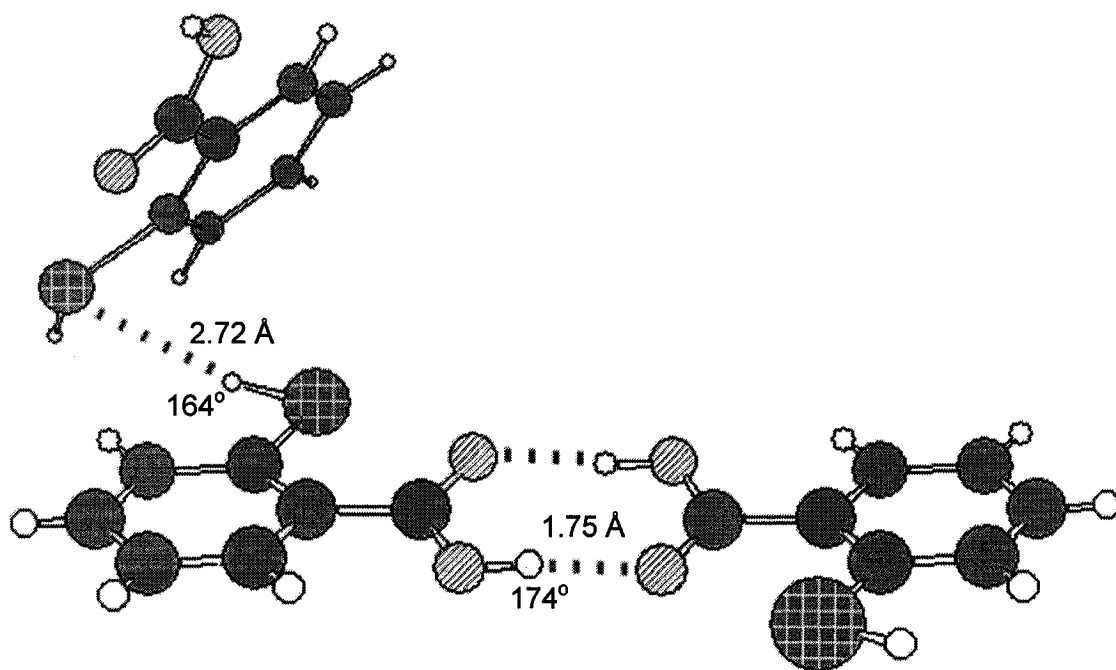
**Figure 7.1** A hydrogen-bonded chain in thiosalicylic acid. Atom designations are provided in the Appendix.

**(a)**

**(b)**

**(c)**

100000          0          -100000
kHz
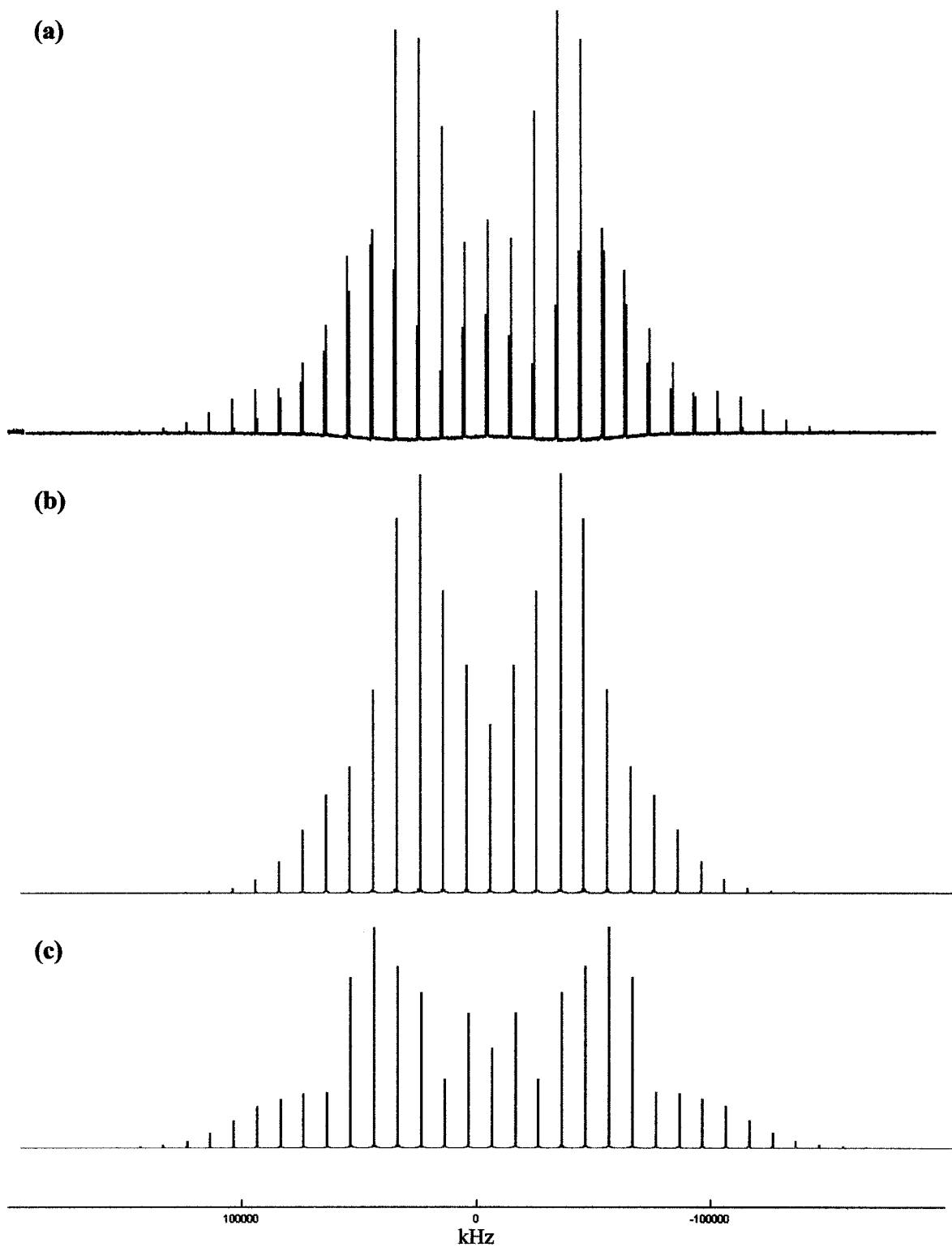
**Figure 7.2**    ²H MAS spectrum of thiosalicylic-d₂: (a) Experimental (the two sites have been highlighted for clarity) (b) Simulation - site 1 (c) Simulation -site 2.

The X-ray structure of thiosalicylic acid [143] contained unreasonably short S–H and O–H bond lengths. Thus the hydrogen positions were optimized (see Appendix D for hydrogen bond geometries after partial optimization), and it was the partially optimized geometry that was used to calculate the appropriate NMR parameters. A tetramer of thiosalicylic acid was used in the calculations, the results of which are found in Table 7.2.

**Table 7.2**
**Quadrupolar and chemical shift parameters for thiosalicylic acid**

| Site | X–H···A | $\chi$ (kHz) | | $\eta_Q$ | | $\delta$ (ppm) | |
|------|---------|-------|-------|-----------|-------|-------|-------|
| | | Expt. | Calc. | Expt. | Calc. | Expt. | Calc. |
| 1 | S–H···S | 125±5 | 112 | 0.05±0.05 | 0.21 | 4.5 | 4.4 |
| 2 | O–H···O | 166±6 | 182 | 0.02±0.02 | 0.14 | 12.9 | 11.6 |
| **Difference** | | -41±8 | -70 | 0.03±0.05 | 0.07 | -8.4 | -7.2 |

Of the two hydrogen bonds the O–H···O hydrogen bond is the shorter, more linear interaction. Thus, one would expect that the O–H···O interaction would possess a larger chemical shift and a smaller QCC than the weaker S–H···S interaction; as seen in Table 7.1, this is certainly not the case. The value of $\delta$ is larger for the shorter, more linear hydrogen bond, as is to be expected. However, the value of $\chi$ for the S–H···S interaction is much smaller than the value for the O–H···O interaction. The reasons for this discrepancy cannot be explained without considering a second S–H donor.

Finding a second compound containing an S–H donor proved to be very difficult. Even for the most common variant, S–H···O, the published material is scarce [144]. Only a handful of appropriate compounds were found, and of these only one, L-cysteine, was commercially available. The crystal structure of L-cysteine [145] is seen in Figure 7.3.

The $^2$H NMR spectrum of L-cysteine was obtained. The spectrum indicated the presence of an N–H···O hydrogen bond, but the deuterons in the S–H···O and S–H···S

bonds were not seen. The reasons for this are unknown, but there are two possible causes:
(1) the thiol deuterons did not exchange in the deuterium oxide solution, or (2) the
relaxation time for the thiol deuterons was too long (i.e. >480 seconds, the relaxation
delay that was employed).

Since physical experiments appeared too difficult considering time constraints, it
was decided that calculations of 2-hydroxythiobenzoic acid would be used to interpret the
thiosalicylic acid results.
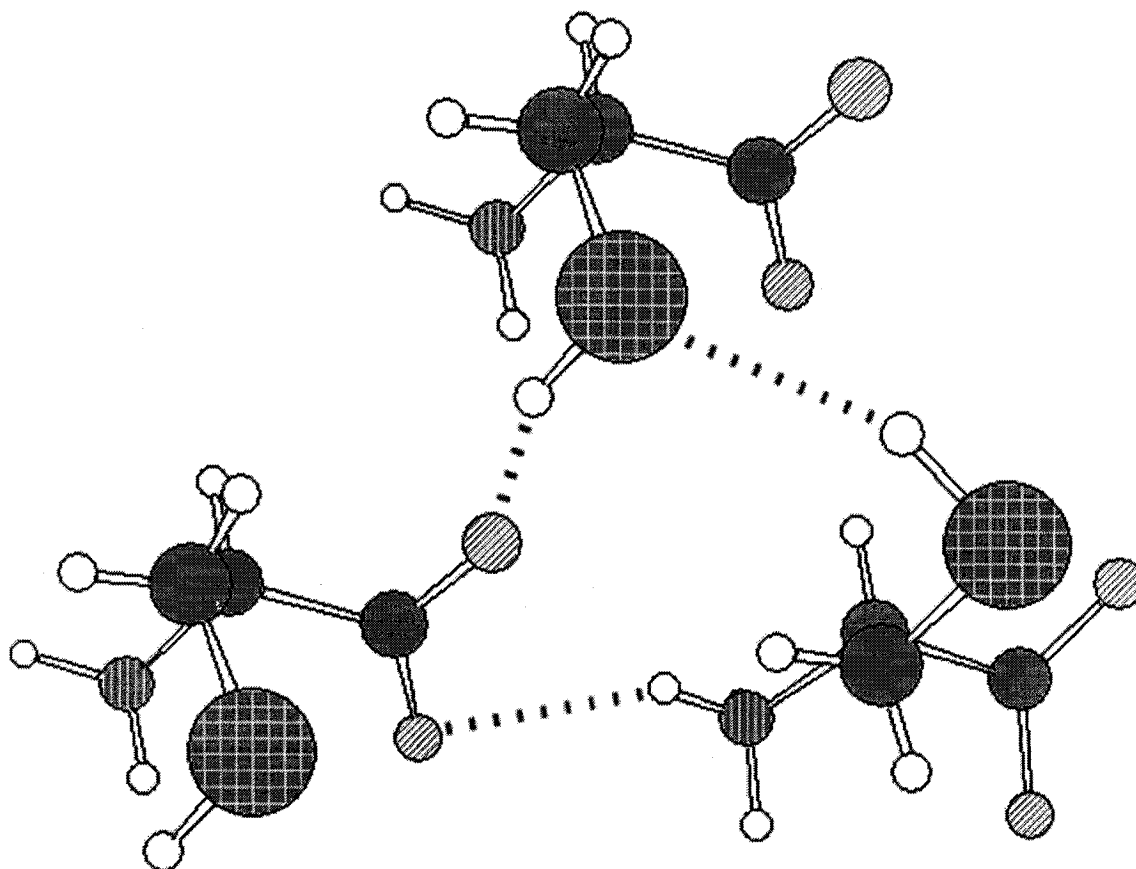


**Figure 7.3**     **Crystal structure of L-cysteine. Atom designations are provided in the
Appendix.**

## 7.2. 2-Hydroxythiobenzoic Acid

The crystal structure of 2-hydroxythiobenzoic acid [146] consists of

centrosymmetric dimers held together by S–H$\cdots$O hydrogen bonds. The structure is

further stabilized by intramolecular O–H$\cdots$O hydrogen bonds. The dimensions of the two

hydrogen bonds are given in Table 7.3. The hydrogen bonding motif is illustrated in

Figure 7.4.

**Table 7.3**
**Hydrogen bonded geometry of 2-hydroxythiobenzoic acid**

| X–H$\cdots$A | X–H (Å) | H$\cdots$A (Å) | X$\cdots$A (Å) | X–H$\cdots$A ($^\circ$) |
|---|---|---|---|---|
| S–H$\cdots$O | 1.40 | 1.99 | 3.39 | 175 |
| O–H$\cdots$O | 0.97 | 1.79 | 2.59 | 138 |

The X-ray structure of 2-hydroxybenzoic acid [146] underestimated the S–H and

O–H bond lengths and thus it was necessary to optimize the hydrogen positions before

further calculations could be performed (see Appendix D for the hydrogen bond

geometries after optimization). An isolated dimer was used to calculate the quadrupolar

and chemical shift parameters. The results of these calculations are given in Table 7.4.

**Table 7.4**
**Quadrupolar and chemical shift**
**parameters for 2-hydroxythiobenzoic acid**

| Site | X–H$\cdots$A | $\chi$ (kHz) Calc. | $\eta_Q$ Calc. | $\delta$ (ppm) Calc. |
|---|---|---|---|---|
| 1 | S–H$\cdots$O | 126 | 0.16 | 6.2 |
| 2 | O–H$\cdots$O | 223 | 0.16 | 9.2 |

The results of the 2-hydroxythiobenzoic acid calculations are similar to the results

seen for thiosalicylic acid. Despite being the weaker hydrogen bond, the S–H$\cdots$O value of

$\chi$ is considerably smaller than the O–H$\cdots$O value of $\chi$.
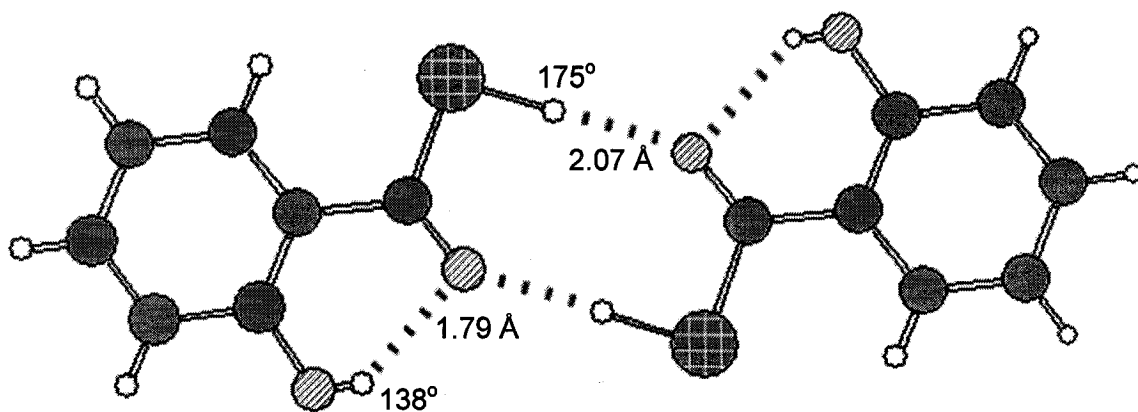
**Figure 7.4** A hydrogen-bonded chain in 2-hydroxythiobenzoic acid. Atom designations are provided in the Appendix.

## 7.3. Comparing the Results of Thiosalicylic Acid and 2-Hydroxythiobenzoic Acid

In order to understand the effect of S–H⋯X hydrogen bonding on the quadrupolar and chemical shift parameters, two S–H⋯X hydrogen bonds (in two different compounds) were investigated. The results of these investigations are summarized in Table 7.5

**Table 7.5**
**Quadrupolar and chemical shift parameters for thiosalicylic acid (S–H⋯S)**
**and 2-hydroxythiobenzoic acid (S–H⋯O)**

| Site | X–H⋯A | $\chi$ (kHz) Expt. | Calc. | $\eta_Q$ Expt. | Calc. | $\delta$ (ppm) Expt. | Calc. |
|------|-------|------|------|------|------|------|------|
| 1 | S–H⋯S | 125±5 | 112 | 0.05±0.05 | 0.21 | 4.5 | 4.1 |
| 2 | S–H⋯O | N/A | 126 | N/A | 0.16 | N/A | 6.2 |
| **Difference** | | | -14 | | 0.05 | | -2.1 |

The S–H⋯O interaction of 2-hydroxythiobenzoic acid is shorter and more linear than the S–H⋯S interaction of thiosalicylic acid. Based on this, one would expect a smaller value of $\chi$ for the S–H⋯O bond, but this is not the case. The value of $\chi$ is composed of two main parts: (1) the contribution from the atom to which the hydrogen is covalently bonded, and (2) the contribution from the atom involved in the hydrogen bonding interaction. It is hypothesized that the S–H⋯S hydrogen bond has a small value of $\chi$ since the contribution to the efg by weakly electronegative atoms is generally small. It is thought that the S–H⋯O interaction has a larger value of $\chi$, since the electronegative O atom increases the value of the efg at the hydrogen atom.

The values of the asymmetry parameter were not as expected. Previous results indicate that stronger hydrogen bonds have larger values of $\eta_Q$. In this case, the stronger hydrogen bond (S–H⋯O) had a smaller value of $\eta_Q$ than the weaker hydrogen bond (S–

H$\cdots$S). The reasons for this were not fully understood. The effect of S–H$\cdots$X hydrogen bonding on the chemical shift was more clear cut. As expected, the stronger hydrogen bond (S–H$\cdots$O) had a larger chemical shift than the weaker hydrogen bond (S–H$\cdots$S).

In general terms, it can be concluded that hydrogen bonds involving S–H donors will have smaller quadrupolar coupling constants than hydrogen bonds involving more conventional donors (i.e. O–H and N–H). In order to fully understand the effects of strong and weak S–H$\cdots$X hydrogen bonds on the value of $\chi$ and $\eta_Q$, more compounds must be investigated.

# 8. Investigation of a Hydrogen Bond Involving a P acceptor

Several different hydrogen bond acceptors were investigated in this work: strong

acceptors included O and N, and weak acceptors included S and $\pi$ systems. Another

acceptor of interest was the very weakly electronegative P atom. In order for P to act as a

hydrogen bond acceptor, its bonding situation must provide an electron lone pair. As a

result, there are exceedingly few crystal structure publications where O/N–H⋯P

hydrogen bonding is discussed.

In order to investigate a specific type of hydrogen bond, it is necessary to study

two or more different examples. In the case of O–H⋯P hydrogen bonds, only two

examples were found in the literature, the strongest of which was found in the crystal

structure of 2-[$t$-Butyl(phenyl)phosphanyl]-4-methylphenol [147] (Figure 8.1). The

hydrogen bond geometry of the compound is provided in Table 8.1.

**Table 8.1**
**Hydrogen bonded geometry of**
**2-[$t$-Butyl(phenyl)phosphanyl]-4-methylphenol**

| X–H⋯A | X–H (Å) | H⋯A (Å) | X⋯A (Å) | X–H⋯A (°) |
|---|---|---|---|---|
| O–H⋯P | 0.77 | 2.42 | 3.19 | 152 |

The difficulty involved in the synthesis of 2-[t-Butyl(phenyl) phosphanyl]-4-

methylphenol [147] required that the investigation be purely computational. The X-ray

structure of the compound contained an O–H bond length that was much shorter than

expected based on standard bond lengths. Thus the hydrogen position was optimized, and

it was the partially optimized geometry (see Appendix D) that was used to calculate the

appropriate NMR parameters. Calculations were performed on a single molecule of
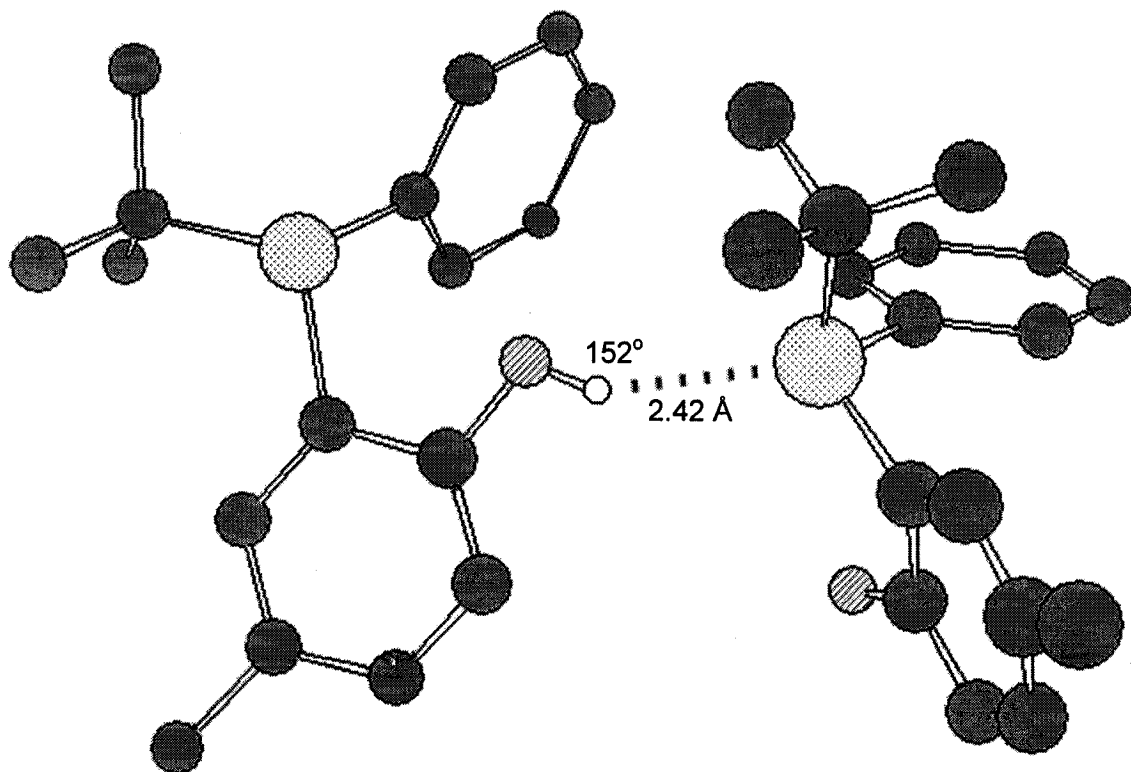
**Figure 8.1**      Intermolecular hydrogen bond in 2-[*t*-Butyl(phenyl)phosphanyl]-4-methylphenol. Hydrogen atoms have been removed for clarity. Atom designations are provided in the Appendix.

2-[t-Butyl(phenyl)phosphanyl]-4-methylphenol as well as on a dimer, the results of these

calculations are given in Table 8.2.

**Table 8.2**
**Quadrupolar and chemical shift parameters**
**for 2-[t-Butyl(phenyl)phosphanyl]-4-methylphenol**

|  | $\chi$ (kHz) Calc. | $\eta_Q$ Calc. | $\delta$ (ppm) Calc. |
|---|---|---|---|
| **Monomer** | 287 | 0.12 | 3.0 |
| **Dimer** | 212 | 0.13 | 6.8 |
| **Difference** | 75 | -0.01 | -3.8 |

As seen from the calculations, upon formation of the hydrogen bonded dimer the

value of $\chi$ drops significantly (by 75 kHz). This reduction in the QCC is consistent with

previous findings. The value of $\eta_Q$ is larger for the dimer; again, this finding is consistent

with trends seen for more conventional hydrogen bonded systems. The value of $\delta$ is much

larger for the hydrogen bonded dimer than for the monomer (6.8 ppm compared to 3.0

ppm), indicating that the hydrogen bond that is formed is relatively strong.

It appears, based on the calculations, that the effect of an O–H$\cdots$P hydrogen bond

on the quadrupolar and chemical shift parameters is similar to the effect caused by more

traditional systems (i.e. O–H$\cdots$O or O–H$\cdots$N). That is, an O–H$\cdots$P interaction results in an

increase in $\eta_Q$ and $\delta$, and a decrease in $\chi$. In order to more fully understand the effect of

weak acceptors on these parameters, more systems must be investigated.

# 9. The Effects of Deuteration

Deuteration of a hydrogen bond often results in an increase in the distance

between donor and acceptor atoms, though generally by an amount smaller than the

standard uncertainties of the bond lengths [95]. The effects of deuteration on hydrogen

bond geometry are demonstrated through a comparison of the crystal structures of

protonated and deuterated pyridine-3,5-dicarboxylic acid [141], as seen in Table 9.1.

**Table 9.1**
**Hydrogen bond geometry in protonated and deuterated pyridine-3,5-dicarboxylic acid**

| Hydrogen Bond | | X···A (Å) | X–H (Å) | H···A (Å) | X–H···A (°) |
|---|---|---|---|---|---|
| O–H···N | Protonated | 2.525 | 1.218 | 1.308 | 177.8 |
| | Deuterated | 2.564 | 1.108 | 1.457 | 177.6 |
| O–H···O | Protonated | 2.591 | 1.004 | 1.608 | 165.0 |
| | Deuterated | 2.640 | 0.993 | 1.678 | 162.1 |

The protonated and deuterated hydrogen bond geometries of pyridine-3,5-dicarboxylic

acid differ substantially. In terms of the O–H···N hydrogen bond, deuteration increases

the donor-acceptor separation by 0.039 Å, but decreases the symmetry (see Introduction,

Section 6.1 for definition) of the hydrogen bond by 0.260 Å. In terms of the O–H···O

hydrogen bond, deuteration lengthens the bond by 0.049 Å overall, and the symmetry

decreases by 0.081 Å. The overall weakening of the hydrogen bond upon deuteration is

as expected, based on the zero point levels of $^1$H and $^2$H (see Introduction, Section 7).

As seen previously in Table 6.7, small changes in the hydrogen bond geometry

(i.e. donor-acceptor separations and hydrogen bond symmetry) can have significant

effects on the calculated values of $\chi$ and $\eta_Q$. In order to obtain calculated results in close

agreement with experimentally obtained values, it is necessary to perform calculations

using the deuterated hydrogen bond geometries. Since deuteration generally causes a

lengthening of the hydrogen bond, calculations using deuterated geometries should provide slightly larger values of $\chi$ than obtained here (using protonated structures). The use of deuterated geometries should increase the difference between experimental results and calculated values, as the calculated values of $\chi$ (using proton structures) were already overestimations.

Deuteration can also result in drastic changes in the crystal structure of a compound. In the case of $KH_2PO_4$, deuteration changes the space group of the molecule from tetragonal to monoclinic [96]. In this study deuteration did not drastically affect the crystal structures; this is evidenced by the strong agreement between experimental and calculated values. If a drastic structural change was suspected, chemical shifts of the protons and deuterons involved in the hydrogen bond could be measured. Provided there were no significant structural changes, the chemical shifts of the H atoms should be the same in the $^1H$ and $^2H$ spectra.

The effect of deuteration on the hydrogen bond geometry of the other compounds studied is unknown, but is assumed to be small. To investigate the changes that occur upon deuteration, neutron diffraction studies on both the protonated and deuterated analogs of each compound investigated must be performed.

# CHAPTER IV

## *SUMMARY AND CONCLUSIONS*

The reported results have demonstrated that $^2$H NMR can be used effectively in the investigation of hydrogen-bonded systems. Selective deuteration of the compounds investigated, such that $^2$H is present *only* in the hydrogen bonds, results in spectra that are unmarred by other hydrogens. The use of magic-angle spinning affords resolution of multiple hydrogen-bonding sites in a single spectrum.

The majority of the compounds investigated were chosen because they possessed two distinct hydrogen bonding situations. In order to fully resolve two sites within a single spectrum, the values of $\delta$ for the two H atoms must differ by a value greater than the line width ($\sim$ 2 ppm in this study). For most of the compounds studied, resolution between the two different sites was achieved. Two compounds, benzamide and nicotinamide, did not offer such resolution and a single spinning sideband manifold was observed. Despite this lack of resolution, accurate values of $\chi$ and $\eta_Q$ for *both* sites were extracted from the simulations.

Experimentally determined quadrupolar and chemical shift parameters were compared to values calculated using crystal structure geometries from X-ray or neutron diffraction studies. Calculated values of the quadrupolar parameters compared favourably with experimental values. The B3LYP method with the 6-311++G** basis set proved to be a reliable method for calculating $\chi$, provided the coefficient eQ/h = 609.4 kHz/a.u. was used to convert the calculated electric field gradients to $^2$H QCCs. Calculated chemical shift parameters also agreed well with experimental results. The B3LYP method with the 6-31G basis set was found to be an inexpensive, yet reliable method for calculating $^1$H chemical shieldings. A simple linear regression technique provided an easy and effective way to convert shielding to shift.

It was demonstrated that the quadrupolar parameters ($\chi$ and $\eta_Q$) are reliable indicators of hydrogen bond strength. Short, symmetrical hydrogen bonds were found to have small values of $\chi$ and large values of $\eta_Q$; longer, more asymmetrical hydrogen bonds were associated with large $\chi$ values and small $\eta_Q$ values. The investigation of a less conventional donor, i.e. S–H, showed that when weakly electronegative atoms are involved in the hydrogen bonding scheme, the values of $\chi$ are larger and the values of $\eta_Q$ are smaller than anticipated. This shows that the values of $\chi$ and $\eta_Q$ depend not only on the hydrogen bond strength, but also on the electronegativity of the atoms involved. As a result of this dual dependence, conclusions regarding the relative strengths of different hydrogen bonds are only appropriate if the hydrogen bonds have similar donors (e.g. comparing O–H donors).

It was also shown that the chemical shift parameters are good indicators of hydrogen bond strength. Chemical shifts were shown to increase upon hydrogen bond formation, and in all cases, shorter, more symmetrical hydrogen bonds had larger $\delta$ values. In the investigation of the complex of TPSiA-TPPO, an increase in chemical shift anisotropy provided an additional piece of evidence indicating the formation of a hydrogen bond. Values of $\Delta\delta$ were not reported for the other compounds studied due to large errors associated with the experimental values. High fields would be required to overcome this problem.

# CHAPTER V

## *FUTURE WORK*

The purpose of this work was to demonstrate the feasibility of using $^2$H NMR to study hydrogen bonding. The compounds that were investigated were chosen for one of two reasons: (a) they possessed hydrogen bonds which were rare and thus never investigated using NMR (e.g. C–H···O and S–H···S); (b) they possessed two distinct hydrogen bonds. There are *thousands* of other hydrogen-bonded systems that could be investigated using $^2$H NMR, and for this reason such prospects will not be discussed. Instead, the focus here will be on four natural extensions of this work.

(1)    <u>Investigation of deuteron migration in pyridine-3,5-dicarboxylic acid</u>

The deuteron migration in pyridine-3,5-dicarboxylic acid could be investigated by experimentally determining the values of the quadrupolar parameters ($\chi$ and $\eta_Q$) at various temperatures (e.g. 296, 200, 150 K). In order to perform such a study, one would require: (a) a probe that could be cooled below 150 K while using MAS; (b) a large amount of available spectrometer time (due to the long relaxation delays required at low temperatures); (c) a method of re-adjusting the magic-angle at low temperatures. Studying the deuteron migration in pyridine-3,5-dicarboxylic acid would provide a more complete investigation of the hydrogen-bonded system. Furthermore, such a study would provide a general indication of the sensitivity of the quadrupolar parameters to changes in hydrogen bond geometry.

(2)    <u>Investigation of the effects of deuteration</u>

Pyridine-3,5-dicarboxylic acid is the most suitable compound for such an investigation as neutron diffraction studies have already been performed on the protonated and deuterated structures. Provided the H atoms involved in the hydrogen bonds could be resolved in the $^1$H spectrum, chemical shifts of the protonated and

146

deuterated analogs could be obtained. Structural changes arising from deuteration would be manifested as a difference in the two values of $\delta$ ($\delta_H$ and $\delta_D$).

The effects of deuteration on other compounds could also be investigated, but first neutron diffraction studies would need to be performed on the deuterated and protonated analogs.

(3)    Investigation of thiobenzamide

Thiobenzamide is of interest because it is the sulfur analog of benzamide, one of the compounds investigated in this work. The crystal structure of thiobenzamide has not been published, and thus calculations are not possible. However, a spectrum of deuterated thiobenzamide could be obtained and analyzed. The spectrum and subsequent analysis would indicate: (a) the number of distinct hydrogen bonding situations; and (b) the relative strengths of the hydrogen bonds (if more than one hydrogen bond). While it would not be possible to assign a specific type of hydrogen bond to a specific spinning sideband manifold, the type of hydrogen bond(s) could be inferred using the quadrupolar and chemical shift parameters from the experiment.

If crystals of thiobenzamide were grown, a neutron or X-ray diffraction analysis could be performed. With a crystal structure, calculations could be performed. This would then mean that the experimental results could be fully interpreted, and compared with the results for benzamide.

(4)    Investigation of systems containing more than two hydrogen bonds

In this work, only structures containing one or two distinct hydrogen bonds were investigated. A natural extension would be to apply this type of study to a system with *more* than two hydrogen bonds. Resolution in such a study would be extremely difficult,

147

as each site would have to have a $\delta$ value at least 2 ppm larger or smaller than the next closest value. Analysis would also be much more difficult, as additional sites have been shown to increase the analysis time exponentially.

# CHAPTER VI

# *REFERENCES*

[1]     Desiraju, G.R.; Steiner, T. *The Weak Hydrogen Bond. In Structural Chemistry and Biology. IUCr Monographs on Crystallography, Vol. 9.* Oxford University Press, London, **1999**.

[2]     Pauling, L. *J. Am. Chem. Soc.* **1935**, 57, 2680.

[3]     Corey, R.B. *J. Am. Chem. Soc.* **1938**, 60, 1598.

[4]     Albrecht, G.; Corey, R.B. *J. Am. Chem. Soc.* **1939**, 61, 1087.

[5]     Senti, F.; Harker, D. *J. Am. Chem. Soc.* **1940**, 62, 2008.

[6]     Pauling, L. *The Nature of the Chemical Bond.* Cornell University Press, Ithaca, New York, **1939**.

[7]     Pimentel, G.C.; McClellan, A.L. *The Hydrogen Bond.* W.H. Freeman, San Francisco, **1960**.

[8]     Jeffrey, G.A.; Saenger, W. *Hydrogen bonding in biological structures.* Springer-Verlag, Berlin, **1991**.

[9]     Steiner, T. and Saenger, W. *J. Am. Chem. Soc.* **1993**, 115, 4540.

[10]    Hamilton, W.C.; Ibers, J.A. *Hydrogen Bonding in Solids.* W.A. Benjamin, New York, **1968**.

[11]    Hibbert, F.; Emsley, J. *Adv. Phys. Org. Chem.* **1990**, 26, 255.

[12]    Gilli, P.; Ferretti, V.; Bertolasi, V.; Gilli, G. *J. Am. Chem. Soc.* **1994**, 116, 909.

[13]    Glasstone, S. *Trans. Faraday Soc.* **1937**, 33, 200.

[14]    Gordy, W. *J. Chem. Phys.* **1939**, 7, 163.

[15]    Sutor, D.J. *Nature* **1962**, 68, 195.

[16]    Sutor, D.J. *J. Chem. Soc.* **1963**, 1105.

[17]    Taylor, R.; Kennard, O. *J. Am. Chem. Soc.* **1982**, 104, 5063.

[18]    Desiraju, G.R. *Acc. Chem. Res.* **1991**, 24, 290.

[19]    Desiraju, G.R. *Acc. Chem. Res.* **1996**, 29, 441.

[20]    Steiner, T. *Crystallogr. Rev.* **1996**, 6, 1.

[21] Allen, F.; Lommerse, J.P.M.; Hoy, J.; Howard, A.K.; Desiraju, D.R. *Acta Crystallogr.*, Sect. B. **1996**, *52*, 734.

[22] Steiner, T. *Chem. Commun.* **1997**, 727.

[23] Desiraju, G.R. *J. Chem. Soc., Chem. Commun.* **1989**, 179.

[24] Desiraju, G.R. *J. Chem. Soc., Chem. Commun.* **1990**, 454.

[25] Pedireddi, V.R.; Desiraju, G.R. *J. Chem. Soc., Chem. Commun.* **1992**, 988.

[26] Steiner, T. *Chem. Commun.* **1994**, 2341.

[27] Kroon, J.; Kanters, J.A. *Nature* **1974**, *248*, 667.

[28] Steiner, T.; Saenger, W. *J. Am. Chem. Soc.* **1992**, 114, 10146.

[29] Novoa, J.J.; Tarron, B.; Whangbo, M.H.; Williams, J.M. *J. Chem. Phys.* **1991**, *95*, 5179.

[30] Taylor, R.; Kennard, O.; Versichel, W. *J. Am. Chem. Soc.* **1983**, *105*, 5761.

[31] Murray-Rust, P.; Glusker, J.P. *J. Am. Chem. Soc.* **1984**, *106*, 1018.

[32] Steiner, T.; Kanters, J.A.; Kroon, J. *Chem. Commun.* **1996**, 1277.

[33] Steiner, T. *J. Phys. Chem.* **1998**, *102*, 7041.

[34] Rundle, R.E.; Parasol, M. *J. Chem. Phys.* **1952**, *20*, 1487.

[35] Lord, R.C.; Merrifield, R.E. *J. Chem. Phys.* **1953**, *21*, 166.

[36] Nakamoto, K.; Margolis, M.; Rundle, R.E. *J. Am. Chem. Soc.* **1955**, *77*, 6480.

[37] Ratajczak, H.; Orville-Thomas, W.J. *Molecular Interactions*. Wiley and Sons, New York, 1980.

[38] Novak, A. *Struct. Bonding* **1974**, *18*, 177.

[39] Bertolasi, V.; Gilli, P.; Ferretti, V.; Gilli, G. *Chem. Eur. J.* **1996**, *2*, 925.

[40] Pimental, G.C.; Sederholm, C.H. *J. Chem. Phys.* **1956**, *24*, 639.

[41] Bellamy, L.J.; Owens, A.J. *Spectrochim Acta*, **1969**, *25A*, 329.

[42] Badger, R.M.; Bauer, S.H. *J. Chem. Phys.* **1937**, *5*, 839.

[43]    Badger, R.M. *J. Chem. Phys.* **1940**, *8*, 288.

[44]    Bellamy, L.J.; Pace, R.J. *Spectrochim Acta*, **1969**, *25A*, 319.

[45]    Purcell, K.F.; Drago, R.S. *J. Am. Chem. Soc.* **1967**, *89*, 2874.

[46]    Drago, R.S.; Vogel, G.C.; Needham, T.E. *J. Am. Chem. Soc.* **1971**, *93*, 6014.

[47]    Giermanska, J.; Szostak, M.M. *J. Raman Spectros.* **1991**, *22*, 107.

[48]    Baran, W.J.; Ratajezak, H.; Lutz, E.T.G.; Verhaegh, N.; Luinge, H.J.; van der Maas, J.H. *J. Molec. Struct.* **1994**, *326*, 109.

[49]    Lutz, E.T.G.; Veldhuizen, J.; Kanters, J.A.; van der Maas, J.H.; Baran, J.; Ratajczan, H. *J. Molec. Struct.* **1992**, *270*, 381.

[50]    Lutz, E.T.G.; Jacob, J.; van der Maas, J. *Vib. Spectrosc.* **1996**, *12*, 197.

[51]    Ditchfield, R. *J. Chem. Phys.* **1976**, *65*, 3123.

[52]    Rohlfing, C.M.; Allen, L.C.; Ditchfield, R. *J. Chem. Phys.* **1983**, *79*, 4958.

[53]    Foster, R.; Fyfe, C.A. *Progress in Nuclear Magnetic Resonance Spectroscopy. Vol. 4.* Pergamon Press, London, **1969**.

[54]    Dachs, H. *Neutron Diffraction.* Springer-Verlag, Berlin, **1978**.

[55]    Coppens, P. *X-ray charge densities and chemical bonding.* Oxford University Press, New York, **1997**.

[56]    Glusker, J.P.; Lewis, M.; Rossi, M. *Crystal structure analysis for chemists and biologists.* VCH, New York, **1994**.

[57]    Cotton, F.A.; Luck, R.L. *Inorg. Chem.* **1989**, *28*, 3210.

[58]    Aakeröy, C.B.; Seddon, K.R. *Chem. Soc. Rev.* **1993**, *22*, 397.

[59]    Jeffrey, G.A. *An introduction to hydrogen bonding.* Oxford University Press, New York, **1997**.

[60]    Olovsson, I.; Jönsson, P.G. *The Hydrogen Bond.* North Holland Publishing Company, Amsterdam, **1976**.

[61]    Gould, I.R.; Kollman, P.A. *J. Am. Chem. Soc.* **1994**, *116*, 2493.

[62] Boggs, J.E. *Accurate Molecular Structures*. Oxford University Press, United Kingdom, **1992**.

[63] Scheiner, S. *Ann. Rev. Phys. Chem.* **1994**, *45*, 23.

[64] Harris, R.K. *Nuclear Magnetic Resonance Spectroscopy: A Physicochemical View*. Longman Scientific & Technical, United Kingdom, **1986**.

[65] Akitt, J.W. *NMR and Chemistry*. Chapman and Hall, New York, **1983**.

[66] Bloch, F. *Phys. Rev.* **1946**, *70*, 460.

[67] Lowe, I. *Phys. Rev. Lett.* **1959**, *2*, 285.

[68] Andrew, E.R.; Bradbury, A.; Eades, R.G. *Nature* **1958**, *182*, 659.

[69] Duer, M.J. *Solid-state NMR spectroscopy*. Blackwell Science Limited, U.S.A., **2002**.

[70] Pake, G.E. *J. Chem. Phys.* **1948**, *16*, 327.

[71] Chiba, T. *J. Chem. Phys.* **1964**, *41*, 1352.

[72] Blinc, R.; Hadzi, D. *Nature* **1966**, *212*, 1307.

[73] Soda, G.; Chiba, T. *J. Chem. Phys.* **1969**, *50*, 439.

[74] Sternberg, U. *Mol. Phys.* **1988**, *63*, 249.

[75] Sternberg, U.; Brunner, E. J. Magn. Reson. **1994**, *22*, 295.

[76] Kalsbeek, N.; Schaunburg, K.; Larsen, S. *J. Mol. Struct.* **1993**, 155.

[77] Zhao, X.; Dvorak, C.; Silvernail, C.; Belot, J.; Harbison, G.S. *Solid State Nucl. Magn. Reson.* **2002**, *22*, 363.

[78] Ono, S.; Taguma, T.; Kuroki, S.; Ando, I.; Kimura, H.; Yamauchi, K. *J. Mol. Struct.* **2002**, *602*, 49.

[79] Camus, S.; Harris, K.D.M.; Johnston, R. *Chem. Phys. Lett.* **1997**, *276*, 186.

[80] Turner, G.W.; Johnston, R.L.; Harris, K.D.M. *Chem. Phys.* **2000**, *256*, 159.

[81] Bailey, W.C. *J. Mol. Spectrosc.* **1998**, 318.

[82] Lee, C.; Yang, W.; Parr, R.G. *Phys. Rev. B.* **1988**, *37*, 785.

[83]   Gerber, S.; Huber, H. *J. Mol. Spectrosc.* **1989**, *134*, 168.

[84]   Michal, C.A.; Wehman, J.C; Jelinski, L.W. *J. Magn. Reson.* **1996**, *111*, 31.

[85]   Berglund, G.; Vaughan, R.W. *J. Chem. Phys.* **1980**, *73*, 2037.

[86]   Jeffrey, G.A.; Yeon, Y. *Acta Crystallogr.* **1986**, *B42*, 410.

[87]   Harris, R.K.; Jackson, P.; Merwin, L.H.; Say, B.J.; Hagele, G. *J. Chem. Soc. Farad. Trans.* **1988**, *84*, 3649.

[88]   Yamauchi, K.; Kuroki, S.; Fuki, K.; Ando, I. *Chem. Phys. Lett.* **2000**, *324*, 435.

[89]   Brunner, E.; Sternberg, U. *Prog. Nucl. Magn. Reson.* **1998**, *32*, 21.

[90]   Wu, G.; Freure, C.J.; Verdurand, E. *J. Am. Chem. Soc.* **1998**, *120*, 187.

[91]   Hauch, A.; Bildsoe, H.; Jakobsen, H.J.; Skibsted, J. *J. Magn. Reson.* **2003**, *165*, 282.

[92]   Brouwer, D.; Ripmeester, J.A. *J. Magn. Reson.* **2007**, *185*, 173.

[93]   Gallagher, K.J. *Hydrogen bonding.* Pergamon Press, New York, **1959**.

[94]   Robertson, J.M.; Ubbelohde, A.R. *Proc. R. Soc. London Ser. A.* **1939**, *170*, 222.

[95]   Sakhawat Hussain, M.; Schlemper, E.O. *Acta Crystallogr.* **1980**, *B36*, 1104.

[96]   Nelmes, R.J.; Meyer, G.M.; Tibbalis, J.E. *J. Phys.* **1982**, *C15*, 59.

[97]   *Gaussian 03* (Revision B.01), M. J. Frisch, G. W. Trucks, H. B. Schlegel, G.E. Scuseria, M. A. Robb, J. R. Cheeseman, J. A. Montgomery, Jr., T. Vreven, K. N. Kudin, J. C. Burant, J. M. Millam, S. S. Iyengar, J. Tomasi, V. Barone, B. Mennucci, M. Cossi, G. Scalmani, N. Rega, G. A. Petersson, H. Nakatsuji, M. Hada, M. Ehara, K. Toyota, R. Fukuda, J. Hasegawa, M. Ishida, T. Nakajima, Y. Honda, O. Kitao, H. Nakai, M. Klene, X. Li, J. E. Knox, H. P. Hratchian, J. B. Cross, C. Adamo, J. Jaramillo, R. Gomperts, R. E. Stratmann, O. Yazyev, A. J. Austin, R. Cammi, C. Pomelli, J. W. Ochterski, P. Y. Ayala, K. Morokuma, G. A. Voth, P. Salvador, J. J. Dannenberg, V. G. Zakrzewski, S. Dapprich, A. D. Daniels, M. C. Strain, O. Farkas, D. K. Malick, A. D. Rabuck, K. Raghavachari, J. B. Foresman, J. V. Ortiz, Q. Cui, A. G. Baboul, S. Clifford, J. Cioslowski, B. B. Stefanov, G. Liu, A. Liashenko, P. Piskorz, I. Komaromi, R. L. Martin, D. J. Fox, T. Keith, M. A. Al-Laham, C. Y. Peng, A. Nanayakkara, M. Challacombe, P. M. W. Gill, B. Johnson, W. Chen, M. W. Wong, C. Gonzalez, and J. A. Pople, Gaussian, Inc., Pittsburgh PA, 2003.

[98] Bak, M.; Rasmussen, T.; Nielsen, N.C. *J. Magn. Reson.* **2000**, *147*, 296.

[99] Peterson, K.A.; Dunning, T.H. *J. Chem. Phys.* **2002**, *117*, 10548.

[100] Woon, D.E.; Dunning, T.H. *J. Chem. Phys.* **1995**, *103*, 4572.

[101] Becke, A.D. *J. Chem. Phys.* **1992**, *96*, 2155.

[102] Becke, A.D. *J. Chem. Phys.* **1992**, *97*, 9173.

[103] Becke, A.D. *J. Chem. Phys.* **1993**, *98*, 5648.

[104] Lee, C.; Yang, W.; Parr, R.G. *Phys. Rev.* **1988**, *B37*, 785.

[105] London, F. *J. Phys. Radium* **1937**, *8*, 397.

[106] Muenter, J.S.; Klemperer, W. *J. Chem. Phys.* **1970**, *52*, 6033.

[107] Kaiser, E.W. *J. Chem. Phys.* **1970**, *53*, 1686.

[108] Van Eijck, B.P. *J. Mol. Spectrosc.* **1990**, *143*, 231.

[109] Wofsy, S.C.; Muenter, J.S.; Klemperer, W. *J. Chem. Phys.* **1970**, *53*, 1686.

[110] Viswanathan, R.; Dyke, T.R. *J. Mol. Spectrosc.* **1984**, *103*, 231.

[111] Cazzoli, G.; Dore, L. *J. Mol. Spectrosc.* **1990**, *143*, 231.

[112] Tucker, K.D.; Tomasevich, G.R. *J. Mol. Spectrosc.* **1973**, *48*, 475.

[113] Kukolich, S.G.; Nelson, A.C.; Ruben, D.J. *J. Mol. Spectrosc.* **1971**, *40*, 33.

[114] Ruben, D.J.; Kukolich, S.G. *J. Chem. Phys.* **1974**, *60*, 100.

[115] Quinn, W.E.; Baker, J.M.; LaTourrette, T.; Ramsey, N.F. *Phys. Rev.* **1958**, *112*, 1929.

[116] Code, R.F.; Ramsey, N.F. *Phys. Rev.* **1971**, *A4*, 1945.

[117] Murray, A.M.; Kukolich, S.G. *J. Chem. Phys.* **1982**, *77*, 4312.

[118] Murray, A.M.; Kukolich, S.G. *J. Chem. Phys.* **1983**, *78*, 3557.

[119] De Lucia, F.C.; Helminger, P.; Gordy, W. *Phys. Rev.* **1971**, *A3*, 1849.

[120] Gray, D.L.; Robiette, A.G. *Mol. Phys.* **1979**, *37*, 1901.

[121] Edwards, T.H.; Moncur, N.K.; Snyder, L.E. *J. Chem. Phys.* **1967**, *46*, 2139.

[122] Carter, S.; Mills, I.M.; Handy, N.C. *J. Chem. Phys.* **1992**, *97*, 1606.

[123] Carter, S.; Handy, N.C. *J. Mol. Spectrosc.* **1996**, *179*, 65.

[124] Kawashima, Y.; Cox, A.P. *J. Mol. Spectrosc.* **1978**, *72*, 423.

[125] Davis, R.W.; Robiette, A.G.; Gerry, M.C.L.; Bjarnov, E.; Winnewisser,G. *J. Mol. Spectrosc.* **1980**, *81*, 93.

[126] Stoicheff, B.P. *Can. J. Phys.* **1957**, *35*, 730.

[127] Venkatachar, H.C.; Taylor, R.C.; Kuczkowski, R.L. *J. Mol. Struct.* **1977**, *38*, 17.

[128] Le Guennec, M.; Wlodarcxak, G.; Burie, J.; Demaison, J. *J. Mol. Spectrosc.* **1992**, *154*, 305.

[129] Chestnut, D.B. In: Lipkowitz, L.B.; Boyd, D.B. (eds) *Reviews in computational chemistry.* VCH, New York, **1996**.

[130] Forsyth, D.A.; Sebag, A.B. *J. Am. Chem. Soc.* **1997**, *119*, 9483.

[131] Schäfer, A.; Horn, H.; Ahlrichs, R. *J. Chem. Phys.* **1992**, *97*, 2571.

[132] Steiner, T.; van der Maas, J. Lutz, B. *J. Chem. Soc. Perkin Trans. 2* **1997**, 1287.

[133] Steiner, T. *Z. Kristallogr.* **1995**, *210*, 475.

[134] Gdaniec, M.; Olszewska, T.; Polonski, T. *Acta Crystallogr. C* **2004**, *60*, o41.

[135] Gao, Q.; Jeffrey, G.A.; Ruble, J.R.; McMulan, R.K. *Acta Crystallogr. B* **1991**, *47*, 742.

[136] Macho, V.; Brombacher, L.; Spiess, H.W. *Appl. Magn. Reson.* **2001**, *20*, 405.

[137] Miwa, Y.; Mizuno, T.; Tsuchida, K.; Taga, T. Iwata, Y. *Acta Crystallogr. B* **1999**, *B55*, 78.

[138] Chao, M.; Shempp, E.; Rosenstein, R.D. Acta *Crystallogr. B - Stru.* **1975**, *31*, 2922.

[139] Bacon, G.E.; Jude, R.J. *Z. Kristallogr.* **1973**, *138*, 19.

[140]  Wunderlich, H.; Mootz, D. *Acta Crystallogr. B – Stru* **1971**, *27*, 1684.

[141]  Cowan, J.A.; Howard, J.A.K.; McIntyre, G.J.; Lo, S.M.F.; Williams, I.D. *Acta. Crystallogr. B* **2005**, *61*, 724.

[142]  David, J.G.; Hallam, H.E. *Spectrochim. Acta* **1965**, *21*, 841.

[143]  Steiner, T. *Acta Crystallogr. C* **2000**, *56*, 876.

[144]  Allen, F.H.; Bird, C.M.; Rowland, R.S.; Raithby, P.R. *Acta Crystallogr. B* **1997**, *53*, 696.

[145]  Gorbitz, C.H.; Dalhus, B. *Acta Crystallogr. C* **1996**, *52*, 1756.

[146]  Mikenda, W.; Steinwender, E.; Mereiter, K. *Monatsh. Chem.* **1995**, *126*, 495.

[147]  Heinicke, J.; Kadyrov, R.; Kindermann, M.K.; Koesling, M.; Jones, P.G. *Chem. Ber.* **1996**, *129*, 1547.
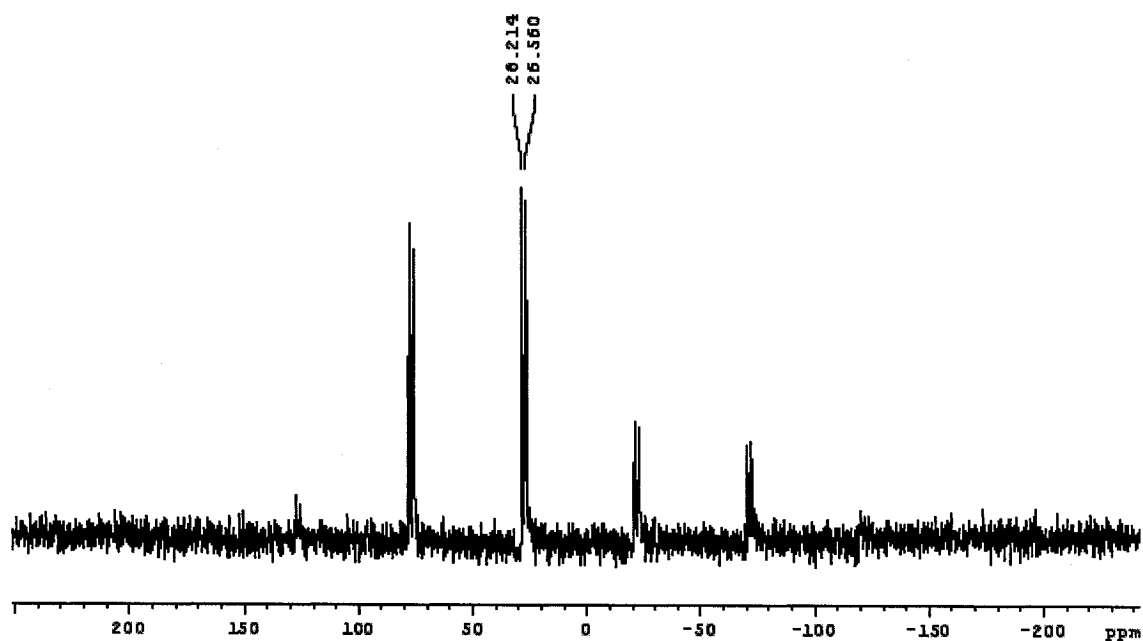
# APPENDICES
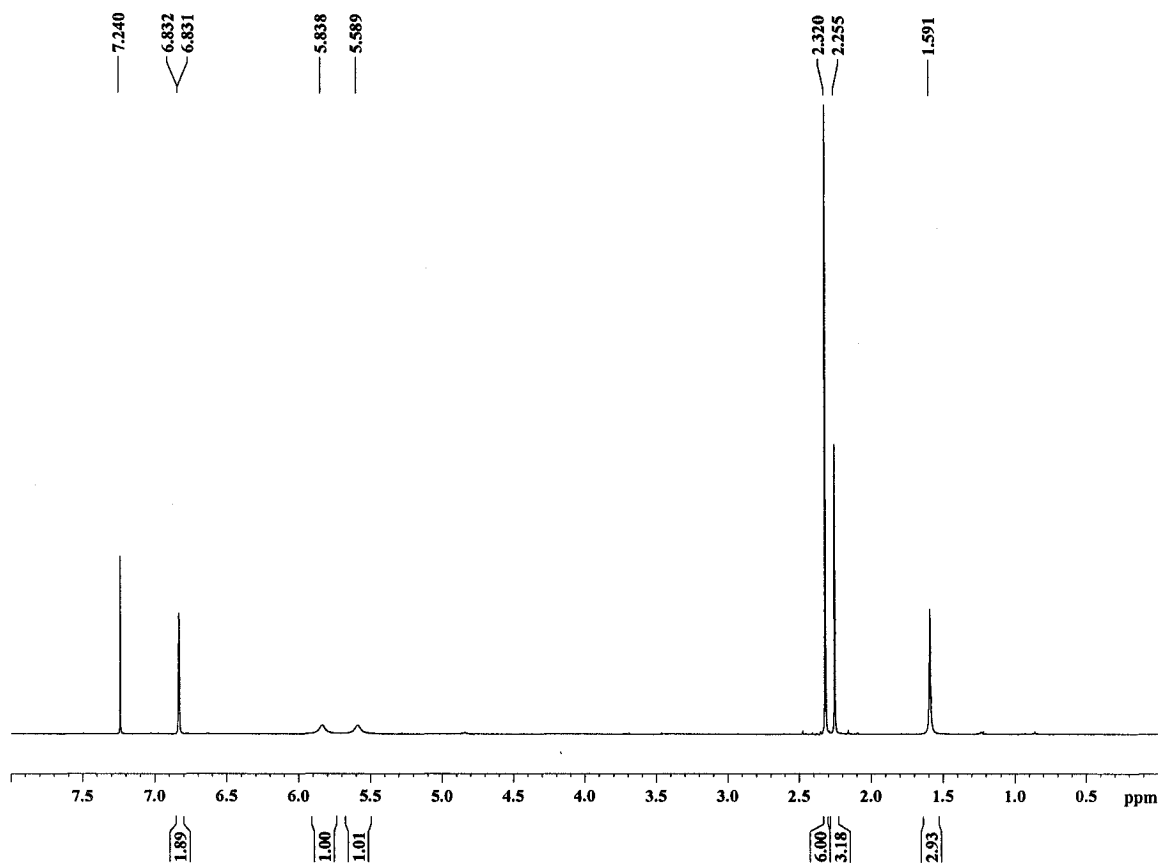
$^1$H spectrum of synthesized 2,4,6-trimethylbenzamide in CDCl$_3$. The peak at 1.591 ppm is a water peak that was eliminated after the deuteration process.

159
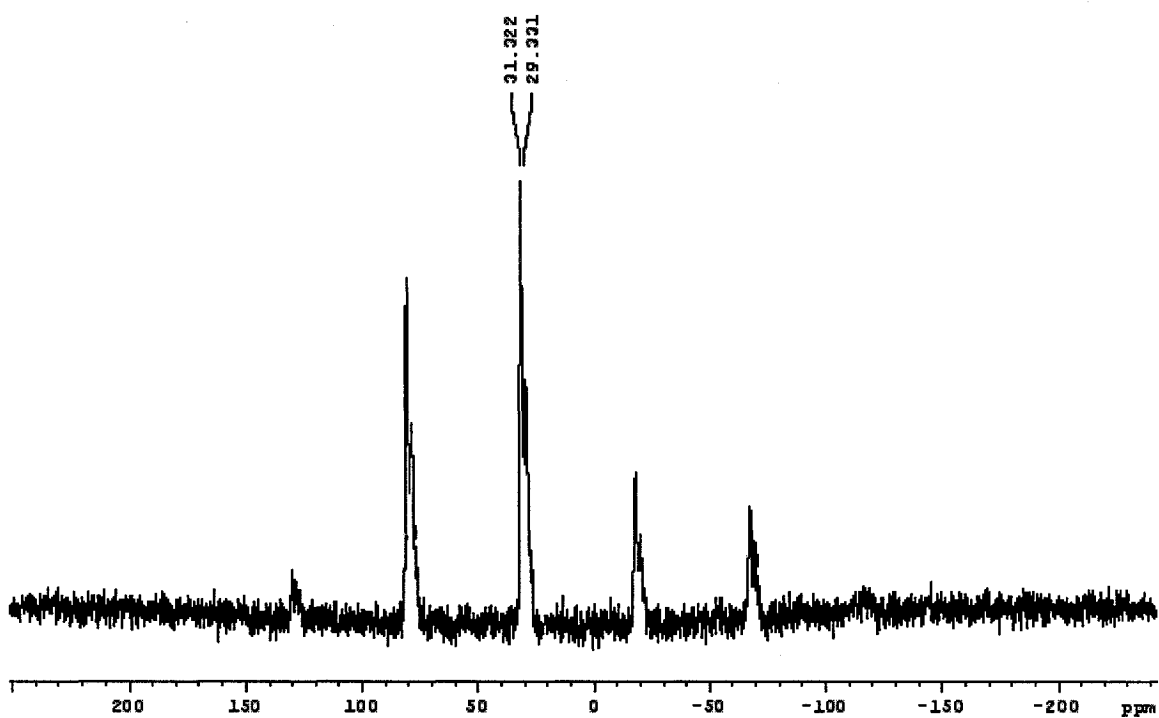
$^{31}$P spectrum of (a) TPPO (b) the complex of TPSiA-TPPO. The increase in chemical shift of 2.9 ppm in going from TPPO to the complex indicates the formation of a hydrogen bond.

```
spinsys (
      nuclei 2H 2H
      channels 2H
      shift 1 6p 0 0 0 0
      shift 2 10p 0 0 0 0
      quadrupole 1 1 2.2e5 0.1 0 0 0
      quadrupole 2 1 1.8e5 0.2 0 0 0
)
```

**Defining the internal spin Hamiltonians and the spin system.**

```
par (
      start_operator        I1x
      detect_operator       I1p
      spin_rate             10000
      gamma_angles          20
      sw                    400000
      crystal_file          rep168
      np                    2048
      proton_frequency      495e6
      rotor_angle           54.7
      verbose               1101
)
```

**Experimental parameters include intitial and detect operator, spectral width, rotor angle, rf field strengths, and sampling time.**

```
proc pulseq ( ) (
      global par

      maxdt 1

      set tdwell [espr 1.0e6/$par(sw)]
      acq
      for (set i 1) ($i < $par(np)) (incr i) (
            delay $tdwell
            acq
      )
)
```

**The pulse sequence, allowing the flexibility to simulate any solid-state NMR experiment.**

```
proc main ( )
      global par

      set f [fsimpson]
      fsave $f  $par(name).fid
      fzerofill $f 8192
      faddlb $f 100 0
      fft $f
      fsave $f $par(name).spe
)
```

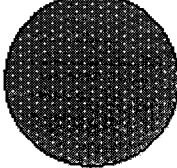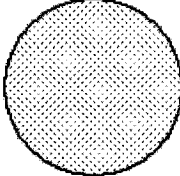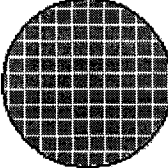**Processing protocols include zero filling of data, Fourier transform of the FID, apodisation and base line correction.**

| Element | Symbol |
|---|---|
| Hydrogen, H |  |
| Deuterium, D |  |
| Carbon, C |  |
| Nitrogen, N |  |
| Oxygen, O |  |
| Silicon, Si |  |
| Phosphorus, P |  |
| Sulfur, S |  |

# APPENDIX D
## Hydrogen Bond Geometries after Hydrogen Position Optimization

### Hydrogen bonded geometry of 2,4,6-trimethylbenzamide

| X–H···A | X–H (Å) | H···A (Å) | X···A (Å) | X–H···A (°) |
|---------|---------|-----------|-----------|-------------|
| N–H···π | 1.02    | 2.38      | 3.40      | 173         |
| N–H···O | 1.02    | 1.85      | 2.87      | 175         |

### Hydrogen bonded geometry of 2-aminopyridine

| X–H···A | X–H (Å) | H···A (Å) | X···A (Å) | X–H···A (°) |
|---------|---------|-----------|-----------|-------------|
| N–H···N | 1.02    | 2.05      | 3.07      | 176         |

### Hydrogen bonded geometry of catechol

| X–H···A | X–H (Å) | H···A (Å) | X···A (Å) | X–H···A (°) |
|---------|---------|-----------|-----------|-------------|
| O–H···O | 0.99    | 1.93      | 2.82      | 148         |
| O–H···O | 0.99    | 1.81      | 2.80      | 170         |

### Hydrogen bonded geometry of thiosalicylic acid

| X–H···A | X–H (Å) | H···A (Å) | X···A (Å) | X–H···A (°) |
|---------|---------|-----------|-----------|-------------|
| S–H···S | 1.39    | 2.65      | 3.99      | 162         |
| O–H···O | 1.01    | 1.65      | 2.66      | 176         |

### Hydrogen bonded geometry of 2-hydroxythiobenzoic acid

| X–H···A | X–H (Å) | H···A (Å) | X···A (Å) | X–H···A (°) |
|---------|---------|-----------|-----------|-------------|
| S–H···O | 1.35    | 2.06      | 3.41      | 175         |
| O–H···O | 0.98    | 1.73      | 2.59      | 144         |

### Hydrogen bonded geometry of 2-[t-Butyl(phenyl)phosphanyl]-4-methylphenol

| X–H···A | X–H (Å) | H···A (Å) | X···A (Å) | X–H···A (°) |
|---------|---------|-----------|-----------|-------------|
| O–H···P | 0.98    | 2.26      | 3.18      | 155         |